Semi-Conductor Core Optical Fibers and Fabrication Dependence of the Grain Structure

Brian L. Scott

Dissertation submitted to the faculty of the Virginia Polytechnic Institute and State University in partial fulfillment of the requirements for the degree of
Doctor of Philosophy
In
Materials Science and Engineering

Gary Pickrell-Chair
Levon Asryan
Carlos Suchicital
Anbo Wang

September 09, 2011
Blacksburg, VA

Keywords: Silicon, Gallium Antimonide, Optical Fiber, EBSD, Silicon Optical Fiber Grain length

Semi-Conductor Core Optical Fibers and Fabrication Dependence of the Grain Structure

Brian L. Scott

ABSTRACT

The production and fabrication of semi-conductor core optical fibers was shown to be feasible and controllable. This was accomplished through the step sequence of fabrication and characterization of 4 fiber types, an experiment on controlling the grain length in the core and a simple model of the heat transfer during fabrication. Fibers were first made with a silicon core, followed by a phosphorous doped n-type silicon core, then a boron doped p-type silicon core, and a tellurium doped n-type gallium antimonide core. Characterization of the fibers was accomplished with energy dispersive spectroscopy (EDS) for compositional analysis, electron backscatter diffraction (EBSD) for crystal orientation and grain size, optical and electron microscopy for physical fiber quality and optical transmission for core optical quality. A model was developed to relate the heat transfer with the grain structure of the fiber core. All of the fibers fabricated had a polycrystalline core with either no detectable oxygen in the case of the silicon fibers or low amounts of oxygen diffusion into the core as in the case of the GaSb fibers. Fiber lengths ranged from 7 cm for the initial silicon fibers to 60 cm and outside diameters down to 100 μm for n and p type silicon fibers. Core diameters for all fiber types ranged from 10 – 200 μm depending on the fabrication parameters. Lengths of major grains in the core are dependent on the core diameter and the pulling speed. The grain lengths of the major grains in the core generally increase in length with an increase in core diameter. Grain lengths in all fibers are thought to be suitable for use in fabrication of electronic

structures in the core region with even the smallest average grain length of around 300 μm. This grain structure satisfies the grain boundary requirements for fabrication of boundary free p-n junctions and other more complicated electronic structures. Small core diameter fibers had better physical quality with fewer cracks and longer continuous length than the larger core fibers.

Acknowledgements

During my time here in the pursuit of this work I've had the great fortune to associate with many wonderful people that have helped me along the way. Without their help this work would have taken much longer. I would like to thank Rick Smith as he has been my mentor in the practical aspects of making or fixing anything, Denise Mainville who has helped me through many other non-academic aspects of the PhD program, Kim Grandstaff and her invaluable assistance in keeping the appropriate stuff together and my advisor Gary Pickrell who seems to have an infinite amount of patience.

Table of Contents

Contents

Table of Figures

.

List of Tables

1. Introduction

Silicon photonics is a field that has seen many developments since its inception. Currently, most silicon photonic structures are fabricated using traditional methods of deposition onto a substrate.[1] The optical signal, from an optical fiber, is then brought into the silicon device to be processed and reintroduced into an outgoing fiber.[2] Silicon photonic structures have many uses including optical signal sources, signal detectors, raman amplifiers, and many other opto-electronic devices.[3] Recently, silicon has been incorporated into optical fibers, where the silicon makes up the core region of the fiber. Currently silicon optical fibers have been made through two methods, one of which involves the heating of silicon to past its melting point while it is surrounded by a silica glass tube.[4-6] The current state of silicon optical fibers is one of short lengths, polycrystalline cores, and cores with multiple fractures that segment the core region. In order for these fibers to become more useful they must be able to have predictable crystalline properties and continuous cores free from physical defects. Fabrication of a successful silicon fiber will enable the development of in-fiber devices, which in turn will improve the efficiency of optical processing and open up the door to more complicated opto-electronic structures for use in optical fibers.

The development of silicon optical fibers presents a method in which opto-electronics can be combined with optical fiber communications in one package. Fibers of this type will allow for the fabrication of the necessary electronic circuits and devices in the core of the fiber. Currently, the use of opto-electronics usually requires the splicing of the device into the optical transmission path and the signal typically leaves the fiber and is processed

in some way before returning to the transmission pathway.[3] This shifting around of the optical signal causes a reduction in the efficiency and requires an increase in power to compensate for this efficiency decrease. Through incorporation of these devices within the fiber itself, the redirecting of the optical signal can be eliminated. In addition to the in fiber opto-electronics, these fibers open the way for long-wavelength transmission without the need for a complicated preform fabrication process that is necessary to cope with the toxicity of the materials in the fabrication of the chalconide glass fibers. A high temperature capability will also be accessible as the operating range of silicon exceeds the melting points of the chalconide glasses.[7]

There has been a recent development in the fabrication of optical fibers that incorporate semiconductors as the core material.[4-6, 8, 9] The development of these fibers has been limited to silicon and germanium as the core material. While silicon and germanium have the advantage of being well studied platforms for electronic devices, long wavelength transmission and integration into existing silicon photonic structures, they are not suitable for efficient light generation. This is primarily due to both materials having an indirect band gap structure. While low efficiency LED's have been made with these materials it is more common for LEDs and diode lasers to be made from III-V semiconductor structures. More recently, the fabrication of a III-V semiconducting core has been accomplished using InSb.[10] Incorporation of these semiconducting materials into the core region of optical fibers will allow for the fabrication of the structures and devices for these types of opto-electronics within the fiber. It is envisioned that a series of post fiber fabrication processes will build the structures necessary for these devices. Selected

regions of the fiber could be manipulated and the devices built onto an exposed end face of the fiber along with electrical contacts and then reincorporated back into the fiber network. Many challenges exist in the creating these devices in the fiber and finding a suitable semiconductor core material. However, being able to fabricate the fibers is the first step.

Results of the fabrication of a glass clad gallium antimonide optical fiber is also presented in addition to the work on fabrication of silicon optical fibers. The focus on the fabrication is the establishment of an additional suitable platform for the future fabrication of opto-electronic devices within the core region for use in the mid infrared region. The transmission window for GaSb is from approximately 2-25 μm.[7] At a stoichiometric mixture of 50% gallium and 50% antimony, the system forms a congruently melting compound upon freezing, making the composition a good choice for this type of III-V core material using a fiber draw casting method. [11] Gallium antimonide is also a good candidate for this type of semiconducting optical core material due to its melting point of 712 °C, low vapor pressure, previous device fabrication and the proven integration of other III-V material components.[12] GaSb has been used to fabricate diode lasers and LEDs with emission in the mid infrared wavelength range where GaSb has been used as the substrate for the device fabrication.[13-15]

Fabrication of silicon optical fibers uses a heat and draw method from a preform typical of optical fiber production. The preform is heated and once the silicon is melted and the silica glass is at a sufficiently low viscosity, the fiber is pulled from the preform. As a

fiber is pulled from the heated zone the silicon in the core region begins to cool and will eventually solidify. Currently, the influence of the processing and fabrication parameters on the solidification process of the silicon in the core region is not understood sufficiently in order to be able to control the properties of the core. Control of the core will enable that future processing can be done to produce opto-electronic circuits and devices on and in the core region. In order to control the properties of the core, this influence on the solidification of the silicon core needs to be understood and how the fabrication parameters dictate the solidification process also needs to be understood. The initial questions to be answered are: what is the achievable microstructure of the core, what can be controlled by the fabrication parameters and does this give a sufficient grain structure such as grain length to allow for the fabrication of devices within the fiber core.

This research covers the experimental approach to determining the feasibility of fabricating semi-conductor core optical fibers for use within the optical fiber scale range and to determine the process factors used in the fabrication of silicon optical fibers and how they influence the resultant microstructure of the silicon in the fiber. The approach uses the fabrication parameters and the produced microstructure to understand the silicon solidification process as it happens during the fiber drawing process.

2. Background

2.1 Grain boundaries in Silicon

The fibers that have been made thus far, have a polycrystalline core which is expected due to the high rate of cooling that the fibers experience as they are being drawn. If the

grain size in the fiber core is made sufficiently large, the effect of the grain boundaries will be reduced in addition to providing a large enough platform for constructing circuit components in one or more of the single crystal grains. The use of silicon for integrated circuits has been around since the early 50's and is the most widely used material for ICs. Accordingly, a large amount of research has been done on silicon and with the use of polycrystalline silicon in photovoltaic cells that research has extended into the effects of grain boundaries and grain size on the performance and properties of silicon.

Grain boundaries usually have a detrimental effect in silicon in which the grain boundaries act as potential barriers, can show a capacitance in the presence of an alternating voltage, and can act as recombination centers.[16] The potential barrier at the grain boundary arises from the charge trapping by the dangling bonds in the highly disordered grain boundary.[16] As charges build up at the interface between grains, the effect of band bending occurs.[17] This band bending will change the energy gap from that of the bulk in the vicinity of the boundary. The amount of band bending is dependent on the surface density of interface traps, the grain size and the dopant concentration. A maximum in the barrier height (φ_b) is given by Equation 1 and the relation of the barrier height to the grain size and dopant concentration in Equation 2. [17]

$$\varphi_{bmax} = \frac{e^2 l N_t}{8\varepsilon\varepsilon_0} \tag{1}$$

$$\varphi_b = \frac{e^2 l^2 N}{8\varepsilon\varepsilon_0} \tag{2}$$

Where l is the grain size, N_t is the surface density of interface traps, and N is the dopant concentration. The critical doping level (N_{max}) where φ_b reaches the maximum is given in Equation 3.[17]

$$N_{max} = \frac{N_t}{l} \tag{3}$$

At doping levels above N_{max} there will begin to be excess free carriers which will lower the height of the barrier. As the doping level becomes very high the boundary states will become saturated and at this point the barrier height will be quite small.[16] The barrier height will affect the resistivity of the silicon as detailed in Equation 4. [16]

$$I = I_0 exp\left\{-\frac{\varphi_b}{\kappa T}\right\} \tag{4}$$

Where I_o is the un-doped silicon resistivity, κ is the Boltzmann constant and T is the temperature. Significant barrier height can occur depending on the value of N_t, φ_b, and l to such a degree that the resistivity of the silicon can be dramatically increased.

Optical transmission is also affected by the grain structure in silicon. The presence of dangling bonds, the potential barrier, and precipitates at the grain boundaries can cause increased transmission loss. Polycrystalline silicon waveguides with hydrogen passivated grain boundaries show a decrease in the transmission loss.[18] Increase in the grain size also showed a decrease in transmission loss.[18] The grain boundaries and precipitates

act as scattering centers and the dangling bonds at the grain boundaries alter the band gap in the grain boundary vicinity which will change the adsorption behavior.

Diffusion in this region is also much higher than in the bulk due to the highly disordered crystalline state at the grain boundaries. Due to the high degree of disorder and the high diffusion rates present at the grain boundaries they will also act as dopant segregation centers.[16] These centers will grow precipitates of the impurities depending on the impurity concentration.[19, 20] Both the dopant segregation and the growth of the impurity precipitates will influence the barrier height at the grain boundaries and the precipitates can act as scattering centers.[19, 20]

2.2 Solidification

The solidification of the core can be considered to be similar to a method of casting where the core is drawn out into a flexible heated mold. Fabrication parameters relevant to core solidification are the fiber dimensions, the volume of silicon pulled into a fiber, the starting temperature of the preform at pulling, and the speed of the fiber pull. The silica cladding thickness may dictate the rate of cooling of the core as thermal conductivity has units in the form of $\frac{watts}{m \cdot K}$, which shows that the amount of heat loss will go down per unit time as the cladding thickness goes up. The cladding may also act as a participating media in the radiation of heat from the core through the cladding. As the rate of heat loss goes down, the amount of undercooling the silicon has prior to nucleation of crystals will be lower. It would be expected that the fewer grains would be nucleated and larger grains would be formed once the solidification process was

completed. Changing the fiber dimensions should show up as changes in the average grain size in the core. A smaller core and cladding dimensions will show up as smaller average grain sizes than a fiber with larger dimension.

Solidification of silicon from the melt that is created through heating of the preform to temperatures above 1412 °C will follow similar solidification processes to that of cast metals, as the thermodynamic driving forces and atomic process will be the same. In the process of solidification, the molten silicon will go from a molten state to a solid state first by the nucleation of crystal nuclei, which then grow as heat is removed from the fiber. The nuclei will grow until they impinge or contact other crystals growing into the melt. Assuming heterogeneous nucleation, the process of nucleation of crystal nuclei and the growth of grains will be dependent on the surface characteristics of the silica tube and the rate of cooling of the silicon.

Nucleation of crystals from the melt is governed mainly by thermodynamic requirements. As crystals begin to form in the melt pool a new surface is created with an attendant interfacial energy between the liquid and the solid. If the solid is to be stable, the added energy from the interface needs to be balanced by a reduction in energy due to the formation of the solid. Derivation of these requirements is well published. The derivation presented here is from Sinha's metallurgical handbook[21] with the first part being relevant to formation due to homogenous nucleation. Modification of the derivation due to heterogeneous nucleation follows the first part. Formation of a solid within a melt is

determined by the reduction of the free energy. For a pure material, the change in the free energy at the melting temperature is given by Equation 5.

$$\Delta G_v = G_v^s - G_v^l = H_s - H_l - T_m(S_s - S_l) = 0 \quad (5)$$

With Equation 5 rewritten as Equation 6.

$$\Delta G_v = \Delta H_f - T_m \Delta S \quad (6)$$

Because the free energy change is zero in equilibrium Equation 6 becomes

$$\Delta H_f = \frac{\Delta S}{T_m} \quad (7)$$

with G_v^s, G_v^l, H_s, H_L, S_s and S_L being the volume free energy, enthalpy and entropy of the solid and liquid, respectively. ΔH_f is the enthalpy change, which is also the latent heat of fusion (L_v) per unit volume. Combination of the Equations 5 and 7 relates the volume free energy change at temperatures other than the melting point, given in Equation 8.

$$\Delta G_v = \frac{\Delta H_f (T_m - T)}{T_m} = \frac{\Delta H_f (\Delta T)}{T_m} = \frac{L_v (\Delta T)}{T_m} = \Delta S_f \Delta T \quad (8)$$

Equation 8 relates the free energy change due to the undercooling (ΔT). This can be used to understand the minimum embryo radius necessary for the crystal to be stable and not dissolve back into the melt. The total change in free energy has contributions from the change in volume free energy G_v and the free energy associated with the interface

between the solid and the liquid. With a spherical embryo nucleating from the melt and the interfacial energy of γ_{sl} between the embryo and the liquid, the total free energy can be given by Equation 9.

$$\Delta G = \Delta G_v + \Delta G_i = -\frac{4\pi r^3 \Delta H_f \Delta T}{3T_m} + 4\pi r^2 \gamma_{sl} \quad (9)$$

The critical radius is the radius at which the crystal embryo is stable, which occurs when ΔG is at a maximum. This condition is expressed in Equation (10)

$$\left[\frac{\partial \Delta G(r)}{\partial r}\right]_{r=r^*} = 0 \quad (10)$$

When the condition for ΔG is met, then the critical radius (r^*) is given by Equation 11.

$$r^* = \frac{2\gamma_{sl}}{\Delta G_v} = \frac{2\gamma_{sl} T_m}{L_v \Delta T} \quad (11)$$

From Equation 11 it can be seen that as the undercooling (ΔT) becomes larger, the critical radius necessary for solidification to begin becomes smaller. The rate at which nuclei are formed is also dependent on the amount of undercooling of the liquid. For metals this can be expressed as it is in Equation 12.

$$\dot{N} = K_2 exp\left[-\frac{K_3}{T(\Delta T)^2}\right] \quad (12)$$

K_2 and K_3 are constants in Equation 12 and when the assumption holds that the source of nucleation won't be exhausted then 12 can also be written as Equation 13.

$$\dot{N} = K_4 N_L exp\left[-\frac{\Delta G^*}{\kappa T}\right] \quad (13)$$

K_4 is a constant and N_L is the total number of atoms in the liquid per unit volume. ΔG^* is the activation free energy for the formation of stable nuclei. This is expressed in Equation 14 and is valid for homogenous nucleation.

$$\Delta G^* = \frac{16\pi\, \gamma_{SL}^3 T_m}{3\, L_v^2\, \Delta T^2} \quad (14)$$

Equations 12-14 show that the rate of nucleation is also dependent on the amount of undercooling. As ΔT increases then the size of nuclei decreases and a larger amount of them form. The proceeding equations are valid for nucleation of crystals from the melt. It is more common for crystals to nucleate on the mold walls or other surfaces that the melt is in contact with, such as non-dissolved particles. This is termed heterogeneous nucleation and takes into account a reduction in the necessary free energy change to nucleate a crystal. The reduction in the required free energy change is due to a reduction in the interfacial area between the crystal nuclei and the melt as the nuclei forms on the mold wall or particle in the melt. Modification of the critical free energy reduction for stable nuclei is given in Equation 15 with the modification to the nucleation rate given in Equation 16.

$$\Delta G_{het}^{*} = \frac{16\pi\gamma_{sl}^{3}T_m^{2}}{3\,L_v^{2}\,\Delta T^{2}}\,\frac{\left(2-3\cos\theta+\cos^{3}\theta\right)}{4} \tag{15}$$

The second term in the Equation 15 is a shape factor $f(\theta)$ that reduces the free energy reduction requirement. The angle θ is the wetting angle the nuclei make between the mold wall and the liquid/nuclei interface.

$$\dot{N} = \frac{D_L\,2\pi r^{*2}\,(1-\cos\theta)}{a_0^{4}} N_a exp\left[-\frac{16\pi\gamma_{sl}^{3}T_m^{2}V_m^{2}\,f(\theta)}{3\kappa\Delta H_f^{2}T\Delta T^{2}}\right] \tag{16}$$

N_a is the number of surface atoms of the nucleation site per unit volume of liquid, D_L is the liquid diffusivity, and a_0 is the lattice constant. Heterogeneous nucleation reduces the amount of undercooling necessary to form stable nuclei of a given radius.

The degree of undercooling will also determine the solidification velocity by which the nuclei form into grains. In a diffuse interface between the solid and liquid, the solidification velocity has a linear relationship with the kinetic undercooling ΔT_k. The kinetic undercooling is the difference between the melting temperature and the temperature of the liquid at the solidification front. Equation 17 details the growth velocity relationship for this type of solidification[21]

$$V = \beta\frac{D_L}{D_{LM}}\Delta T_k \tag{17}$$

where β is a constant and D_{LM} is the liquid diffusivity at the melting temperature. As the growth velocity increases with increasing kinetic undercooling the crystal will incorporate more dislocations and defects as the diffusivity in the liquid decreases and the atoms have lower mobility to completely fit into the crystal lattice. The amount of undercooling will determine the size of the nuclei that forms, the number of nuclei that form, the rate of growth of the nuclei into grains, and to some degree the defect density.

2.3 Heat transfer

Investigation of the processing parameters and the resultant grain structure revolves around the amount of undercooling of the silicon melt in the core region at the beginning of solidification. This undercooling will be the result of the rate of heat loss from the silicon melt, which is the related to the rate of heat loss and heat transport through the silica cladding. A simple way to view rate of heat loss is to use Fourier's first law as stated in Equation 18 [22] where K is the thermal conductivity and A is the area of heat transfer.

$$Q = -KA\frac{dT}{dx} \tag{18}$$

Theoretically, at the moment of the drawing of the fiber, both the core region and the cladding will be at the same temperature. The amount of heat loss will begin at the surface of the fiber with a temperature gradient being established from the air/silica interface to the silica/silicon interface. The rate of heat loss in the core region will be determined by the thickness of the cladding region and the thermal conductivity of the

silica in that temperature range. It is assumed in this approach that the heat conducted to the surface is removed through convection and radiation and that there is no increase in temperature at the fiber surface.

At the temperatures that are necessary to draw the silica into a fiber the other main mode of heat transfer is radiant energy. Heat will transfer from the molten silicon core to the surrounding area through the cladding. If the cladding material does not participate in the transmission of the radiant energy, a simple solution exists that follows the Stefan-Boltzmann equation. This is shown in Equation 19, where σ is the Stefan-Boltzmann constant, T is the temperature of the core and A is the area of the core emitting.

$$q = \sigma T^4 A \tag{19}$$

In this case the rate of cooling of the core will be greater for a larger core. However, the amount of heat that is contained will also increase with the increase in core diameter. The amount of heat that is contained versus the amount radiated will scale with the radius. The peak wavelength of the emitted radiation for the temperatures that the fibers will be pulled at is within the transmission window of silica at around 1.3 μm at 2000 °C. This is not the low loss portion of the silica window so the cladding may become a participating media in the heat transfer. Due to the complexity of the heat transfer if the cladding participates in the heat transfer a solution or model is not put forth to calculate how the cladding and the core diameter will affect the heat loss. The actual heat transfer solution is complicated as it must take into account both radiation heat transfer from the core and

from and through the cladding and the convective heat transfer from the surface of the fiber and any increase in the temperature of the environment surrounding the fiber.

2.4 Crystal Growth Mechanisms

The rate of cooling of the core is going to influence the crystallization of the core. The different methods of growing silicon crystals are presented in the next section. Single crystals are primarily grown either using the Czochralski or float zone method. Each process has its own advantage depending on the application of the silicon. The single crystal methods are slow growth methods and are close to equilibrium processes in order to allow for proper crystal orientation to develop with a minimum amount of defects in the crystal. The process of crystal growth in the fibers is unknown but it is expected to be a highly non-equilibrium process.

2.4.1 Single Crystal methods

Czochralski

The first method developed to grow single crystals was the Czochralski method. Originally done by pulling thin fibers of metal from a melt pool, these fibers were of small diameter so that the latent heat of fusion could be dissipated quickly enough for the single crystals to form as the fiber was being drawn. This method requires that the growth of the single crystal start with the contact of a single crystal seed with a melt pool. Contact with the melt pool allows the molten material to bond to and arrange atoms onto the surface that's in contact with the pool. The seed crystal is slowly withdrawn from the

melt pool at a rate that allows the heat to dissipate so that the crystal orientation is maintained. As one layer solidifies, the molten silicon below remains attached to the seed crystal by capillary pressure. The size and shape of the liquid column is determined by the size of the seed crystal and the surface energy of the molten material. Rate of removal of the crystal from the melt pool is determined on the basis of the size of the column and the time necessary for heat removal to allow for orderly solidification of the column. Process variables are significantly more complicated than presented. Growth rates for most 300 mm crystal boules are on the order of 3-5 cm/hr.[23] The Czochralski method grows crystals of good quality but contamination is a potential concern and may result from the crucible that holds the melt pool for an extended period of time while the boule is being drawn.

Float Zone

Float zone crystal growth was originally developed and used to refine materials through the use of the partitioning of impurities during the solidification process. This process is also useful in the growth of single crystal high purity semi-conductors. In float zone crystal growth a rod of the material is attached to a seed crystal. The area around the seed crystal is heated by a thin profile furnace so that only a small portion of the rod is melted. As this is drawn through the furnace, the part of the melted portion solidifies with the rejection of the impurities into the unsolidified portion. This process is continued until the end of the feed rod is reached with most of the impurities being contained in the end portion of the feed rod. Speed and size of the rod is controlled so as to grow high purity low defect single crystal material. The size of the final crystal is dependent on the surface

energy and tension of the material, but for silicon a maximum diameter of 200 mm is commonly made. Feed speed for this process is in the range of 3-5 mm/min.[24]

3. Materials and Methods

Investigation of the feasibility of making semiconductor core optical fibers led to the development of the fabrication process for 4 different fibers types and an experiment to determine the influence of the fabrication parameters on the grain structure. The types of fibers are separated by the core material and were high purity silicon, n-type doped silicon, p-type doped silicon, and n-type doped GaSb. Each fiber is given its own subsection in each of the proceeding sections. All Optical transmission characterization of the silicon, n-type and p-type silicon and the n-type GaSb fibers was done by Dr. Ke Wang.

3.1 Silicon Fiber

The fabrication of silicon fibers was accomplished to determine the feasibility of making experimental lengths of semi-conductor core optical fibers on the drawing system that was present at the time of development. It was necessary to see if optical fiber sized silicon fibers could be made and what type of core shape, size and length was producible.

3.1.1 Fabrication

The silicon fibers were drawn from a preform that was made with a powder-in-tube technique. High purity (99.9%) silicon metal powders were placed inside an optical purity grade silica tube, with an approximate OD of 12 mm and an ID of 10 mm where

one section of the tube was modified by prior flame working. The silica tube was modified to include a neck down region immediately preceding a closed end to have a volume for placing the silicon powders. This region was about 5 cm in length with an approximate OD of 4 cm and an ID of 3 cm. Fibers were drawn from the preform on a small glass lathe with a draw length of approximately 0.3 m. The fiber drawing system has two chucks, which are used to clamp the glass preform and can spin together or separately at precisely-controlled speeds. The second chuck can also be moved linearly which draws the fiber from the preform when heated by an oxygen-hydrogen torch to a temperature well above the silicon melting point and above the glass softening point, where the viscosity was suitable for drawing. The typical drawing temperature for silica fibers is in the range of around 2000 °C. A schematic of the preform used during drawing is shown in Figure 3.1.

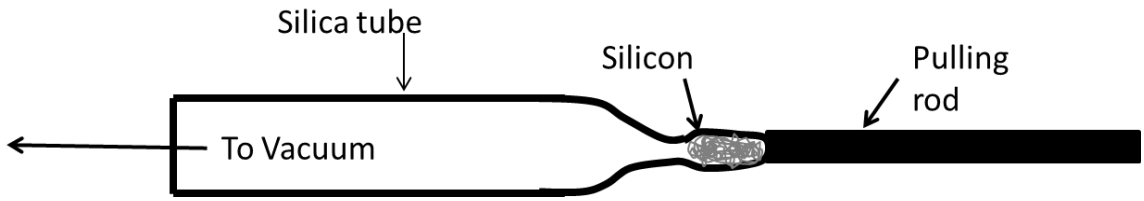

Figure 3.1 Schematic of silicon fiber preform

The preform was clamped in one of the chucks, and a silica rod was clamped in the second chuck and then fused to the end of the preform. During heating, the preform was rotated to evenly distribute the heat from the flame about the circumference of the preform. The silica rod served to support and allow mechanical force to be imparted on the heated preform. A vacuum was applied during the fabrication process in order to

remove air from the preform. The vacuum was maintained as the preform was heated and during the fiber draw. When the preform was heated by the torch to above 1900 °C, the silicon metal melted and the silica tube softened, at which point fibers were drawn from the end by translating the second chuck along the stage it was mounted on. Many different diameters and lengths of fibers were produced with the fabricated fibers having lengths up to 7 cm.

3.1.2 Characterization

The silicon fibers were characterized optically using a Zeiss microscope. In addition to the optical characterization, the fibers were viewed using a scanning electron microscope. Identification of the core material was done through the use of Energy Dispersive spectroscopy (EDS).

3.2 N-type Silicon Fiber

3.2.1 Fabrication

Fabrication of the n-type fiber started with the making of a powder-in-tube preform. The preform was made by sealing one end of an optical-grade silica tube by heating the center section of the tube and pulling it to a point, which produced a closed end. This method eliminates contamination of the tube interior by water vapor produced by the oxy-hydrogen flame. The tube had an outer diameter (OD) of 6 mm and an inner diameter of 2 mm. Doped silicon powder was then packed into the tube using a fused silica ram rod in conjunction with vibration. Doped powder was produced from doped silicon wafers that were fractured and then ground into a fine powder using a fused silica mortar and

pestle. The starting wafer had a sheet resistivity of 100 Ω•cm with a <100> orientation corresponding to a doping density of $1x10^{15}/cm^3$. Fibers were drawn on a similar setup as used for fabricating the un-doped silicon fibers. Modifications were made to the setup by having one of the chucks attached as a motorized linear stage. When the preform is heated by a hydrogen-oxygen torch, a fiber can be drawn by moving the stage at a controlled speed. A schematic of the n type preform used during fiber pulling is shown in Figure 3.2.

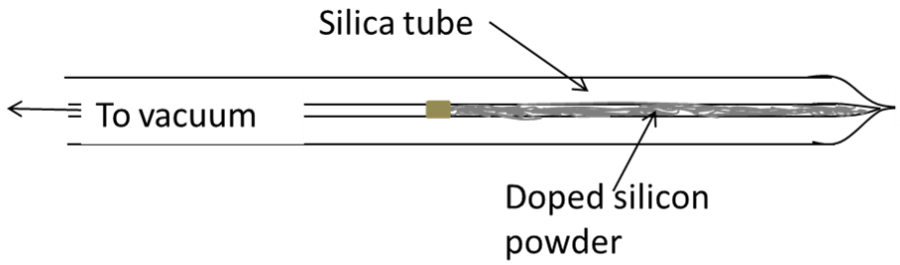

Figure 3.2 Schematic of n-type silicon fiber preform

In the experiment, the preform was secured in the fiber drawing system with one end in the non-movable chuck end and attached to a vacuum system. A silica rod was secured into the motorized chuck and then fused to the end of the preform. The vacuum system was used to evacuate the air from the tube in order to prevent potential oxidation and the formation of crystalline and amorphous silica during any heating of the preform during the fiber drawing process. A hydrogen-oxygen torch was used to heat the preform to a temperature above 2000 ºC, based on the glass viscosity observed during the fiber draw. When the silicon powder was molten and the silica tube sufficiently softened, the torch flame was removed and then the secondary chuck was moved in the linear direction to draw a fiber from the preform. This technique produces fibers of different diameters

depending on the temperature and the linear pulling speed. Fibers with overall diameters from 200 µm to 1000 µm and lengths from 50 mm to 120 mm have been fabricated. Fabrication of the fibers in this manner allowed for real time adjustment of the pulling conditions during the fiber drawing process in order to produce continuous lengths. Figure 3.3 is an image of the modified glass lathe that was used to pull the n-type silicon fibers. The controls on the glass lathe allow for precise control of the linear speed of the both the torch platform and the tailstock that holds the motorized chuck. Speeds can be adjusted from 0-5.5m/min in increments of 0.1 mm/min. These controls provide for controlled heating of the preform by moving the torch platform along the preform at the speeds necessary to heat the preform thoroughly and uniformly. The tailstock motor can be controlled in combination with the torch platform to give a pulling condition specific to the preform.

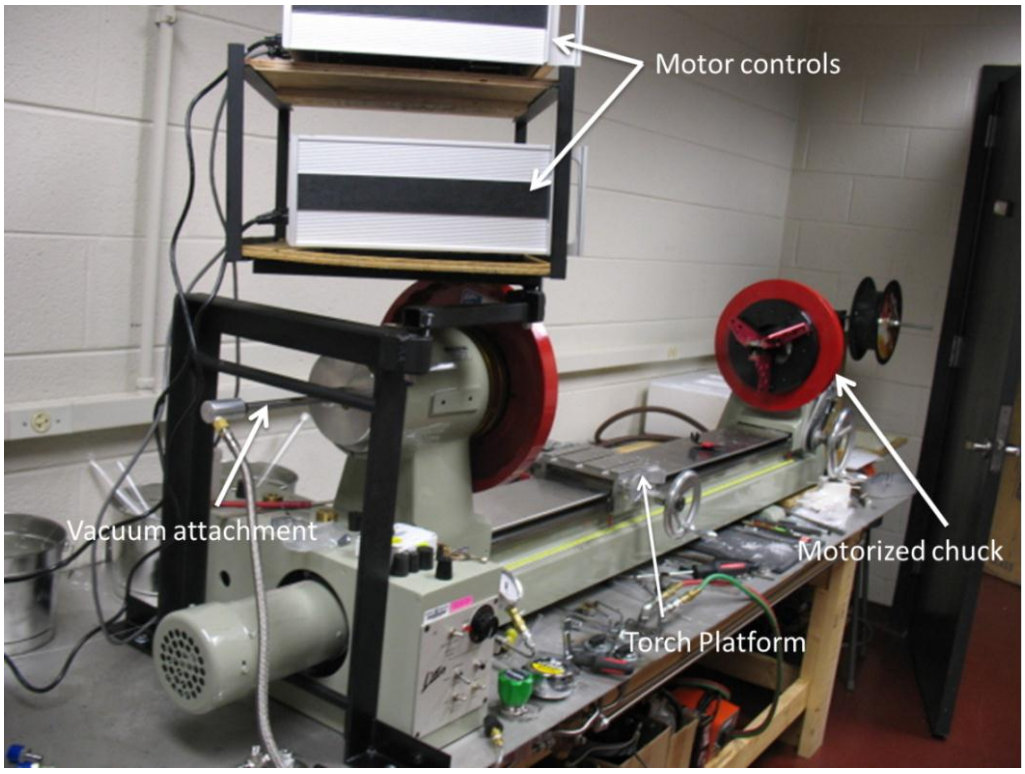

Figure 3.3 Modified glass lathe for pulling experimental fibers

3.2.2 Characterization

Optical

The optical transmission was tested through a butt-coupling technique by a Micron Optics CTS system (SI-720) in the wavelength range from 1520 to 1570 nm. The fiber was mounted horizontally on an optical stage and axially aligned with lead-in and lead-out single mode fibers, which were mounted on two separated three-dimensional stages for precision alignment. Light was delivered from the CTS system through the lead-in fiber into the N-type silicon optical fiber. The transmitted light was then collected by the lead-out fiber and sent back to the CTS system for spectrum analysis.

Material

The n-type silicon optical fiber end face was imaged using a Scanning Electron Microscope (SEM). The composition of the fiber was characterized using Energy Dispersive Spectroscopy (EDS). The electron beam was set at an accelerating voltage of 20 kV, an aperture of 120 μm and a count time of 90 s. These setting were chosen to maximize the counts received during the line scan of the fiber end face. Verification of the phosphorous concentration levels was done with Secondary Ion Mass Spectroscopy (SIMS). Although using single crystal silicon powders, the crystalline orientation of the core is unknown after the fiber is fabricated, due to the core crystallizing out from molten silicon. In order to investigate the crystalline orientation of the silicon along the fiber axis, the fiber sample was mounted on a copper wire scaffold, mounted in Bakelite and then polished to the core region. Polishing of the sample started 240 grit SiC paper through 1200 grit SiC paper, followed by a 1 and 0.3 μm alumina suspension polished

and then finished with a 0.06 μm colloidal silica vibratory polish. Then the fiber sample was analyzed by Electron Backscatter Diffraction (EBSD)

3.3 P-type Silicon Fiber

3.3.1 Fabrication

The preform used to fabricate these fibers was made from optical-grade silica tubes in which a p-type silicon powder were tightly packed inside. Doped silicon powder was obtained by crushing doped silicon wafers and then grinding them in a silica mortar and pestle. Wafers were obtained from University wafer with a resistivity of 1-10 Ω•cm. This resistivity corresponds to a doping concentration of approximately $1x10^{15}/cm^3$. The tube was closed off on one end and had an outer diameter of 6 mm and an inner diameter of 2 mm. The preform was then secured in a horizontal fiber drawing system with the open end of the tube connected to vacuum. The preform was evacuated down to a pressure of approximately 3500 mtorr. Removal of the air is also thought to be a crucial step to prevent oxidation of the silicon and the formation of crystalline or amorphous silica during the fiber drawing process.

The p-type fibers were fabricated in the same manner that was described for the n-type fiber. The preform was secured in modified lathe while a torch heated the glass preform until the glass had a sufficiently low viscosity and the silicon in the core was molten. This technique produces fibers with various dimensions depending on the temperature of the preform and the speed at which the fiber is drawn from the preform. Fibers with outer diameters from 200 μm to 1 mm and inner diameters from 10 to 200 μm were fabricated

3.3.2 Characterization

Optical

Optical transmission of the p-type fiber was measured by a Micron Optics CTS system (model number SI-720) with a spectral range of 1520-1570 nm on a 4 cm length of fiber with a 100 micron core diameter and cladding diameter of approximately 450 microns. The fiber was mounted on an optical stage and axially aligned with the lead-in and the lead-out single-mode fibers, which were mounted on separate three-dimensional stages for precision alignment. Light was delivered from the lead-in fiber into the testing fiber. Then the transmitted light was collected by the lead-out fiber into the spectrometer. The transmission includes the lead in and lead out fiber coupling loss associated with setup. The length of the fiber was too short to determine the loss per cm using the cutback method.

Material

The end face of the p-type silicon optical fiber was imaged by SEM. The sample that was imaged solely by SEM was mounted on a sample stub with silver paint and polished to produce a flat end face. EDS was used in order to determine the material composition of the fiber. A sample for EDS was mounted onto a sample holder with carbon tape after the fresh fracture surface was created by scribing and breaking a portion of a fiber. The EDS was performed by setting the accelerating voltage to 20 kV, the aperture to 120 μm and the count time to 90 s. The p-type silicon optical fiber was also analyzed by EBSD and SIMS. Samples for EBSD were mounted onto a copper wire scaffold which was then mounted into a Bakelite container for polishing. Two polished surfaces were prepared.

They are the end face and the surface along the fiber axis. Samples were polished down by a 0.3 μm alumina polishing media and then polished on a vibratory polisher using a 0.05 colloidal silica suspension. Samples for the SIMS analysis were mounted in 99.99% pure indium after the end face of the fiber was polished on 1200 grit paper.

3.4 N-type GaSb

3.4.1 Fabrication

Starting materials for the core region of the fiber were obtained from University Wafer as a 2" Te doped GaSb wafer with a doping concentration of $10^{17}/cm^3$. Wafers with similar doping levels show a peak transmission of approximately 30-35% in the 2-5 μm range. The wafer was ground in a fused silica mortar and pestle until the wafer was reduced to a course powder particle size of approximately 1 mm. The powder was then inserted and packed into a low softening point glass tube with a composition in the sodium borosilicate glass family of approximately 60 wt. % SiO_2 and the rest made up of Na_2O, B_2O_3, and Al_2O_3 with an inside diameter of approximately 3 mm. The tube was then connected to a vacuum source to reduce potential oxidation of the GaSb and to assist in the consolidation of the powder and collapsing of the tubing diameters. While the tube was being evacuated, the outer part of the tube was heated with a hydrogen oxygen torch to around the softening point of the glass. The temperature of the glass was approximated visually. Visual approximation was possible due to the softening point of the glass being slightly higher than the melting point of the GaSb. During heating of the tube, the GaSb powder did not melt, while the tube experienced a contraction of the outside diameter. The contraction put the glass cladding into close contact with the condensed GaSb powder in the preform.

Fiber drawing was done on a horizontal drawing system which consists of two opposing rotatable chucks. One of the chucks held the preform, while the second chuck translates in the horizontal direction and held a pulling rod that is fused to the preform end. The preform was inserted into the primary chuck and a rod was fused to the end using a hydrogen-oxygen torch. Once the rod was fused to the end, a portion of the preform was heated until the GaSb was molten and the glass viscosity was sufficiently low. Fibers were then drawn from the preform end by translating the second chuck away from the preform end. Fibers were pulled from the preform at 5.5m/min, producing fibers with an outside diameter of 300 microns and core diameter of 100 microns. Lengths of approximately 0.8 meter were produced with lengths of around 0.4 meter having a consistent inner and outer diameter. The drawn fibers exhibited a uniform diameter over a substantial length of the fiber. Visual inspection of the fibers showed no indication of differences between the fiber segments. Core cracking and discontinuities were not apparent in any of the drawn fibers.

3.4.2 Characterization

Based on the homogeneity of the fibers, a sample was taken at random for SEM and EBSD analysis. While the draw lengths in these experimental runs are short in comparison to conventional drawing, the consistency of the drawn fibers indicates that a steady draw condition will produce good fiber properties, although further analysis of the fabricated fibers will be needed in order to confirm this. Fibers were characterized optically and with SEM, EBSD, and EDS. SEM and EDS were performed on the same

sample. A 1 cm sample was cleaved from a longer length of fiber and mounted onto a sample stub with conductive silver paint. The end of the fiber was then polished down to 1200 grit. EBSD samples were mounted onto a copper wire scaffold, which was then mounted in Bakelite. The entire mount was then polished down to 1200 grit, followed by a vibratory polish using 0.06 μm colloidal silica. The scan was conducted with a step size of 10 μm over the core region including sections of the cladding.

3.5 Grain Structure Fabrication Dependence Experiment

The materials and methods section is organized into two parts: materials and method of fabrication of the silicon optical fiber preforms; the methods used for the drawing of fibers and the analysis of the fibers produced. Fabrication of the preforms was a somewhat lengthy process that involved several steps. Those steps were the sizing of the silica tubes, formation of a preform casting structure, and the vacuum forming of the preform. The preforms were fabricated with outside diameters of 15 mm and 10 mm with a solid silicon core. Inner and outer diameters were achieved by inserting tubes of appropriate diameters into larger tubes until the correct diameter was achieved. The tubing was 214D silica manufactured by GE and the as-received tubing had significant variability in the inner and outer diameters making sleeving of the tubes impossible. Resizing of the silica tubes was done by etching the silica tubes with HF acid in order to decrease the O.D. of some of the tubes so that they could be inserted into other tubes to make the overall O.D. of the preform. Etching of the tubes was done after the tubes were cut to a length of approximately 300 mm. The tubes were placed in a full strength solution of the HF and left to soak for times ranging up to 300 minutes depending on the

amount the diameters needed to be changed. After the allotted time the tubes were removed and rinsed in running water for several minutes. Tubes were then checked for diameter change and if necessary they were immersed again in the HF solution until a suitable set of diameters was produced. Due to the variability of the silica tubes some clearance between the tubes when stacked occurred from the removal of silica from both the outside and inside diameter of the tubes. The tube stack used to produce a 15 mm and 10 mm outside diameter preform is shown in Figure 3.4. Inner diameters smaller than shown are produced by inserting an additional tube into the inner most tube in the tube stack. Tube sizes were chosen based on commercially available tubes that could be stacked together to achieve the desired outside and inside diameters.

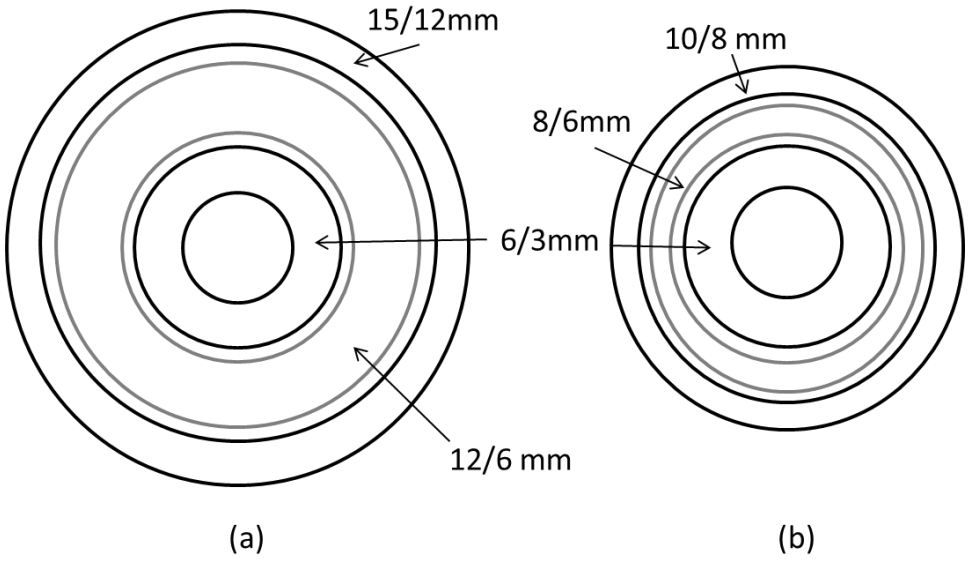

Figure 3.4 Silica tube stack schematic (a) 15 mm OD/ 3 mm ID (b) 10 mm OD/3 mm ID

The structure used to cast the silicon into the preform is constructed out of a silica tube that is shaped on a glass lathe into a bulb shape on one end and a necked down region on the other end. The bulb was also formed from 214 D silica tubing from GE. Necking

down of the tubing was done by chucking a section of tubing in a glass lathe and applying heat to a portion of the silica tubing using a oxy-hydrogen torch with a fan type torch tip. During the neck down, the tubing was rotated with the lathe for even heating and forming of the tube section. The torch was adjusted to get the tubing near the softening point. Forming was done once the silica was heated by applying pressure to the side of the heated section of the tubing with a 12 mm diameter graphite rod. The forming produced a neck down region in the tube with a thicker wall and inner diameter of approximately 2-3 mm. Once the forming was done the torch flame was moved over to the region that was to become the bulb. This heating caused a reduction of the ID of the tubing and increased the wall thickness. With reduction of the inner diameter complete, a section of the tubing was chosen and a neck down region was formed with a complete collapse of the ID. At this point the lathe tailstock was translated horizontally, pulling the bulb section away from the rest of the tubing. The end of the bulb was then heated while pressure was applied with a graphite paddle to increase the thickness of that region, which would be one of the main heating points during the casting of the silicon in the preform. With the bulb formed, the next step was the attachment of the sleeved tubes that make up the preform. In order to fuse the tubes to the bulb and allow for the application of vacuum to the inside of the bulb through the tubes, a hole was made in the bulb near the closed end. Forming the hole in the bulb was done by attaching a holed rubber stopper that was connected to a blow hose. A point on the bulb was heated and then air was blown into the bulb until a bubble was formed and burst to produce a hole. The hole was then enlarged to allow admittance of the smallest tube of the sleeved preform tubes. Tubing was fused to the bulb with the smallest of the tubes protruding into the interior of

the bulb. Gaps between the bulb and tubing were filled by fusing a silica rod into the area and heating and forming until all gaps were removed. A schematic of the silicon casting setup fabrication is shown in Figure 3.5.

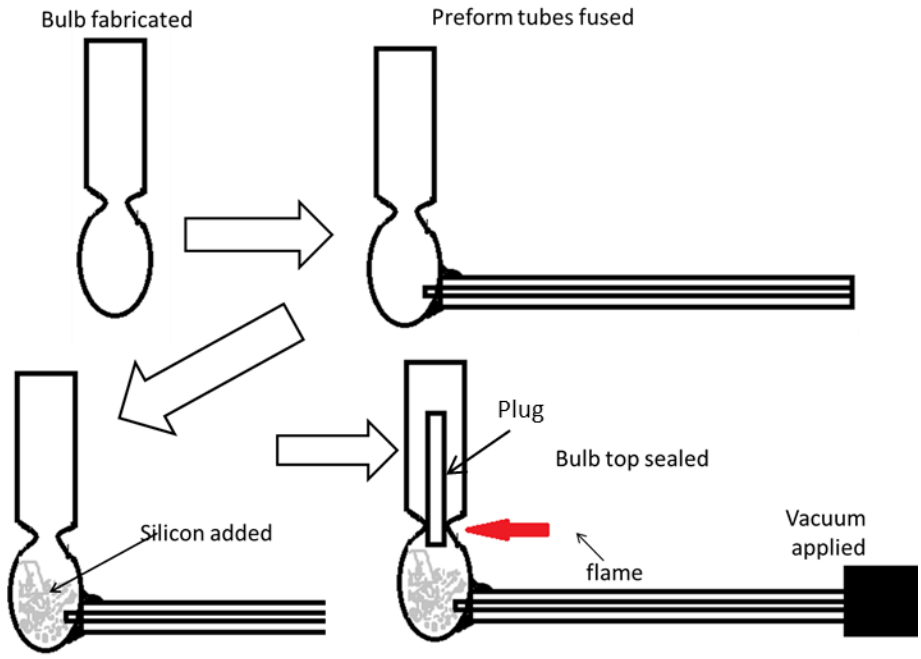

Figure 3.5 Schematic of fabrication steps in making the preform casting setup

In the initial preform fabrication steps, an effort was made to seal the gaps between the tubes by fusing glass to the face of the tubes with all of the tubes sleeved together except for the inner most tube. This manner of sealing the tubes was not always successful and during the vacuum casting of the preform, silicon was cast into the space between the tubes in some of the preforms. The vacuum casting of the preform was conducted with the preform casting structure housed in a refractory brick enclosure in order to reduce the heat loss during heating. With the preform casting setup in place, the open end of the tubing was connected to a vacuum. Vacuum was applied for approximately 1-2 minutes

with no heating. Then a low oxy-hydrogen flame was applied to the bulb of such intensity as to heat the silicon near the outer glass surface to a dull red color in order to drive off residual moisture. After preheating the bulb, additional heat was applied by increasing the hydrogen and oxygen flow to the torch tip until the silicon in the bulb melted and the silica glass softened. Heat was applied to the portion of the bulb opposite to the tube opening, and when the silicon blocking the opening melted, the vacuum pulled the molten silicon into the tube. Figure 3.6 is an image showing the refractory brick holder and a 15 mm casting preform structure during a portion of the heating process with an oxy-hydrogen torch.

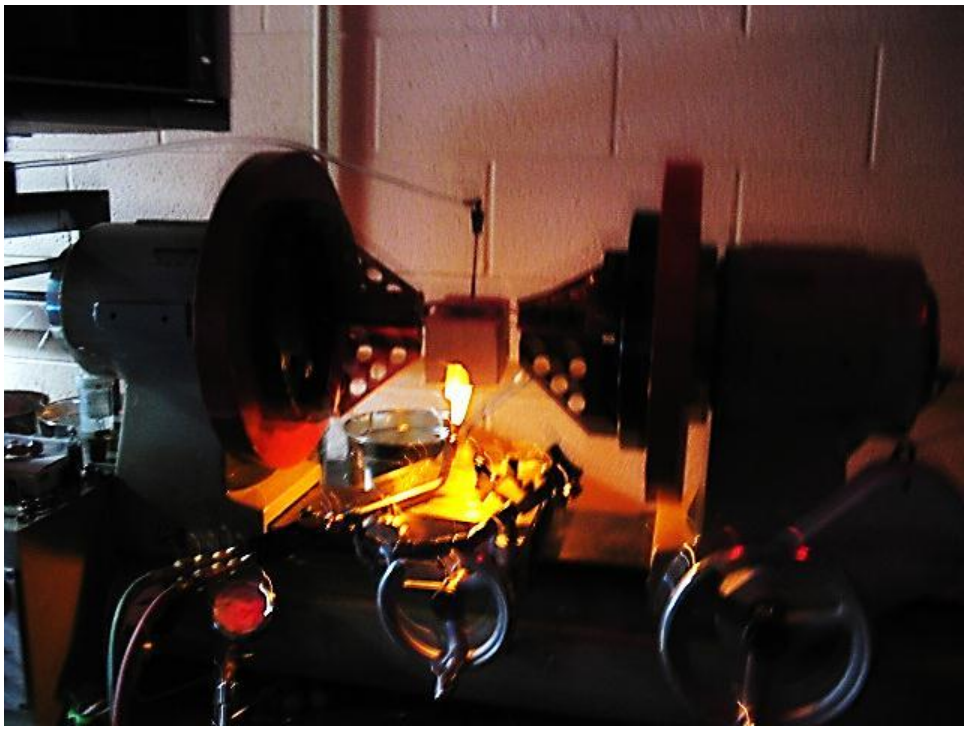

Figure 3.6 15 mm preform in the process of being heated prior to casting of silicon core

Depending on the heat in the area around the tube the length of silicon cast into the preform ranged from approximately 25 mm up to 150 mm. Images of vacuum cast preforms are shown in Figure 3.7 and Figure 3.8. Figure 3.8 details a preform with the

silicon cast between the tubes. During the process of casting the preforms, some silicon was vacuumed into the gaps in between the tubes. These portions of the preforms were also drawn out to produce fibers to see if the additional layer of silicon imparted a change in the cooling rate, grain structure or ability to pull the fibers to a desired dimension.

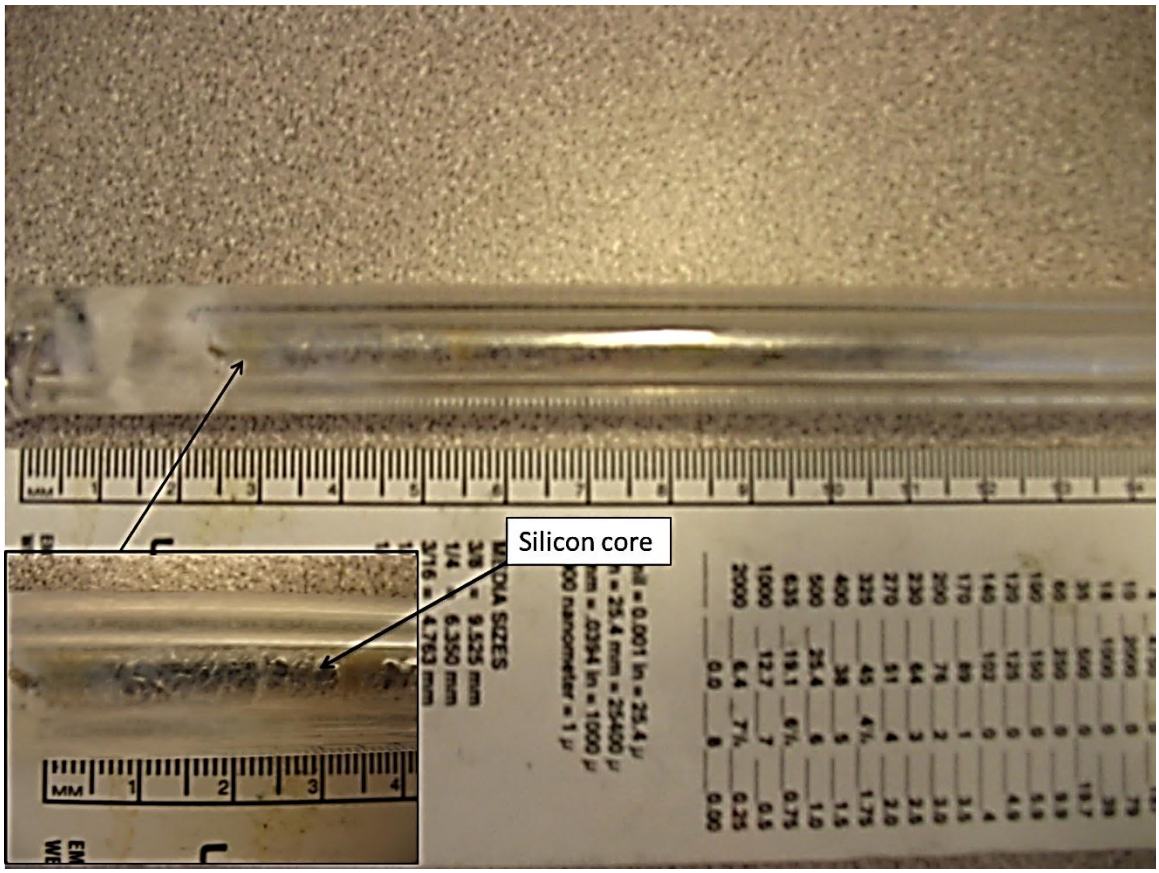

Figure 3.7 Vacuum cast silicon preform

The length of the silicon contained in the preform in Figure 3.7 is approximately 12 cm and is pointed out in the inset in the image in Figure 3.7. Inset into Figure 3.8 is the section of the preform where the silicon penetrated in between the tubes. When the silicon made its way into this space between the tube it was usually only in a small region like what is shown in the inset. The dark area to the side of the inset is the edge of the table that the preform was sitting on when the image was taken.

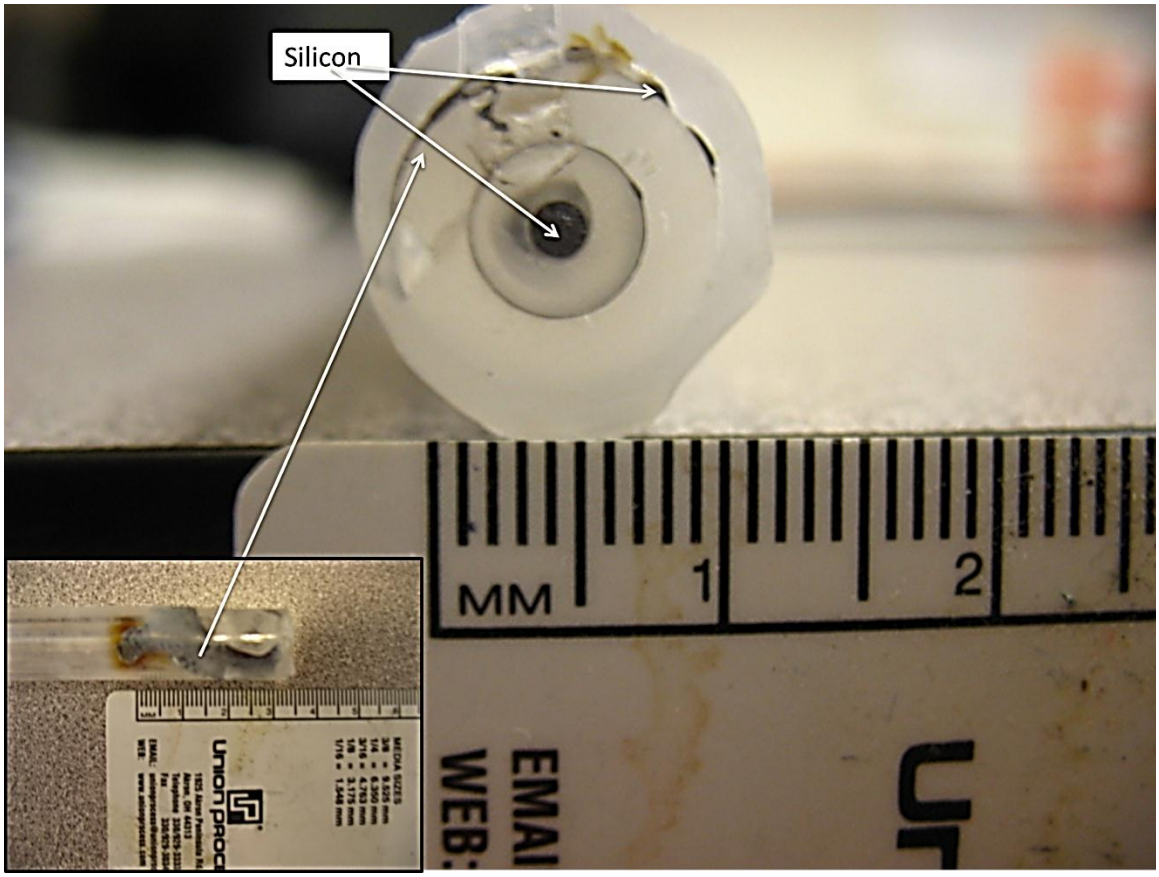

Figure 3.8 Vacuum cast silicon preform with between tube cast silicon

3.5.1 Fiber Drawing

Drawing of the fibers was done utilizing a glass lathe that was outfitted with automated controls that allowed for a specific preform feed speed and a specific fiber pulling speed. The preform feeding into the heat zone was accomplished by holding the preform in a fixed position while a carriage that holds the heating apparatus was translated horizontally away from the preform tip as a fiber was pulled. Fiber pulling was accomplished by translating the tail stock that was holding a rod that was fused to the end of the preform. With both the heating carriage and the tail stock, the available speeds are from 1 mm/min to 5500 mm/min with increments of 0.1 mm/min. The experimental

setup is shown in Figure 3.9 which details the heating carriage, automation controls, and the preform monitoring setup.

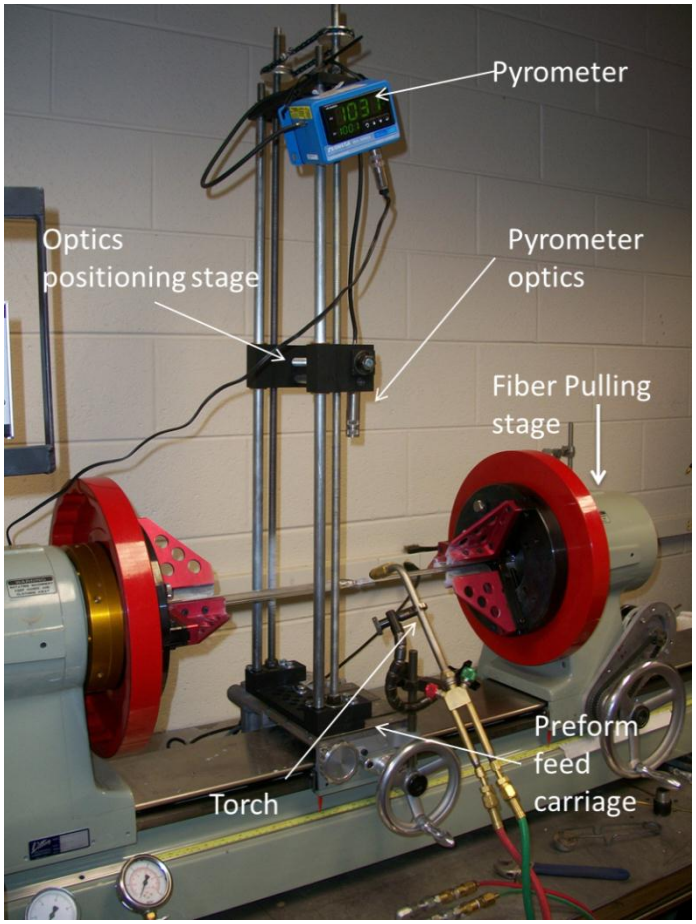

Figure 3.9 Fiber drawing experimental setup

Preform temperature monitoring was done utilizing an ir2c temperature controller with 2 color optical pyrometric temperature reading. The pyrometer optics was mounted onto a 2 axis stage and positioned so that it was reading the temperature of the preform just prior to the neck down region from which the fibers are pulled. Temperature of the preform was monitored prior to the pulling of the first fiber. The beginning and stable temperature of the preform was recorded as the fiber was pulled from the preform end. This was done for each fiber pulling event on all preforms.

Pulling of the fiber from the end of the preform was done in several steps. First the preform was chucked into the headstock and a pulling rod was chucked into the tailstock. The pulling rod was then fused to the end of the preform to aid in the efficient pulling of fibers from the end. Once the pulling rod was fused, the heating carriage was positioned so that the pyrometer optics could be aimed at the preform. With the pyrometer in position, the preform was then set to rotate at a speed of approximately 20 RPM. Heat was then applied with an oxygen-hydrogen torch using a Carlise 1382 torch tip to heat the preform. The torch tip was aimed at the side of the preform at approximately 90° angle from the pyrometer reading position.

The main experimental aspect of the fabrication was carried out by changing the fabrication parameters of preform dimensions, preform temperature, preform feed speed, and the fiber pulling speed. The inner and outer diameters of the fibers are a result of the starting preform dimensions, the temperature of the preform at the moment of pulling and the speed of the fiber pull. Preform temperature and pulling speed were determined experimentally. Outside to inside diameter ratios of the fibers should be maintained from that of the preform. To this end, the following ranges of preform dimensions were used and the target final fiber dimensions are listed in Table 3.1. These parameters were initially tested on GE 214D silica rods with outside diameters of 15 and 10 mm. The preform temperature was adjusted by controlling the flame intensity at the torch until a desired preform temperature was achieved. Feeding speed was adjusted from 4 mm/min to 50 mm/min depending on the starting preform temperature. The pulling speed was

started at 3000 mm/min and increased to 5500 mm/min with the maximum pulling speed dictated by the preform temperature and the previous pulled fiber.

Table 3.1 Preform dimensions and target fiber draw down dimensions

Preform number designation	Preform dimension		Fiber dimensions		Cladding thickness (μm)
	O. D. (mm)	I.D. (mm)	O.D. (μm)	I.D. (μm)	
1	10	1	200	20	90
2	15	1	300	20	140
3	10	2	200	40	80
4	15	2	300	40	130
5	10	3	200	60	70
6	15	3	300	60	120

Once the silica rods were pulled down to make fibers of approximately 200 μm and 300 μm outside diameters, the silicon preforms were pulled down in the same manner as the silica rods. The feed and pulling speed were recorded along with the direction of pulling and correlated were the inside and outside diameters of the fibers. Thirty four pulling trials were done across the 6 preforms. Samples were selected from the resultant fibers by sorting by outside dimension and grouped in increments of 50 μm starting with 200 μm up to 2 mm.

3.5.2 Characterization

Fibers were characterized optically for the inside and outside diameters. The grain structure of the core regions was characterized by EBSD. Optical analysis was done by taking a chosen section that was measured by a micrometer and cleaving one end to

present a clean fracture surface. The fiber end face was then roughly polished to present a flat surface for a more accurate measurement. The fiber was mounted onto a cylindrical die so the end face could be viewed, captured and the ID and ODs measured by the camera software. A Zeiss microscope was used to image the fiber and the image was captured utilizing an Axio camera with installed software for the image processing. Preparation of the samples for EBSD analysis was done by mounting the fiber sections onto a copper wire using Super Glue. The Super Glue was allowed to cure prior to mounting the copper wire assembly in Bakelite. The samples were then polished by starting with 80 grit paper and proceeding to 1200 grit paper. Samples were rinsed after each polishing step and blown dry with compressed nitrogen, sonicated for 5 minutes, and then rinsed and blown dry before the next polishing step. At the conclusion of the 1200 grit polish step the samples were thoroughly rinsed, sonicated for 10 minutes and then polished using a 1.0 and then 0.5 micron alumina suspension with the same cleaning step in between each stage. Following polishing with the alumina, the samples were rinsed and sonicated for 15 minutes and then polished on a vibratory polisher with a 0.06 µm colloidal silica polishing slurry. Samples went through the final polish step in increments of 20 minutes until a pattern that could be indexed during EBSD analysis was obtained.

4. Results and Discussion

4.1 Silicon fiber

Many different diameters and lengths of fibers were produced. The fabricated fibers had lengths up to 7 cm as shown in Figure 4.1.

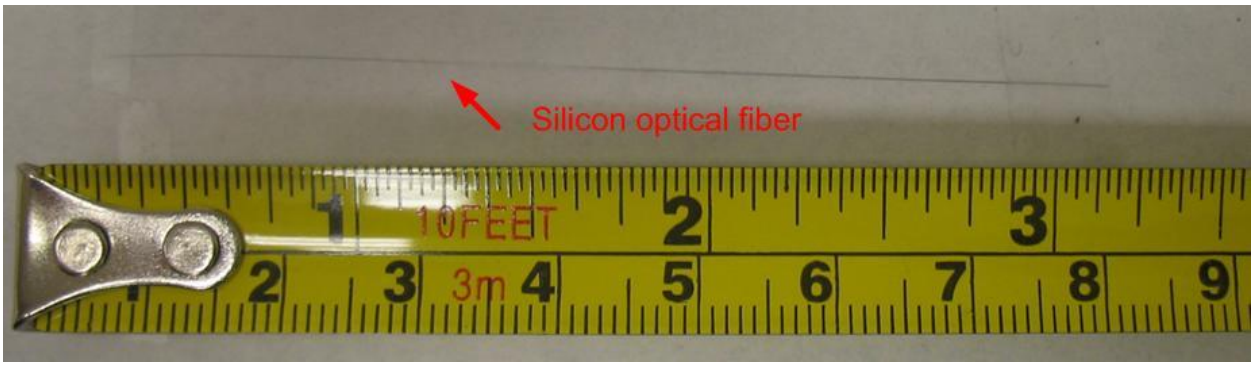

Figure 4.1 7 cm long silicon optical fiber

The reflected light optical micrograph and the SEM micrograph of 2 different diameter silicon fiber end face are shown in Figure 4.2 . In Figure 4.2 (a) the core is visible as the bright center spot in the image with a highly circular shape for the core. The SEM image in Figure 4.2 (b) is another silicon optical fiber and the core is the lighter grey color near the fiber center. A non-circular core is presented mirroring the non-circular shape of the outside diameter.

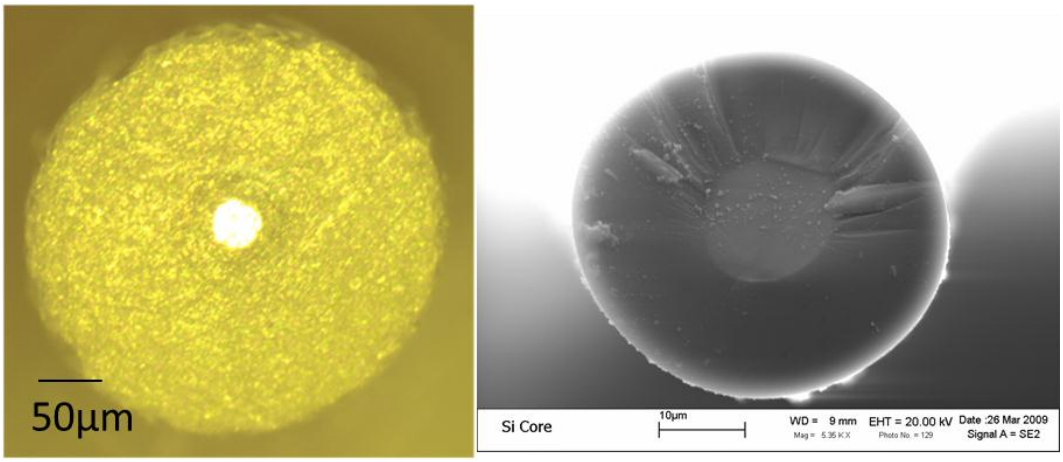

Figure 4.2 (a) Optical micrograph of silicon core fiber when the end face is illuminated by a white light (b) SEM micrograph of silicon fiber

EDS analysis of the fiber in Figure 4.3 (a) and (b) is in in the form of a compositional map of the fiber end face. The red map details the location where oxygen is present in the fiber and blue represents silicon. The core region is predominately silicon (blue) with little oxygen present (red).

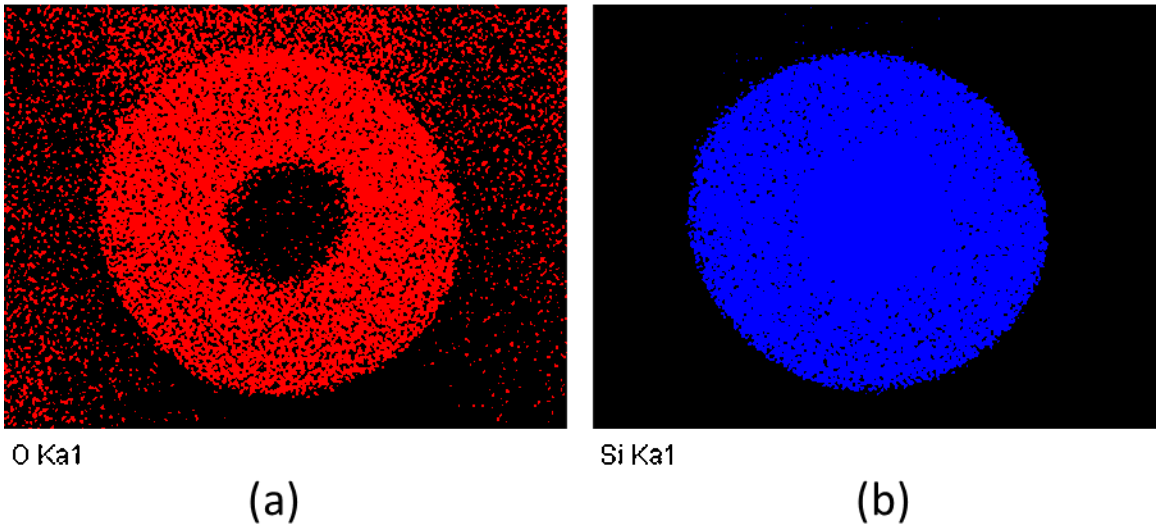

Figure 4.3 EDS map of silicon core fiber (a) oxygen map (b) silicon map

The EDS map of the silicon fiber end face in Figure 4.3 shows little or no oxygen present at the center of the core with the possibility of some oxygen present at the core-cladding interface. An absence of oxygen with the EDS indicates that the use of the vacuum helps to prevent oxidation of the silicon during the fabrication process. The irregular core shape in Figure 4.2 (b) indicates that there was uneven heating of the preform during the fabrication process. This causes the viscosity levels to vary across the cross section of the silica tube which in turn causes differences in the pulling of the tube at different parts of the tube cross section.

A quantitative compositional analysis was done with an EDS measurement of a spot on the end face of the fiber at approximately the center of the core. An SEM of the fiber end face that was analyzed with the EDS spot characterization is shown in Figure 4.4. Inset into the image is an EDS map of that fiber in the lower right corner and the compositional result inset into the lower left corner. The compositional analysis shows carbon and silicon present. The carbon that's present is contamination due to the fiber mounting process. Oxygen was scanned for, but none was found at the center of the core region. Oxygen might be present near the edges of the fiber, but due to the irregularity of the core-cladding interface getting a spot well placed was not possible.

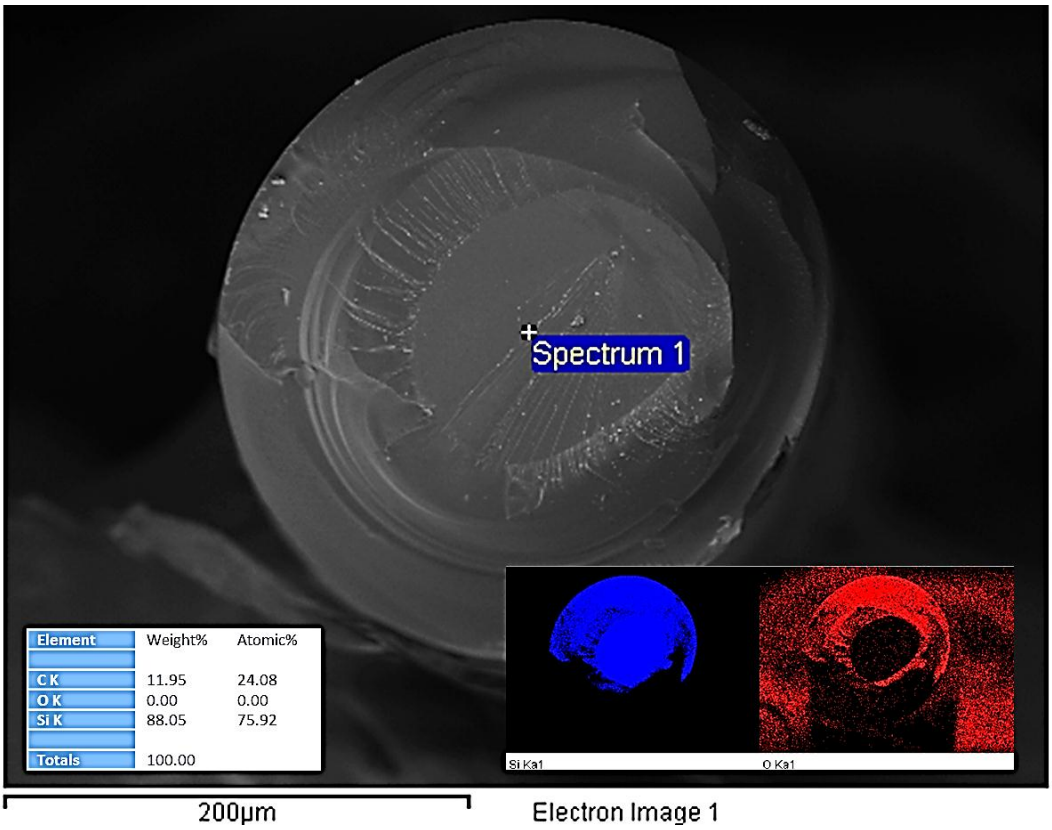

Figure 4.4 EDS spot location on silicon fiber (center), composition (inset left) and EDS map (inset right)

The optical transmission spectrum was also measured. The transmission spectrum is shown in Figure 4.5. The transmission was taken between 1520 and 1570 nm and a rough spectrum exists between those points. Overall coupling efficiency was highly related to the optical alignment and the surface condition of the fiber end faces of the silicon fiber.

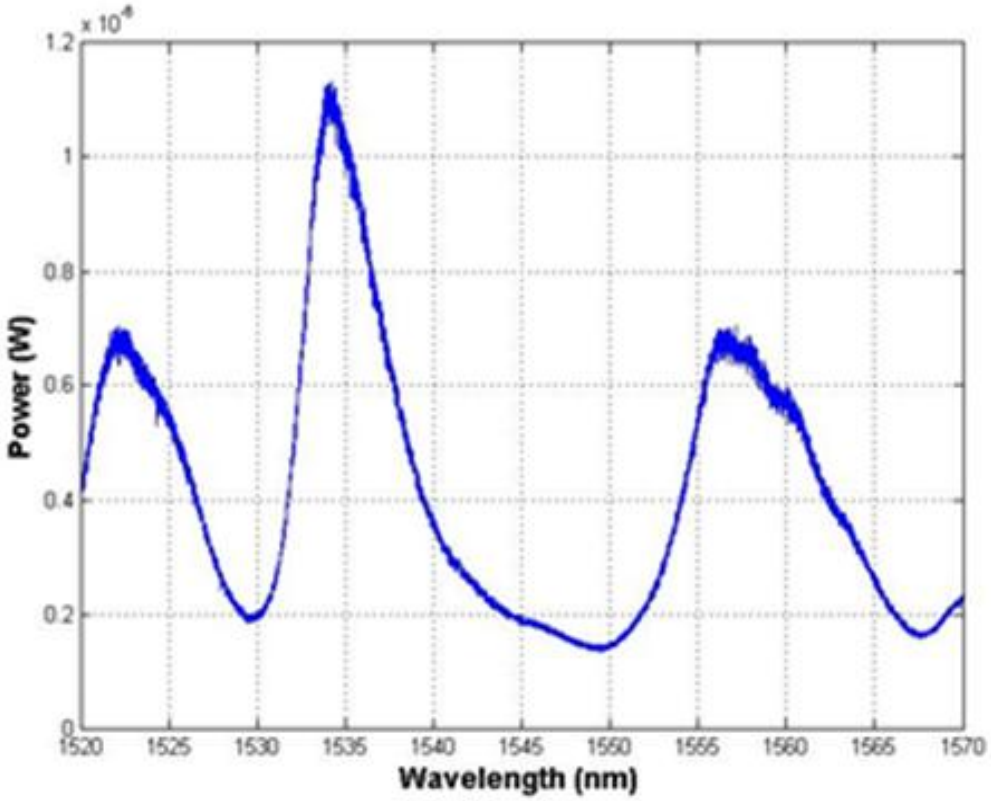

Figure 4.5 Optical transmission spectrum of a silicon optical fiber

The first published result of a silica clad silicon structure fabricated by a heat and draw method was done by the group at Clemson.[6] The structure that they fabricated was a cane with short lengths and larger diameters that would be considered traditionally outside of what is an optical fiber. These initial usable lengths of the fibers were around 5 cm and diameters around 1-2 mm. The structures fabricated in that work contrast from the fibers that were fabricated in this experiment, in that the lengths were around 7-8 cm

and diameters were on the order of 200-300 μm. While not significantly longer, the reduction in core diameter is and it shows the possibility of fabricating silicon core optical fibers that have flexibility and a length of core integrity. These fibers were pulled on a bed length of about 30 cm of which the preform, silica rod and tailstock took up approximately 20 cm of the drawable length leaving a maximum fiber length of 10 cm. Useable fibers that were fabricated on this system were almost the maximum possible length. In comparison, the silicon canes fabricated were around 5 cm while the possible fabrication lengths would only have been limited by the preform length. The high percentage of useable fiber from this draw system shows the feasibility of this method for fabricating long lengths of silicon optical fibers. The manner of formation of the core during the starting trials did not indicate that the small diameter fibers were possible. During many of the trials, the core would move out of the heat zone during pulling, resulting in only a small capillary tube. Other fibers pulled that did have silicon within the core region would explode upon freezing of the silicon. This initial fiber was drawn using a powder in tube type preform where the silicon was packed into a tube after a section of silica tubing was modified to hold the powder. During drawing, the tube was held under low to mid vacuum to minimize oxidation of the silicon while at elevated temperatures. In comparison to the other fibers published in the literature, these un-doped silicon fibers had low oxygen content in the core.[6] This is seen in Figure 4.3 where the core is entirely silicon with a few dots indicating oxygen at the core/cladding boundary. An EDS spot at the center of a core of the second silicon fiber sample is shown in Figure 4.4 and shows no oxygen present at that location. The resolution of EDS only allows for a conclusion that the oxygen content is less than 1 atomic percent. The previously

published fibers had a consistent concentration of oxygen of approximately 17 atomic percent across the core region.[6] The nature of the phase change of the silicon at the melting point added a level of difficulty in the fabrication step as the contraction of the volume of the silicon as it melts enables the silicon to more easily move about within the tubing. With the reduction of the volume, there is no hindrance to the movement of the silicon and since it was being drawn on a horizontal stage, the silicon could move in either direction within the confines of the tube. During this and subsequent draws in the silicon system while using the powder–in-tube type preforms, it was observed that the molten silicon that was flame heated would move along the shortest direction to escape the heat of the flame and recrystallize. This type of behavior was not noticed as much in the vacuum formed preforms, as the contraction was only due to the phase change, whereas the powder-in-tube preforms also had contraction due to the consolidation of the silicon particles and the removal of the airspace in between to add the total volume change of the silicon powder.

4.2 N-type Silicon Fiber

The n-type silicon optical fiber end face was imaged using an SEM, as shown in Figure 4.6. The fiber has a cladding diameter of approximately 590 μm and a core diameter of approximately 102 μm. Defects in the surface of the end face are a result of the rough polishing of the fiber prior to imaging. Polishing was done to a roughness sufficient to achieve a flat surface to facilitate EDS measurements. The silicon core is identified as the lighter grey circular region at the center of the fiber. A definite boundary exists between

the core and the cladding area, showing good formability and confinement of the silicon during the drawing process.

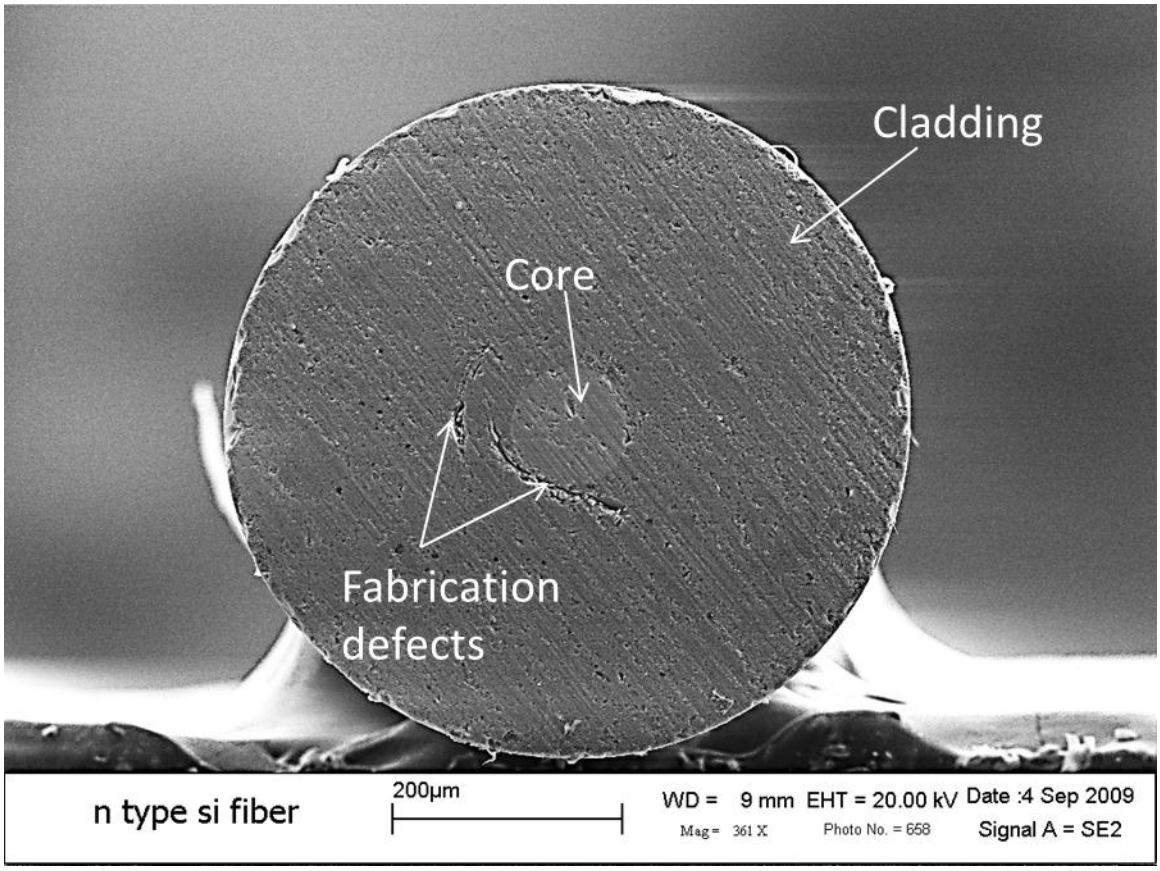

Figure 4.6 SEM micrograph of an n-type silicon optical fiber

The composition of the n-type silicon fiber was characterized using EDS. The electron beam was set at an accelerating voltage of 20 kV, an aperture of 120 µm and a count time of 90 s. These settings were chosen to maximize the counts received during the line scan of the fiber end face. The results are shown in Figure 4.7 (a) with the line scan overlaid onto the SEM image and the line scan legend in Figure 4.7 (b). The green line color represents silicon and the yellow line color represents oxygen. It can be concluded from Figure 4.7 that in the cladding region, both silicon and oxygen are present, but in the core region only silicon is present with no oxygen detected. The EDS detection limit is

approximately 1 atomic percent. This result confirms the presence of a silicon core and that oxidation of the silicon powder has been prevented during the fabrication process by evacuating the preform. However, the phosphorous was not detected because the concentration levels are below the EDS detection limit. Verification of the phosphorous concentration levels was done with Secondary Ion Mass Spectroscopy. A bulk phosphorous concentration of 5 x $10^{16}/cm^3$ was detected. The original doping concentration as derived from the resistivity value was $1x10^{15}/cm^3$ showing an increase in the phosphorous concentration in that portion of the fiber. Both values of the phosphorous concentration are above the SIMS detection limit of $2x10^{14}/cm^3$.

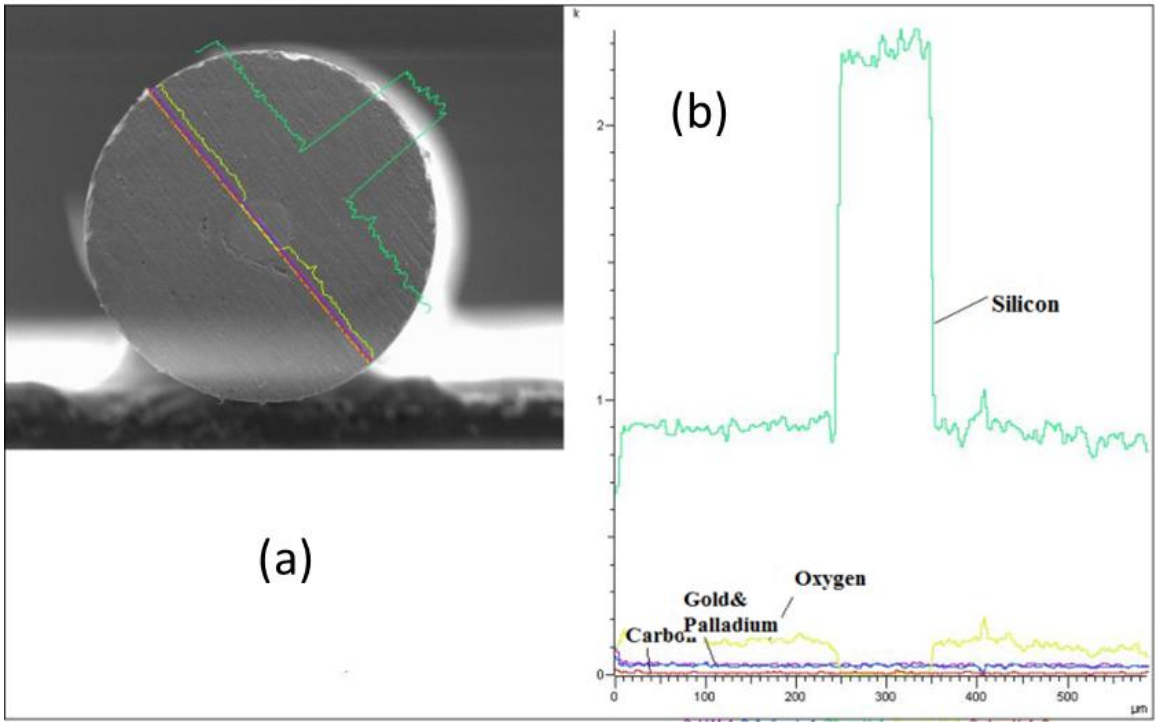

Figure 4.7 EDS mapping line scan of an N-type silicon core fiber end face (a) overlaid line scan (b) line scan

A difference in the core concentration over that of the original wafer indicates that partitioning of the phosphorous may be occurring. Since the wafer was not tested for

dopant concentration using the same system, the difference may not be as large as indicated by the SIMS measurement. If partitioning of the phosphorous does occur, then once the solidification kinetics of the core is understood, the partitioning of the dopant could be taken into account to allow for device fabrication.

Although using single crystal silicon powders, the crystalline orientation of the core was unknown after the fiber was fabricated, due to the core crystallizing out from molten silicon. In order to investigate the crystalline orientation of the silicon along the fiber axis, the fiber sample was mounted on a copper wire scaffold and then ground and polished to the core region. Then the fiber sample was analyzed by Electron Backscatter Diffraction (EBSD). As shown in Figure 4.8, each color region represents a unique crystalline orientation and a lattice marker is superimposed in that region. At least 5 crystalline orientations are observed in Figure 4.8. Therefore, the core is polycrystalline along the fiber axis, and is composed of a few large grains.

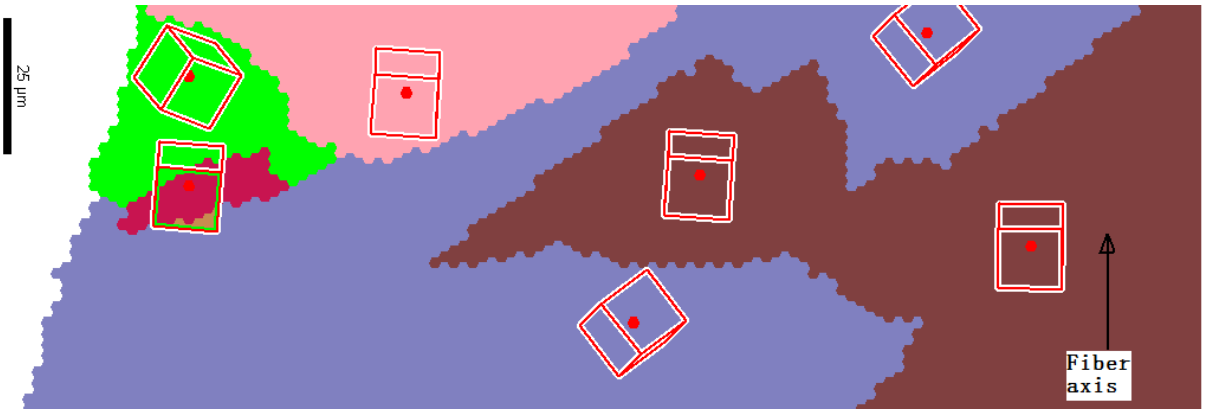

Figure 4.8 EBSD Crystal orientation map of silicon core viewed parallel to fiber

The optical transmission was tested through a butt-coupling technique and the transmission spectrum is shown in Figure 4.9. The overall coupling efficiency is highly

related to the optical alignment and is very sensitive to changes in the environmental conditions. At the time of measurement it was not known if the silicon optical fiber could be either cleaved or fusion spliced with regular fibers. Therefore, it is difficult to make an accurate numerical conclusion of the transmission loss at this time. A very rough estimation can be made by comparing the transmission of the n-type silicon optical fiber with that of a regular multimode fiber (MMF) (0.8 dB/km at 1310nm) under similar coupling conditions. For the butt-coupling technique, the optical quality of the testing fiber end face is significant because the rough end face will introduce considerable loss from scattering. The transmission spectrums of a well-cleaved MMF, an N-type silicon optical fiber and an uncleaved MMF are shown in Figure 4.9. In Figure 4.9, the spectrum of the n-type fiber has a periodicity which is attributed to reflections of the optical signal between the sample and the lead-in and lead-out fibers.

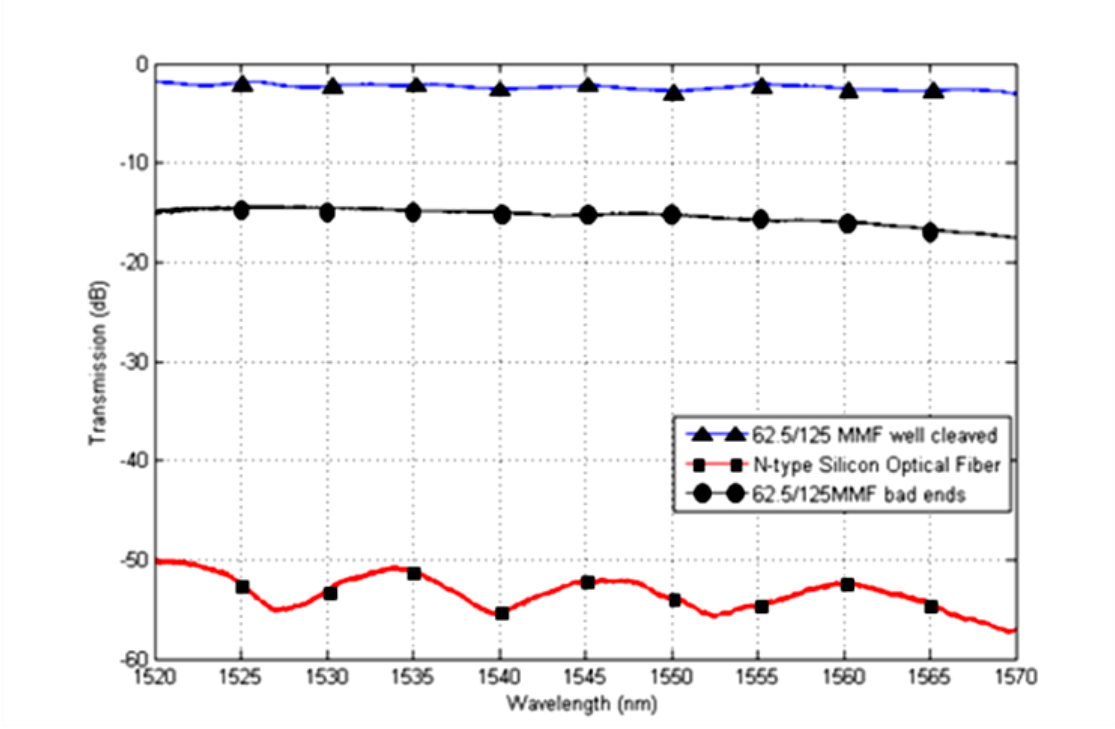

Figure 4.9 Optical transmission spectrum of an n-type silicon optical fiber in comparison to spectrums of a well cleaved MMF and an un-cleaved MMF

Besides the coupling conditions, the following factors are considered as main reasons for the loss from the fiber itself: (1) A transmittance of approximately 55% in the 1-6 μm range.[7] (2) Flatness of fiber end face, since from Figure 4.9, it can be seen that even for the same MMF, an uncleaved end face can easily induce 10~15 dB loss. (3) Uniformity of the silicon core and the core/cladding boundary. The irregularities at the core/cladding boundary will dramatically increase the loss. (4) Coupling losses between the lead in and the lead out fibers and the tested silicon fiber.

With the pulling of the initial silicon fibers it has been show that the method works to fabricate silicon fibers in the size range of optical fibers. The next step taken was the fabrication of doped silicon core optical fibers, as the main focus in this work was determining the feasibility of fabricating semi-conductor optical fibers that will allow for the construction of in-fiber electronic structures. The objective of the fabrication of the n and p type doped silicon core fibers was to demonstrated that the dopant doesn't appreciably leave the core and that the core maintains its crystalline nature during what is a highly non-equilibrium fabrication process. The process of fabrication of the doped core fibers was changed a little from the initial method of fabricating the silicon optical fibers. Changes include using a different tube size with uniform dimensions to increase the wall thickness of the preform, packing of the powder during fabrication of the preform and pulling of the fibers on a longer bed lathe that was specifically set up for fiber drawing. With the change in set up the fibers that were produced were of long lengths of approximately 50-60 cm relative to the 1m of useable bed length. These n-type

doped silicon core optical fibers were the first ever produced. The main limitation on the length of the fibers aside from the bed length was the contraction of the silicon during the phase change. This change limits the amount of silicon present in the hot zone that can be pulled into fiber form. The n-type fibers that were made from the powder-in-tube preforms had cladding diameters from approximately 40 to 600 μm and core diameters from approximately 20 to 100 μm. One of the larger fibers is shown in Figure 4.6 was chosen for SEM analysis due to the ease of handling and polishing of the fiber. In the SEM image the core/cladding boundary is visible and distinct. The core of the n-type silicon fibers is highly circular, which was not the case for the previously produced silicon fibers. This is thought to be due to the improved fabrication process and preform materials.

Elemental mapping of the fiber end face shows that the preliminary n-type silicon fiber has a silicon core and a silica cladding. Figure 4.7 details the compositional variation across the core and it can be seen that the level of oxygen content goes to near zero. The core contains no detectable amount of oxygen by EDS, which means that oxidization in the core is prevented by applying vacuum to the preform when drawing the fiber. Oxidation of the silicon may occur through oxygen diffusion through the silica during drawing but at levels below that detectable by EDS, or less than 1 atomic %.

Crystal orientation of the silicon core varies along the fiber axis as the silicon forms a polycrystalline structure during the solidification after being drawn into fibers. The silicon in the fiber core solidifies into a polycrystalline configuration with a

predominance of large grains which can have dimensions larger than 100 μm and this is seen in Figure 4.8. The core is composed of a few large grains of silicon and grain growth proceeds primarily parallel to the fiber axis. Oxidation of the silicon core material during the drawing process is not observed in the core. Most of the fibers fabricated are expected to be multimode. Through alteration of the fabrication and processing conditions, it is possible that a single mode fiber could be made by producing fibers of smaller core size and lower refractive index contrast between the core and cladding.

Optical transmission of these fibers shows a fair degree of loss as is shown in Figure 4.9 of around 45-50 dB. This can be attributed to several possible causes aside from the manner of coupling the lead-in and lead-out fibers. The fibers that were used for testing were of larger diameter. These larger diameter fibers from this group tend to have more cracks within the core region that propagate completely through the region. This cracking is the result of the expansion of the core material against the cladding at the silicon melting point of 1412 °C. At this temperature the silica cladding has a fairly high viscosity which resists the expansion of the silicon, thereby setting up a compressive stress state in the silicon. If the silicon is restrained significantly, the compressive stress will result in the formation of cracks. Crack formation was noticed with greater frequency in the larger core diameter samples. This can be explained by the greater amount of time it takes a larger core to reduce in temperature to the point of freezing. The longer time to freezing allows for the viscosity of the silica cladding to be at a higher value for the larger diameter cores than for the smaller diameter core fibers.

4.3 P-type Silicon Fiber

Optical and material characterizations of the p-type silicon optical fiber were conducted in order to determine the optical transmission, core composition, and crystallinity of the core. The end face of the p-type silicon optical fiber was imaged by SEM and is shown in Figure 4.10 where the core shows up as the darker grey region at the center of the fiber. A higher magnification of the end face is shown in Figure 4.11 where the interface between the core and cladding is visible.

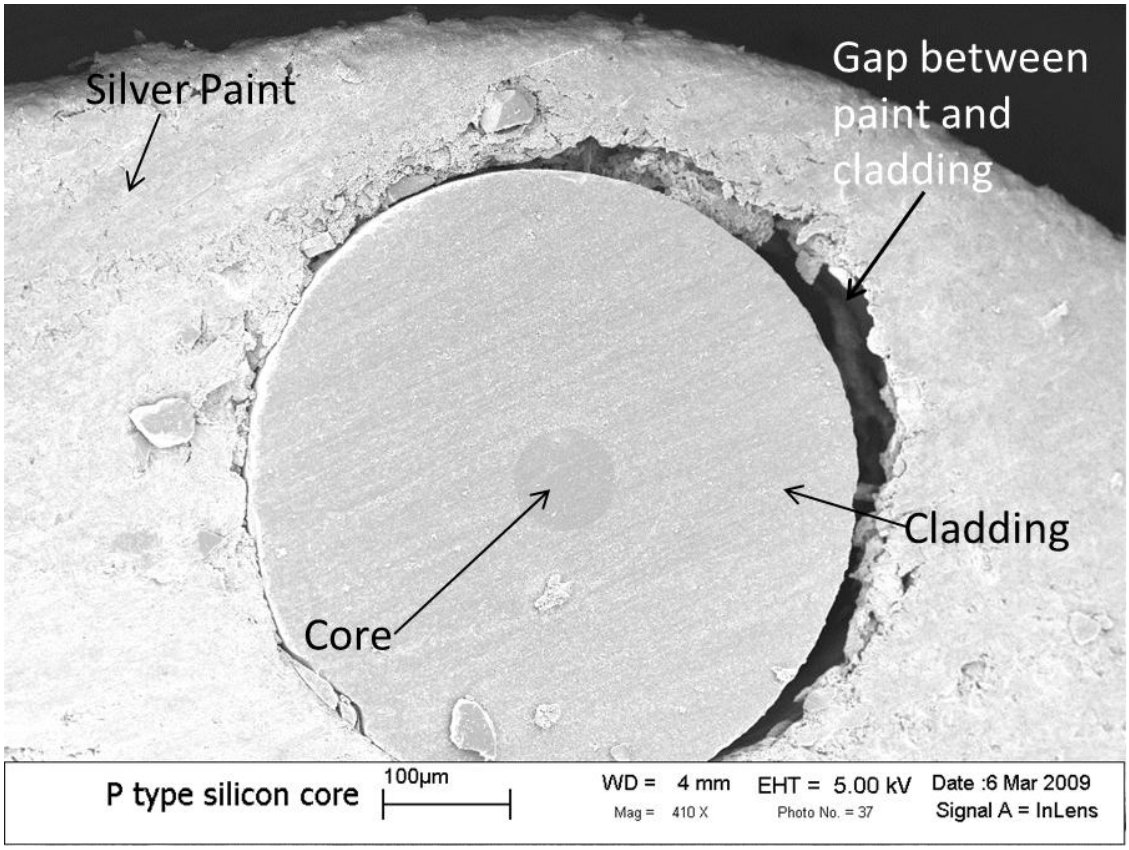

Figure 4.10 SEM micrograph of a p-type silicon optical fiber

EDS was used to determine the material composition and the sample used for analysis is shown in Figure 4.12(a) with the EDS line scan superimpose with the arrows indicating the element the line represents. In Figure 4.12(b) the detailed EDS elemental line scan is

shown which was taken along the diagonal direction of the fiber end face, where the blue color represents silicon; the green color represents oxygen and the red color represents carbon. The presence of carbon is contamination from the carbon tape used to attach the sample to the sample holder. It can be concluded that silicon is present both in the core and cladding regions but no oxygen was detected in the core region.

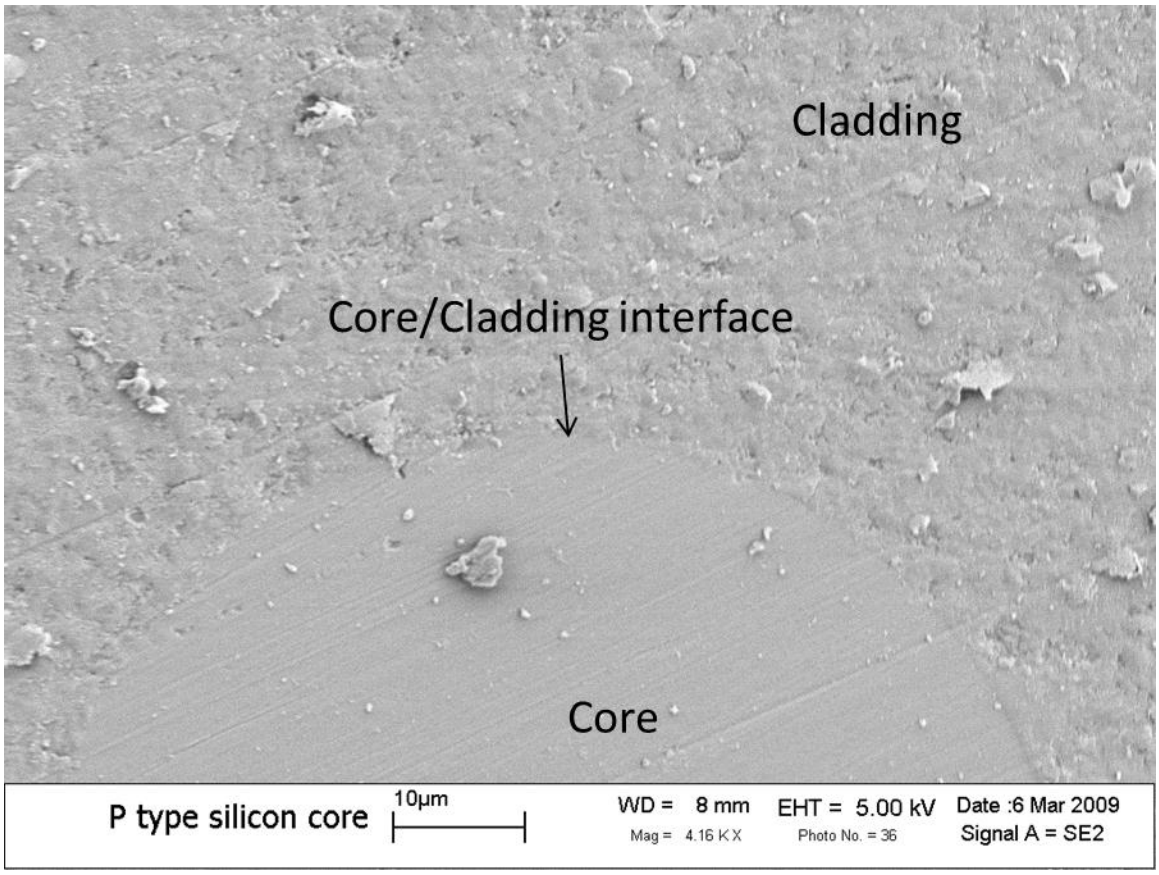

Figure 4.11 SEM micrograph of the core/cladding boundary in a p-type silicon optical fiber

The SEM images in Figure 4.10 and Figure 4.11 show that the p-type fibers are well formed as would be expected from the results in the n-type fiber fabrication. A clear and distinct boundary exists between the silicon core and silica cladding. While the boundary is distinct, the interface is also quite smooth as can be seen in Figure 4.11. Since the

solidification of the silicon is accompanied by a volume expansion, the smoothness of the interface would indicate that the cladding has a high enough viscosity to resist the expansion. If the viscosity was not sufficiently high, the growth of crystal facets would produce a rougher interface as they grew into the silica.

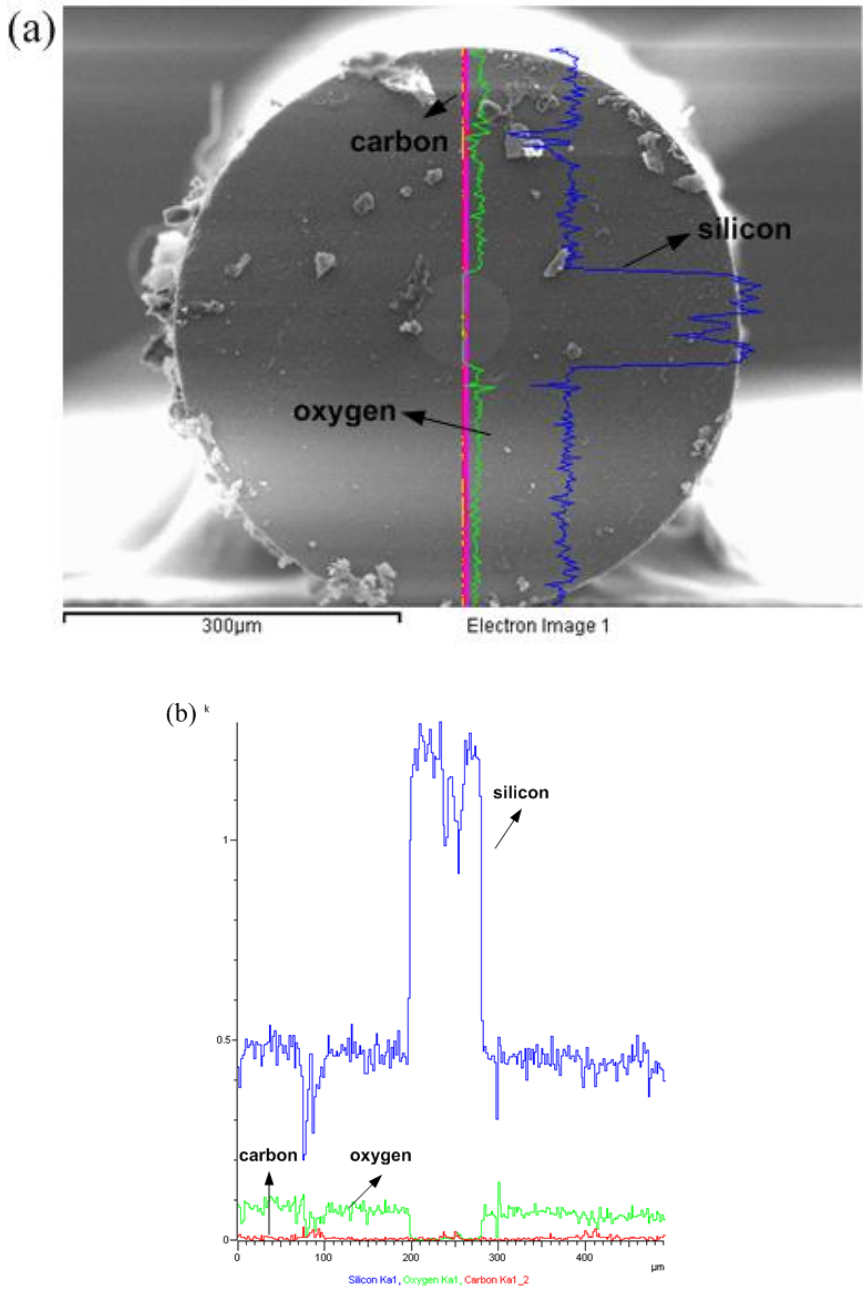

Figure 4.12 (a) The SEM micrograph and (b) elemental line scan of the p-type silicon optical fiber

The p-type silicon optical fiber was also analyzed by Electron backscatter diffraction and secondary ion mass spectroscopy. EBSD data is shown in Figure 4.13(a) and (b), where the crystal orientations along the end face and fiber axis are shown respectively.

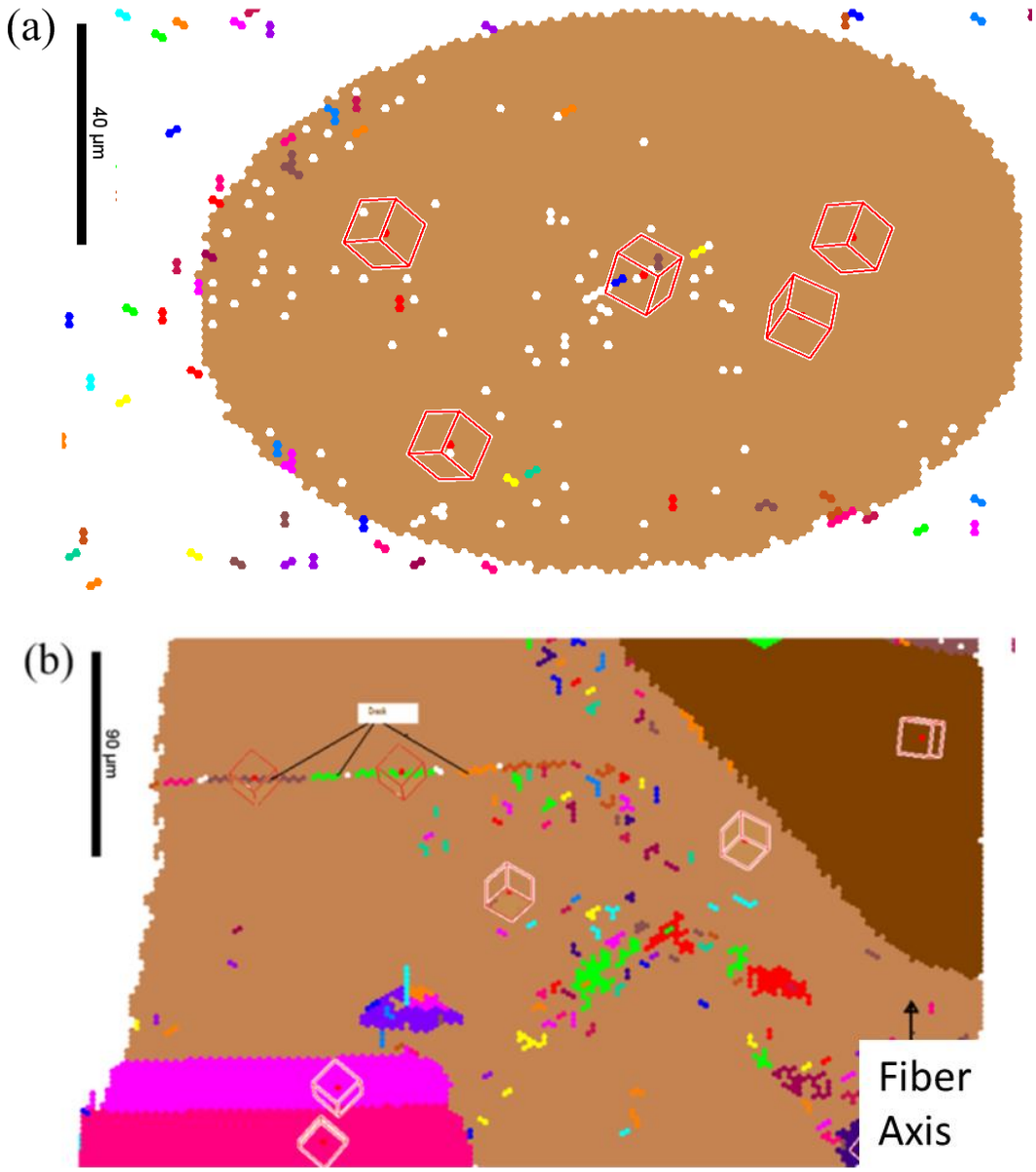

Figure 4.13 EBSD crystal orientation map of silicon core (a) in the end face and (b) along the fiber axis.

In Figure 4.13(a), the same color represents the same crystal orientation. Along with color, a crystal unit cell is superimposed onto the image indicating the orientation of that

particular grain. Areas in the image where there is no color or white are locations that were not indexed; either due to poor surface quality or the material is amorphous. Therefore, the end face of the fiber shows a single crystal orientation, while the surface parallel to the fiber axis is polycrystalline with very large grain sizes in the core, indicated by different colors in Figure 4.13(b). The elliptical view of the end face is due to the large mounting angle used during the sample analysis, which foreshortens the image in one direction.

The bulk concentration level of boron was measured through SIMS analysis, in which it confirms the presence of boron in the core region with a concentration level of $8.48 \times 10^{18}/cm^3$. Original concentration of the wafer was $1 \times 10^{15}/cm^3$. The increase in the boron concentration at that location is most likely due to the partitioning of boron from the liquid silicon during solidification. Optical transmission was measured by a Micron Optics CTS system (model number SI-720). The optical transmission was measured in the wavelength range between 1520 nm and 1570 nm and is shown in Figure 4.14. Transmission of the p-type silicon is comparable to the transmission of the n-type fiber shown in Figure 4.9.

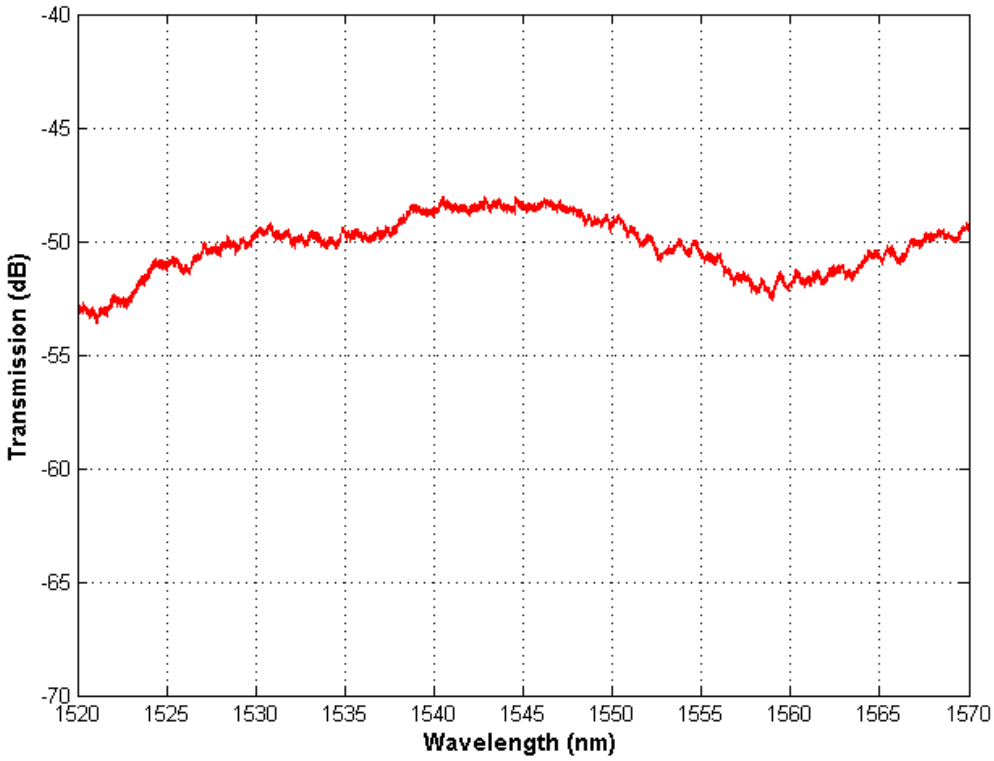

Figure 4.14 Optical transmission spectrum of the p-type silicon optical fiber

Compositional analysis of the fiber shows that it was a p-type silicon core optical fiber with oxygen levels below the EDS detection limit. The oxygen level as determined by EDS confirms that the vacuum system is crucial for the prevention of oxidization in the core when drawing the fiber from the preform. This is in comparison to the work in the literature where there is no mention of pulling a vacuum on the preform, while having an oxygen content of around 17 atomic percent.[6] Compositionally, the core cladding interface is also present in the sharp changes in the silicon and oxygen content as seen in the detailed EDS in Figure 4.12 (b).

The SIMS data tends to indicate some partitioning of the dopant during the solidification process. Both the phosphorous and boron levels were measured to be greater than what is expected from the original wafer resistivity. Only one sample for each was done and the original wafers were not analyzed for the dopant content. While there may be partitioning of the dopants during solidification, too little data exists to make a conclusion. Even with the potential increase in the doping level of one area or decrease of dopant in another area, this still allows for the development of in-fiber devices. Any partitioning that occurs will follow in the direction of solidification and once the relationship is understood how it starts and travels in the fiber, it can be planned for when fabrication of the structure is undertaken. In addition to maintaining the material properties important to the use in the fabrication of electronic structures, optical transmission is also desired as it is envisioned that the in fiber structures could be integrated into an optical fiber network.

The p-type fibers were assumed to be poly-crystalline due to the high cooling rate of the fibers during fabrication and the results from the EBSD done on the n-type fibers. This is born out in the EBSD shown in Figure 4.13(b) with the presence of 5 large grains in an area of approximately 0.1 mm^2. Figure 4.13(a) shows that one grain will exist over the whole region of the core or be the dominant one when viewed perpendicular to the fiber axis. Only short sections of fibers were analyzed using EBSD, so there is incomplete information as to how the preform or fabrication parameters influence the crystallization kinetics and the grain formation.

Fabrication of the p-type fiber was the next step in understanding the ability to fabricate in-fiber opto-electronic structure. Depending on the structure that is needed for an application, either an n-type base or a p-type base may be needed. Additionally, the opposing fiber types may be joined to create a superstructure based on each base materials fabrication properties. Characterization of these preliminary fibers indicates that the fabrication of the p-type fiber is feasible. The core structure has low oxygen content and a poly-crystalline core. Long lengths of the fiber were made comparable to the 50-60 cm lengths seen with the n-type fibers. Of concern in the p-type fibers is what appears to be the greater extent of partitioning of the boron in the fiber core. Further experimentation is necessary to understand how the fabrication parameters affect the boron concentration in the core.

4.4 N-type GaSb Fiber

A section of fiber used for SEM analysis of core/cladding is shown in Figure 4.15 where the core is the lighter grey color at the center of the fiber. In the SEM image the core/cladding boundary is seen as mostly circular with lobes of the core protruding into the cladding region.

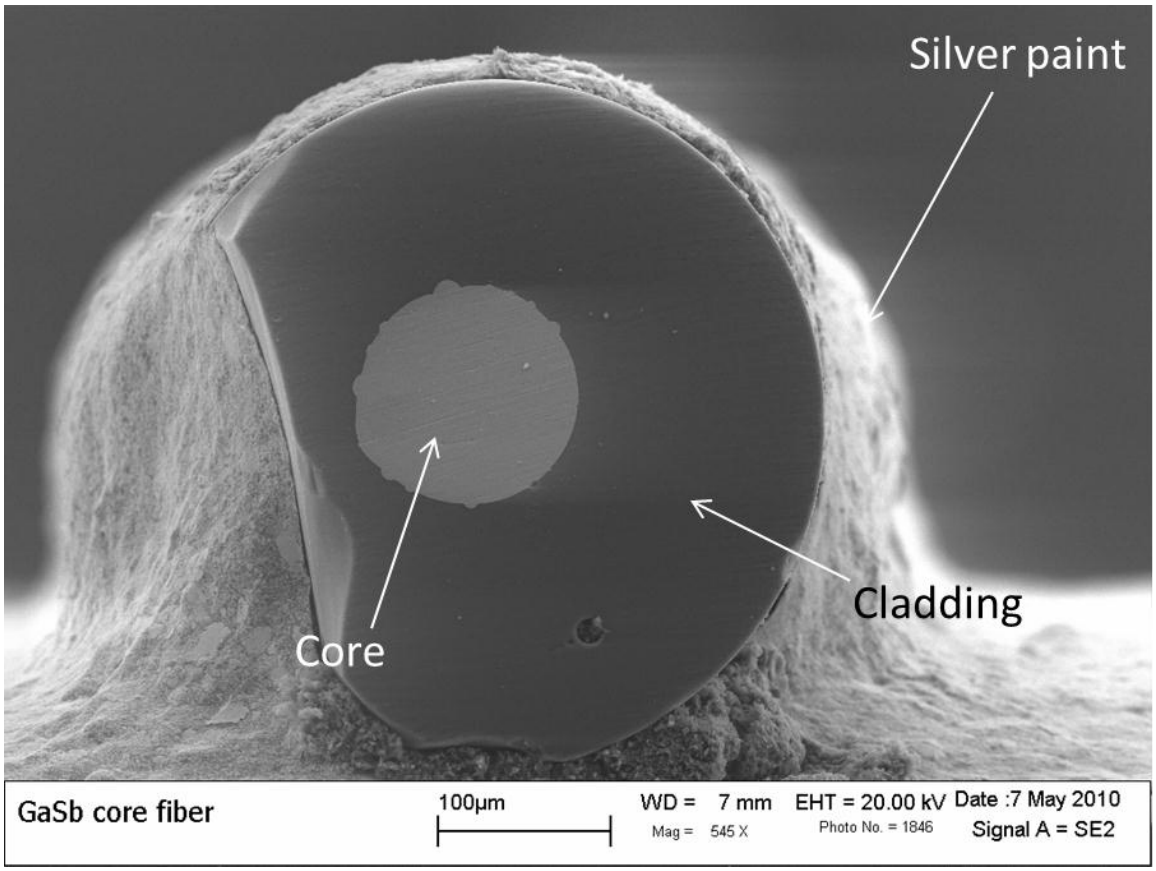

Figure 4.15 SEM micrograph of GaSb fiber end face fracture surface

An EDS point scan of this same sample is shown in Figure 4.16 (a) and (b). Part (a) of the figure is the composition of the different points scanned along the core with the origin marking the core-cladding boundary. Part (b) is a section of the SEM image showing the location of the scanned points on the fiber end face. The SEM micrograph is lined up so that the points on the micrograph match the points on the graph. EDS measurement indicates the presence of the gallium, antinomy, oxygen, sodium, silicon and aluminum in the core. Most of the components of the glass composition from the cladding region have a low concentration in the core region with the exception of oxygen. The compositional levels are roughly constant across the core.

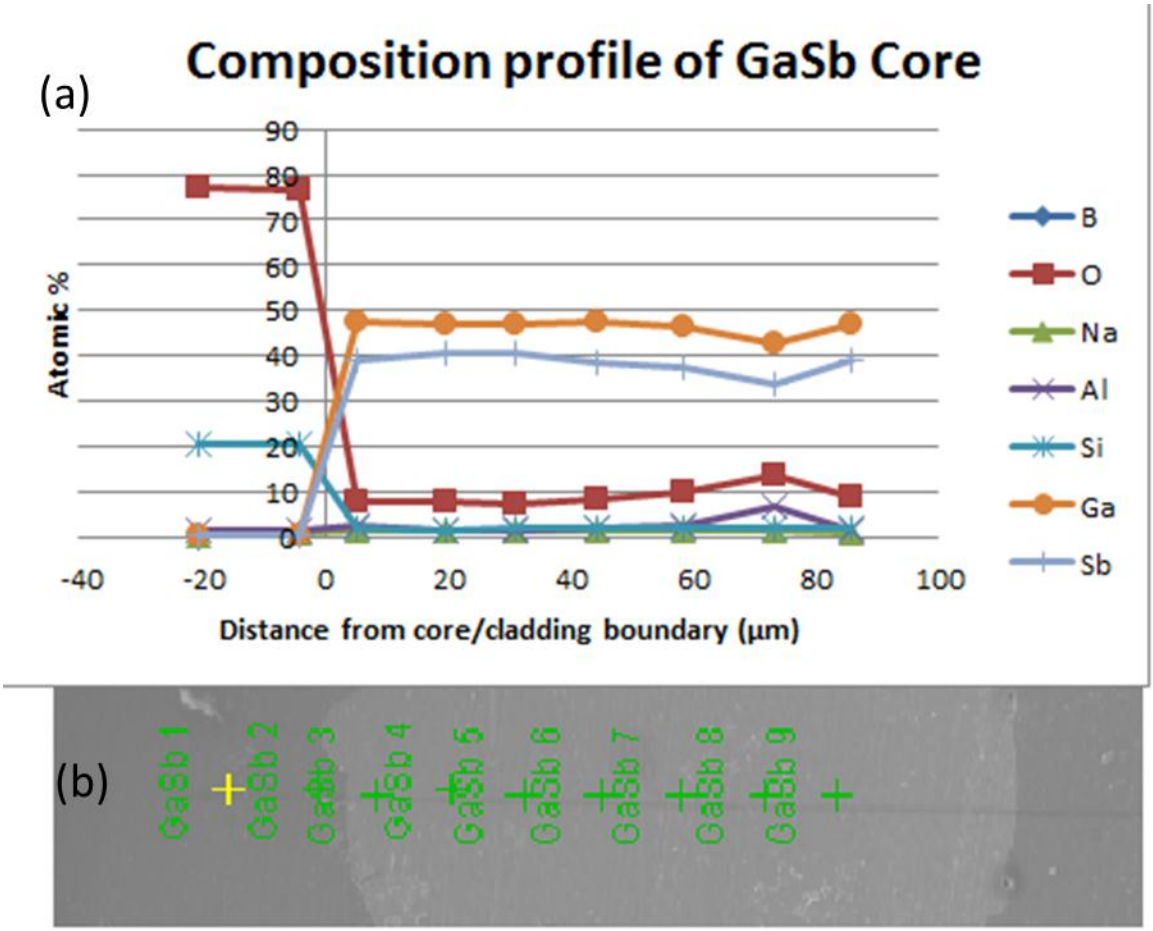

Figure 4.16 EDS of GaSb fiber end face (a) composition by point (b) location of points on end face

Figure 4.17 is an optical micrograph of the fiber when polished along the fiber axis for EBSD characterization. The grain structure can be seen in the micrograph as the changes in the way the light is reflected off of the core region. Regions of similar reflectivity and color are unique grains within the core. Inset into Figure 4.17 is the EBSD scan of a portion of the core along with an inverse pole figure showing the grain orientations. The same grain structure can be seen in both the optical micrograph and the EBSD image. EBSD confirmed the grain size and provided crystallographic data as detailed in the inset

in Figure 4.17 with a section along the core being analyzed. Grain size is shown along with orientation of each grain within the scanned region. The core consists of several grains with an average diameter spanning the width of the core and an average length of approximately 300 µm. Grains consist of several different crystallographic orientations between the {001} and {111} planes normal to the fiber axis.

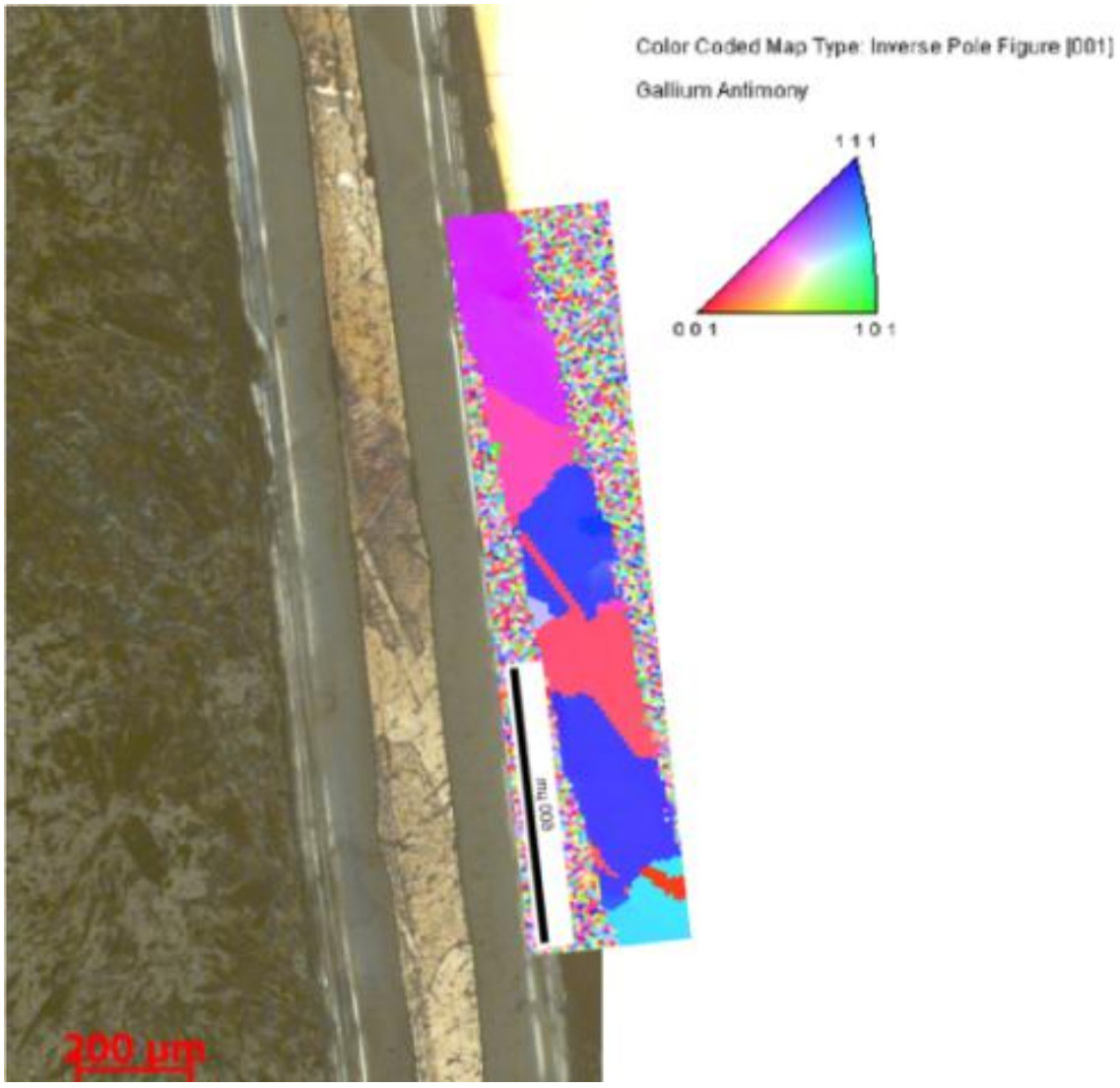

Figure 4.17 Optical micrograph of side polished GaSb fiber with EBSD inset

A fiber section was optically tested but no transmission was detected. This is most likely due to the low external transmittance of the material of ~35% in conjunction with the multiple grain boundaries present in the fiber core. These grain boundaries can act as segregation centers for materials that have diffused into the core and thus will act as scattering centers further reducing the transmission. In this regard, working toward fewer grain boundaries with less diffusion of impurities into the core may allow for a higher transmission to be achieved.

The characterization results of the fiber shows a core that has a GaSb composition with approximately 8% oxidation of the GaSb region. Since the fiber end face was wet polished prior to the EDS analysis, the significant degree of oxidation of the core is probably due in part to the oxidation of the GaSb during the wet polishing. Tighter control of the fabrication process by decreasing the heating and pulling times to reduce oxygen diffusion from and through the cladding and a higher vacuum on the preform to remove the ambient environment prior to heating of the preform will further reduce the detectable amount of oxygen. The presence of other glass constituents in the core region show either minor diffusion into the core or possible contamination during the polishing of the fiber end face. Atomic percent of these other constituents is around 2% or less and could be attributed to either process. At present these contamination levels are too high for efficient device fabrication, so further investigation into the fabrication parameters is necessary to find the cause of contamination in order to reduce these levels. The core region has a high degree of integrity as is seen by the fibers in Figure 4.15-Figure 4.17. The images show the fiber with a continuous core throughout the entire length with no

cracking or other apparent discontinuities. This is most likely due to the close approximation of the glass softening point and the melting point of the GaSb. As the GaSb solidifies, the glass is still fluid enough to accommodate the expansion and relieve any induced stresses due to the solidification process. Stresses related to the differential CTE between the GaSb and the glass cladding are still relevant and can be minimized by controlling the annealing of the fibers, in addition to a reduction in the core size. In Figure 4.15, the core region can be seen as having formed lobes or protrusions into the cladding region which may contribute significantly to the lack of optical transmission. This is also most likely due to the softening point of the glass being close to the melting point of the GaSb. As the core freezes the glass viscosity is too low to resist the growth of the crystal into the cladding region. Alteration of the glass composition to increase the softening point may prevent the development of these "lobes" from forming by increasing the glass viscosity at the freezing point of GaSb. While increasing the softening point of the clad glass will increase the tendency to create voids and cracks, a small increase in softening point should be suitable to decrease the irregularity of core clad interface while not significantly increasing the formation of voids and cracks. The presence of grain boundaries is an important matter as these boundaries influence electronic device performance by altering the band gap near the boundary from that in the rest of the grain. Depending on the size of the grains, annealing may be necessary to minimize the presence of grain boundaries to improve device performance. Crystal orientation can also be important in the fabrication of the devices as the electrical properties can be different depending on the crystal orientation. Epitaxial growth of other materials onto the core will also be affected by the crystal orientation. The grain structure

in the core, seen in both the optical micrograph and in the EBSD image gives an indication of the crystallization of the GaSb. In both images, the intrusion of one grain into another adjacent grain is visible. With the imaged surface being in the interior of the core and that the same crystal orientation is present on both sides of the intrusion, it can be inferred that the intrusion, is completely surrounded by the other grain. With this being the case, the likely explanation is that the surrounded grain grew into that region as the other grain was nucleating and growing in from the cladding/core boundary.

Crystallization of the semi-conductor material is governed by nucleation theory which will be highly influenced by the heat transfer from the core. This is expected to proceed from the outer boundary into the interior and that the nucleation of grains will begin at the glass/GaSb interface and proceed inward toward the center. During the pulling of the fiber, the amount of heat loss from the core will be greatest at the first portion of the fiber being removed from the heat zone and decrease along the fiber opposite the pulling direction. From this, one would expect that the grains will form and grow along the fiber axis until they impinge on another grain that began growing at a later time. This impingement will result in a grain boundary with the lowest energy plane facet growing the fastest, resulting in an angled boundary. While the grain and crystallinity data was collected over a small sample size, there appears that a preferential grain orientation formed in this sample. Analysis of several other samples would be needed to confirm this grain orientation, but this may not be important optically, since GaSb is cubic and hence isotropic. However, it is important for the fabrication of devices and a preferential grain orientation would be advantageous in producing higher quality devices.

Once the fabrication of the silicon and both of the doped silicon optical fibers were completed and characterized, the next step was to develop a 3-5 semi-conductor optical fiber. This material was chosen as they are widely used for LEDs due to the direct band gap structure that they possess, as opposed to the indirect band gap structure of silicon. The difficulty in fabrication of a 3-5 is the lower melting point of the materials. A lower melting point necessitates the use of a glass composition other than pure silica in order to have a softening point compatible with the materials melting point. Addition of other components to the glass adds the possibility of contamination of the core material which appears to be the case in these experimental fibers. While there have been other fibers made from 3-5 materials, this work was the first with this material and in an intermediate temperature range between InSb and silicon optical fibers. The other 3-5 semi-conductor fiber was made with an InSb material for the core using a phosphate glass for the cladding. InSb melts at 527 °C and the softening point of the glass was below the drawing temperature of 700 °C. GaSb core optical fibers were pulled at temperatures estimated to be around 1000 °C based on the glass type.

4.5 Grain Structure Fabrication Dependence Experiment

4.5.1 Data analysis

The data that was collected from imaging the fiber cores using EBSD was processed using the software linked to the FEI Helios electron backscatter application. The output of this data was taken in the form of inverse pole figures (IPF) which the crystal direction is displayed in both the sample normal and fiber axis directions. In addition to the IPF a grain map was also produced. The grain map was utilized to derive the data on grain

sizes that were present in each fiber segment. Areas in the grain maps that denote different grain regions are based on a 2 degree misorientation angle between neighboring regions and are displayed as different colored regions. These images were analyzed and further data was collected using the image processing software Image J. While a particular image was opened in Image J the grain regions were selected using an auto select feature that outlines the region selected. This selected region was then measured for area, perimeter, and a bounding rectangle that gives the length and width of the grain. During selection the grains were identified as one of 4 types. The 4 types are major (grains that span from cladding region to cladding region and occupy greater than 5% of the area viewed or any grain that has greater than 10% of the area viewed), minor (grains that have from 1-10% of the viewed area and at least 1 surface exposed to the cladding), edge (grains that occupy space only along the edge of the core with less than 1 % of the viewed area), and interior (grains which are entirely contained within the core region). These measurements were further modified since each fiber segment has different core dimension. This modification of the data was done to normalize the measurements so as to compare across the samples. Normalization was done for the area, perimeter, and width of the grains with results in these measurements being expressed as a percentage or fraction. The modification for the area is as in Equation 20, Equation 21 is the normalization for the perimeter and the normalized width is described Equation 22.

$$normalized\ area = \frac{area\ of\ grain}{total\ area\ viewed} \tag{20}$$

$$normalized\ perimeter = \frac{perimeter\ of\ grain}{minimum\ perimeter\ of\ area\ viewed} \tag{21}$$

$$normalized\ width = \frac{width\ of\ grain}{width\ of\ area\ viewed} \quad (22)$$

Since the grain shapes can be varied and multiple grains occupy the same linear distance of the core, the grain length was modified to account for this structure. The grain length was multiplied by the normalized area to create an adjusted grain length. This adjustment of the length represents the length of that grain if it occupied 100 percent of the core diameter. The method used is shown in Equation 23 where the measured length is the length of the viewed area.

$$adjusted\ length = normalized\ area\ \times measured\ length \quad (23)$$

The normalized and adjusted data was taken for each of the grains and totaled and then used to compute the averages of the grain length & percent area of the core that the grain type occupies. Some of the samples had a skewed distribution where several small major grains existed and one very long grain that took up the majority of the core. This data was taken and then a weighted average and weighted standard deviation was calculated in order to more accurately describe the type of grain length one would likely find. The weighting factor was accomplished by calculating the length fraction that the grain had over the entire length of the sample. This is illustrated in Equation 24.

$$w_i = \frac{adjusted\ length}{total\ length\ viewed} \quad (24)$$

The sample quality is important in the getting accurate and high resolution data during EBSD analysis. Surface quality is extremely important and when the surface isn't flat or if the surface is distorted due to residual strain, the ability to get crystal data is impeded. This impediment results in not being able to index some areas and they show up as an amorphous or non-indexed area. During analysis of the grain maps, the images were altered to fill in some of the amorphous areas in order to smooth the edges so that Image J would correctly calculate the area or perimeter of the areas selected. Smoothing of the edges or filling in of areas was done by connecting the adjacent areas with the same colors and filling in. If the gap was between two different grain areas, the non-index area was split between the 2 grains. Decisions on filling in vacant areas were made by comparing the EBSD grain maps and EBSD inverse pole figure (IPF) maps that show the crystal orientation. When the vacant area was separated by regions that had the same orientation, that area was assigned to the major grain. If the gap was large enough that the OIM program assigned the grains separated by a vacant area as different grains, then the grains were merged if the IPF map showed the same orientation in both regions. The majority of the image alteration was due to the smoothing of the edge along the core/cladding boundary which in the un-smoothed images showed up as a saw tooth type profile along this boundary. Alteration of the grain maps did not significantly change the shape or area of the grain.

4.5.2 Selected fibers

Fibers that were drawn in the experiment were initially sorted by outside diameter using a micrometer. The fibers were then imaged using an optical microscope. Digital images of

the fiber end face were taken. The outside and inside core diameters were then measured using the camera software from these images. Some of the measured fiber end face images are shown in Figure 4.18-Figure 4.20. The reflected light optical micrographs show representative samples out of the total sample pool. In all of the micrographs, the core can be identified by the bright circular region near the center. Figure 4.18 is the optical micrograph of sample 6-1. The micrograph shows a circular core with a diameter of approximately 290 µm as detailed by the measurement bracket around the core.

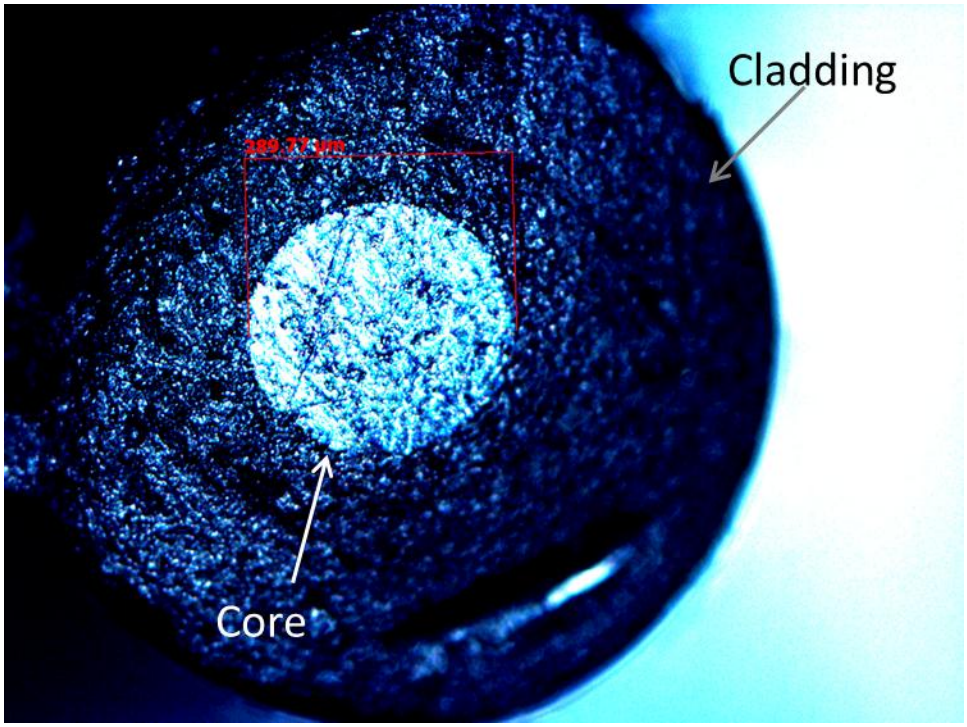

Figure 4.18 Optical Micrograph of Sample 6-1 showing measured end face

The micrograph of sample 6-1 shows a distinct boundary between the cladding region and the core. In the micrograph the circularity of the core is visible and indicates that the core solidifies after the cladding region has achieve sufficient viscosity to resist the growth of the crystal from displacing a portion of the cladding. Figure 4.19 is the end

face of sample 23 at 20x objective magnification. The core is visible as the bright circular region with a diameter of approximately 99 µm.

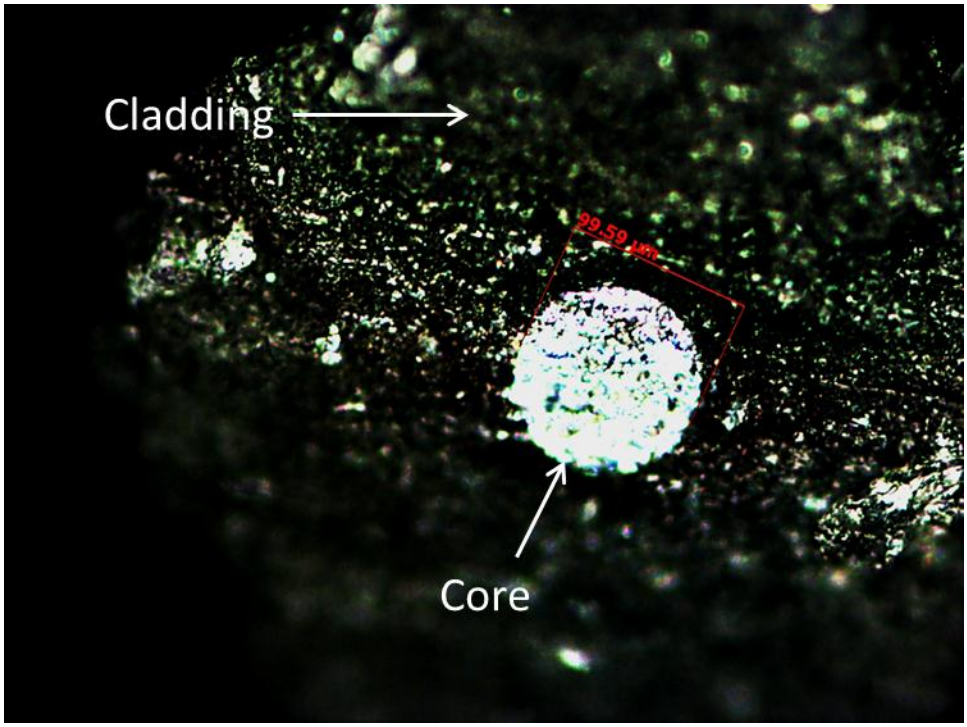

Figure 4.19 Optical Micrograph of Sample 23 showing measured end face

The optical micrograph of Sample 23 is similar to one for sample 6-1, in that the core is visible as a circular region with a distinct core-cladding boundary. Visibility of the core is slightly obscured by the end of the fiber be slightly out of focus. The out of focus portion is due to the rough polishing of the fiber and the mounting not being perpendicular to the microscope lens. Sample 32-1 is the fiber sample with the smallest core diameter and is shown in Figure 4.20. The core region is visible as a mostly circular region in the center at an objective magnification of 20x. The core diameter is measured to be between approximately 40-43 µm. Deviation from a circular cross section is most likely due to slightly uneven heating of the preform during the fiber pulling process.

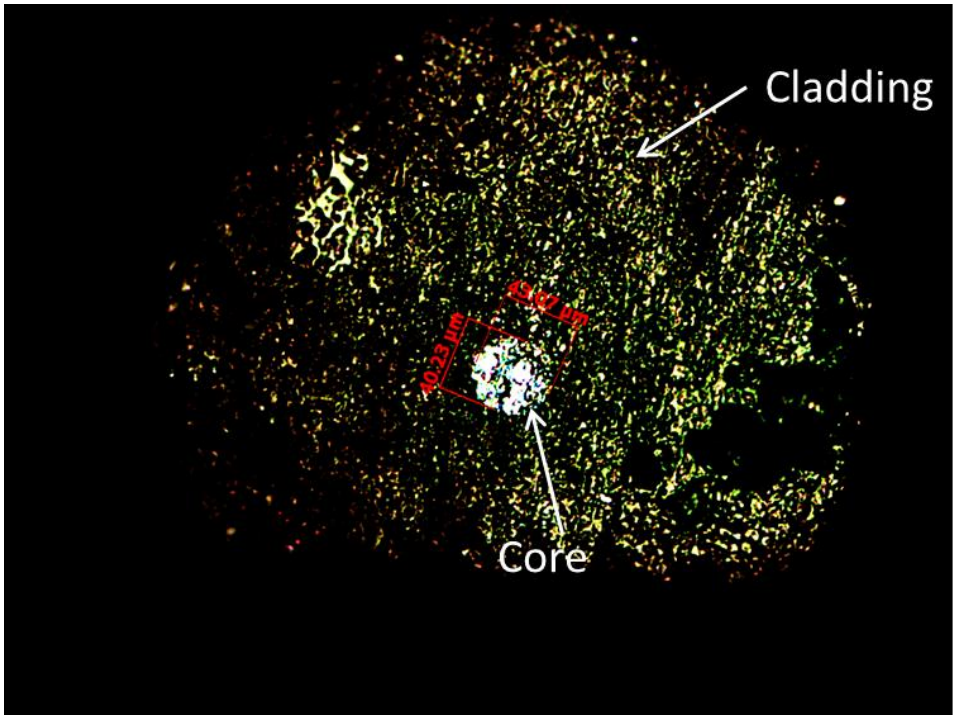

Figure 4.20 Optical micrograph of sample 32-1 showing measured end face

Overall, 54 samples were selected from the first round of sorting done solely by inside diameter so as not to introduce bias. All of the samples were mounted and polished in preparation for EBSD with 44 samples remaining at the end of the final polishing step. Figure 4.21-Figure 4.23 are the polished samples that are shown in Figure 4.18-Figure 4.20. Figure 4.21 shows the side polished view of sample 6-1 after polishing for EBSD analysis which shows a core diameter of 290 μm in the micrograph.

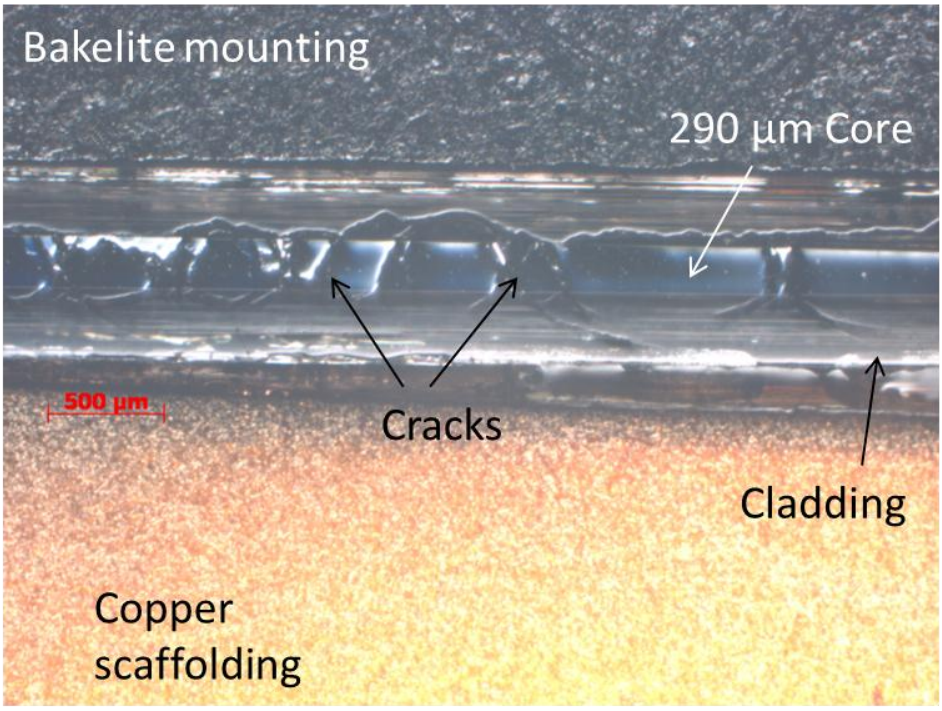

Figure 4.21 Sample 6-1 polished for EBSD

The fiber sample shown in Figure 4.21 has many cracks in the core. Some of the cracks may come for the release of stress contained in the core as the cladding layer is polished away, but several were visible prior to the beginning of polishing. Cracks can be seen to occur at close intervals in the core with approximately 100 µm to 1 mm between cracks. Cracks are also visible propagating out into the cladding region which is an indication the fiber is in a high stress state at some point in the fabrication process. The cracks in the core are mainly perpendicular to the core axis and the cracks in the cladding run roughly parallel to the fiber axis. These crack patterns suggest that the crack may start in the cladding due to the stress in the radial direction brought about by the expansion of the silicon. The cracks then propagate through the silicon and continue on the other side as the stress is relieved. Figure 4.22 is a micrograph of sample 23 which has an average core diameter of 97 µm.

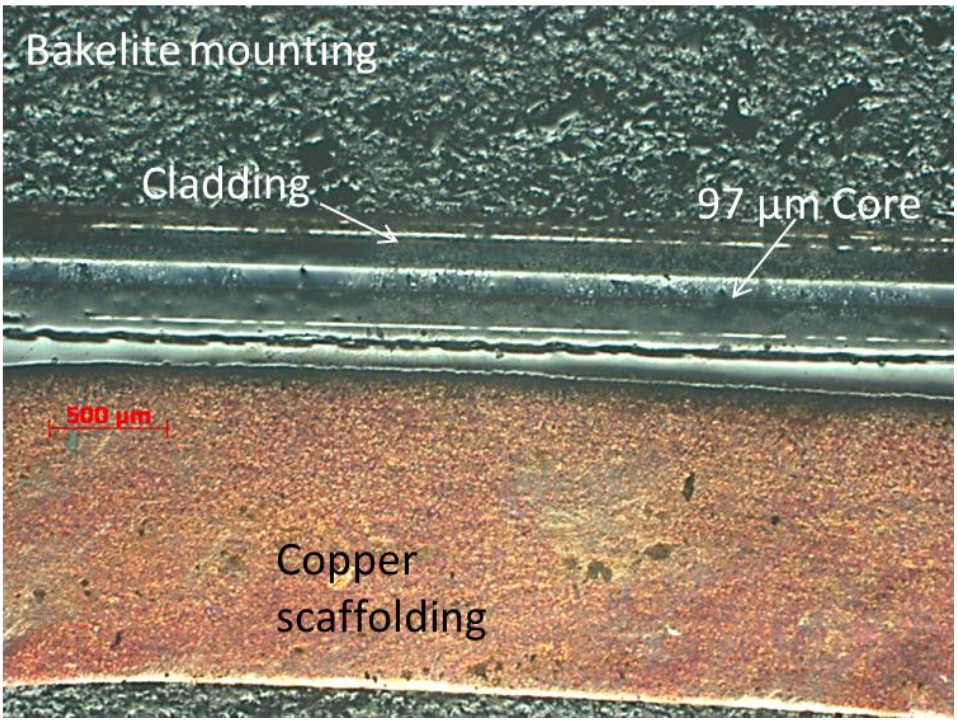

Figure 4.22 Sample 23 polished for EBSD

The polished section of the sample doesn't show any visible cracks in the core. A lack of cracks in the core or cladding shows that the stress state generated during the fabrication is below the critical value necessary to generate and propagate cracks such as those in sample 6-1. Figure 4.23 shows a micrograph of sample 32-1, which was the fiber that had the smallest core diameter of the samples tested. The fiber integrity of Sample 32-1 is similar to sample 23 with the lack of cracks in the core and cladding region evident. The frequency of cracks increased with the increase in the core diameter of the fiber for the large diameter fibers and did not exist at all in the small diameter fibers.

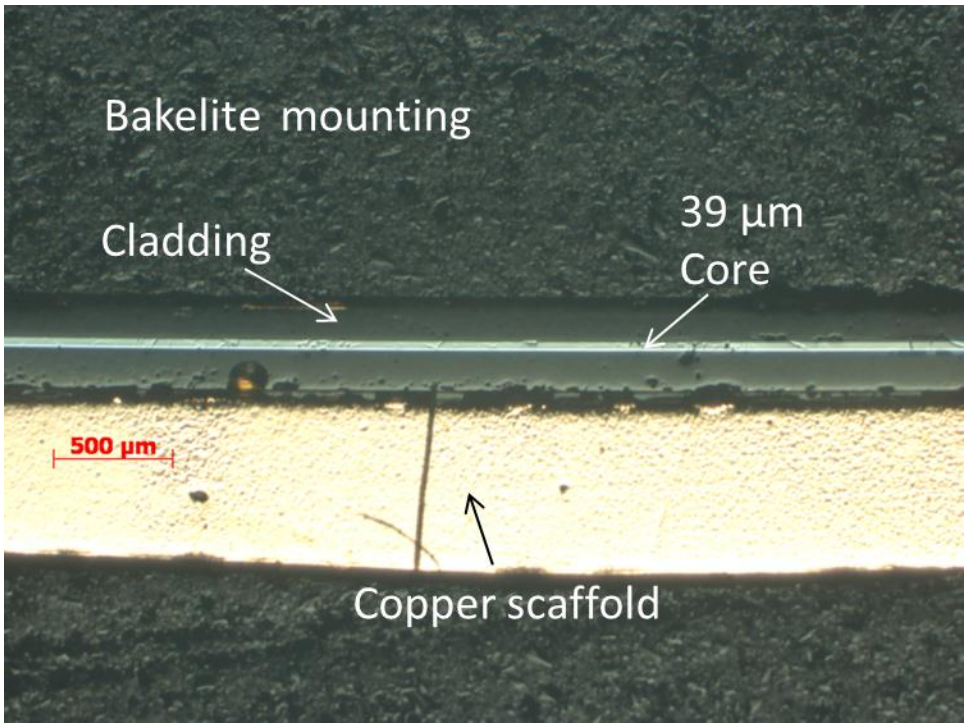

Figure 4.23 Sample 32-1 polished for EBSD

Of the 44 samples that were mounted and polished, 12 samples were characterized by EBSD. The samples that were characterized are detailed in Table 4.1 with the trial origin and pulling conditions along with the resultant physical dimensions and the length of the sample that was scanned. The trial number corresponds to a specific set of fabrication conditions along with a specific preform. Only one fiber was produced during one trial run with fiber lengths depending on the fabrication parameters. The pulling speed refers to the rate at which the tailstock moves and draws a fiber from the end of the preform. Feed speed refers to the rate at which the torch was moved along the preform to prepare the successive preform section for having fiber drawn. Outside diameter (OD) and inside diameter (ID) are the average of the diameters of the fiber section as measured by optical microscopy. Wall thickness is the difference between the OD and the ID. Preform ratio is the ratio between the OD and ID of the preform. Fiber ratio is the ratio between the OD

and ID of the fiber that was pulled from its preform. Length viewed is the length of the sample that was imaged by EBSD.

Table 4.1 Measured samples characterized by EBSD

Sample	Trial	pulling speed (m/min)	feed speed (mm/min)	OD (µm)	ID (µm)	wall thick (µm)	Preform ratio	Fiber OD/ID ratio	length viewed (µm)
32-1	14	3500	25	408	39	184	0.200	0.095	10677
30-1	34	4000	25	555	41	257	0.133	0.074	1907
32-3	14	3500	25	450	47	201	0.200	0.104	3866
26	14	3500	25	529	57	236	0.200	0.107	3502
22-1	14	3500	25	576	67	254	0.200	0.117	5692
23	15	4000	25	550	97	226	0.200	0.177	7513
15-2	15	4000	25	633	112	260	0.200	0.178	4328
24-2	16	4500	25	590	130	230	0.200	0.220	1498
16	16	4500	25	667	142	263	0.200	0.212	3575
17-1	20	3000	35	618	178	220	0.200	0.289	5726
2-1	32	4500	30	1241	210	515	0.200	0.169	4863
6-1	20	3000	35	816	290	263	0.300	0.355	7816

4.5.3 Electron Backscatter Diffraction

The data utilized in determining the grain lengths was taken from the unique grain maps that were produced by the EBSD software (OIM) linked to the hardware installed on the FEI Helios. The color in each image indicates a grain based on a grain crystal orientation mismatch of 2° between regions. It was necessary to scan several regions for each fiber sample in order to determine the lengths of the grains as many grains were longer than the scanned area. These images are put into individual montages for each fiber sample and are shown in Figure 4.24-Figure 4.35 and are shown in order from smallest core

diameter to largest. Colors are assigned by the program and change from scanned section to section. The fiber sections start in the upper left corner and proceed from left to right. There is overlap in several of the fiber segments and during analysis of the grain lengths, the images were lined up to eliminate duplication of area or over estimation of grain length. In Figure 4.24 the upper left 2 images in the montage show several grains followed by a longer grain. This grain continues through the rest of the images until the last one in the lower left corner of the montage. The continuity of the grain is supported by the crystal orientation maps that are shown in Figure 4.37. The scale among the images is different so that comparing the montage images is not useful. Scale of the images is derived by the conditions during the scan which sometimes required a smaller scan area of the core in order to minimize charging of the surrounding area from affecting the scan.

Figure 4.24 Sample 32-1 EBSD grain map montage

Sample 30-1 in Figure 4.25 is 2 scanned sections that are not connected as opposed to the other images where the scans are of successive sections. The section on the left side is composed of two grains filling up the entire region while the right section has multiple grains.

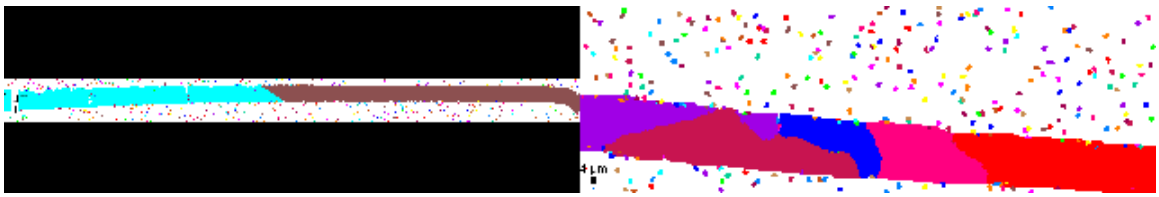

Figure 4.25 Sample 30-1 EBSD grain montage

Sample 32-3 is shown in Figure 4.26 where there are 2 major grains visible with the lining up of the sections. The first major grain starts in the upper left section and continues into the upper middle section. The second major grain starts in the end of the upper middle section and continues through the rest and ends at the end of the lower middle section.

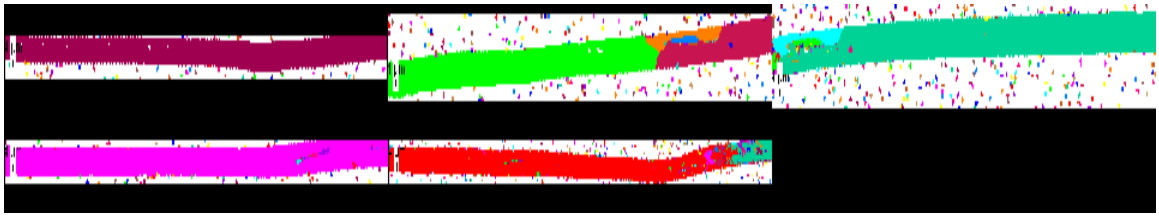

Figure 4.26 Sample 32-3 EBSD grain map montage

Figure 4.27 is the montage for sample 26 where many grains of varying sizes are visible in the first 3 sections followed by the beginning of a longer grain. The majority of the grain shapes are roughly rectangular indicating a non-faceted growth.

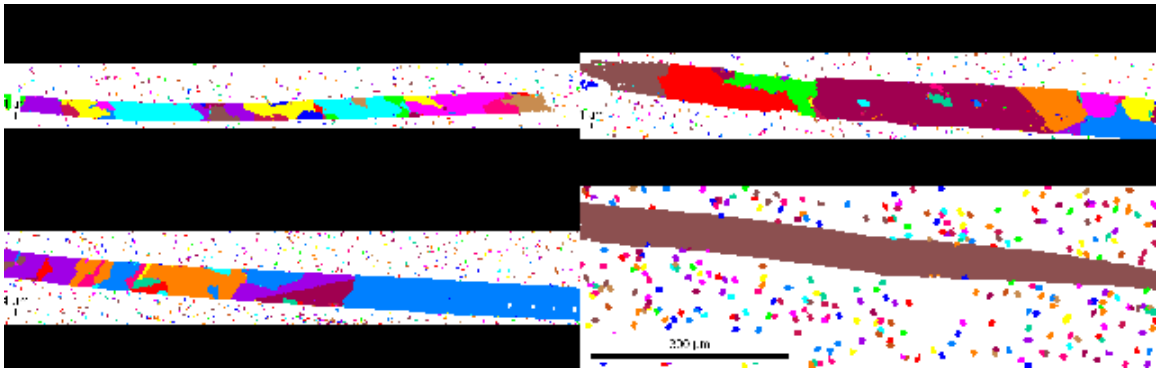

Figure 4.27 Sample 26 EBSD grain map montage

Sample 22-1 is shown in Figure 4.28 that has a variety of grain sizes like sample 26. The grain shapes in the images are both rectangular as well as angled at the boundary between grains which suggest a faceted grain crystallization mechanism.

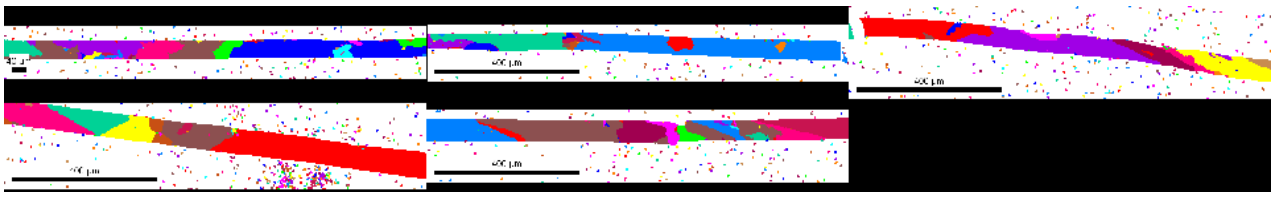

Figure 4.28 Sample 22-1 EBSD grain map montage

Figure 4.29 is the grain montage for sample 23 where 5 major grains are visible. The first grain starts in the upper left section and continues to the upper right where the second and beginning of the third major grain starts. The angle boundaries between all of the grains are visible in the image and indicate faceted crystallization.

Figure 4.29 Sample 23 EBSD grain map montage

Sample 15-2 is shown in Figure 4.30 with 3 major grains visible and angled boundaries between them and a few large minor grains. The grains present in the maps show few grains intruding into the longer major grains.

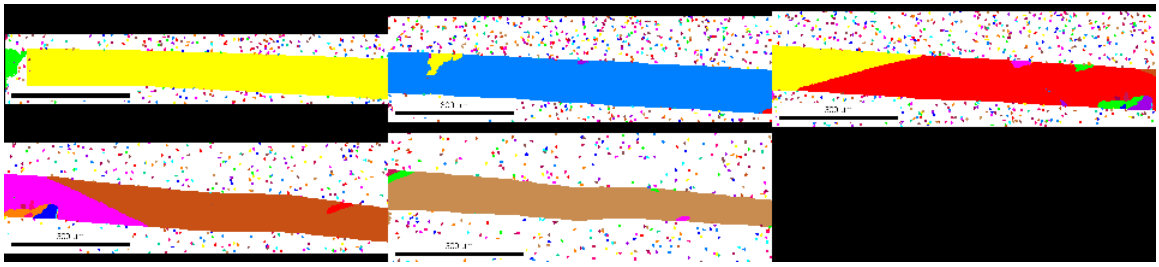

Figure 4.30 Sample 15-2 EBSD grain map montage

Figure 4.31 is a 4 section montage of sample 24-2 that shows 6 major grains and 3 large minor grains. Sample 24-2 also displays the angled boundaries of a faceted growth mechanism.

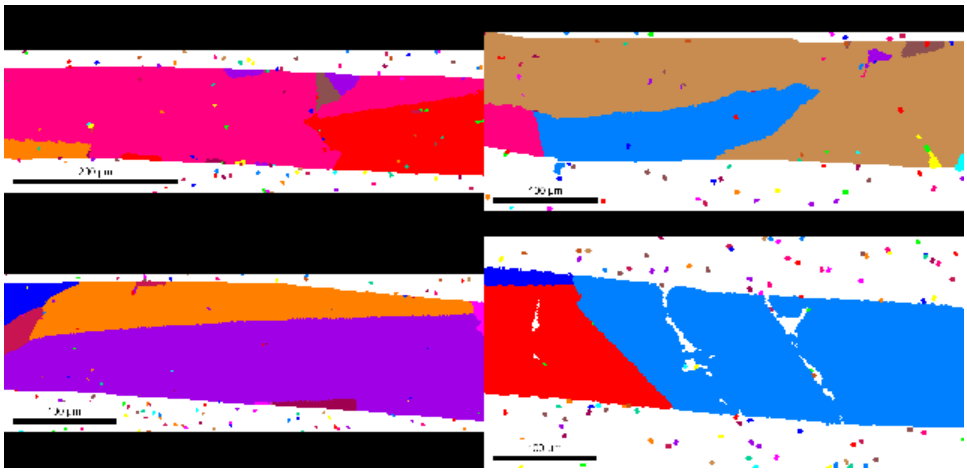

Figure 4.31 Sample 24-1 EBSD grain map montage

The grain maps for sample 16 are shown in Figure 4.32 where 4 major grains are identifiable from the 3 grain map sections. Overlap in all 3 sections is identified by the common features of the interior grains. Tapering of the grain on the section on the right side of the montage is due to polishing of the fiber on an angle. The point of the taper is where the core intersects the cladding at the interface between the two.

Figure 4.32 Sample 16 EBSD grain map montage

Figure 4.33 contains 4 grain map sections of sample 17-1. In the grain map montage 5 major grains are visible. The tapering of the grains on the bottom sections is similar to sample 16 where the fiber was polished on an angle relative to the fiber axis.

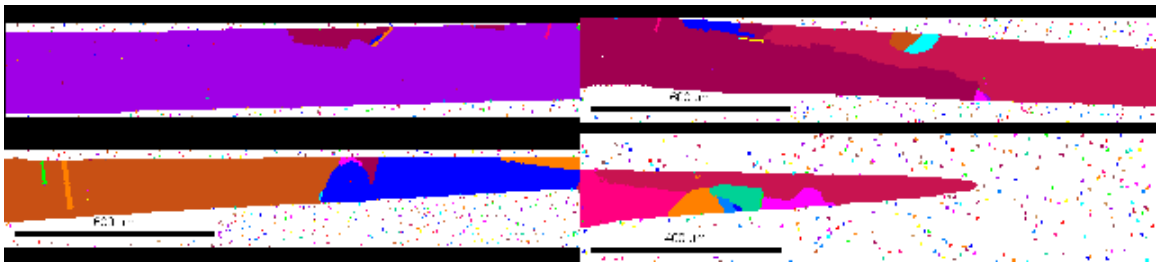

Figure 4.33 Sample 17-1 EBSD grain map montage

Five EBSD grain maps for sample 2-1 are presented in Figure 4.34. In the 5 grain maps there are 4 unique grains identifiable. The major grains are mostly free from other grains with exception of some grains along the edge and one larger minor grain in between 2 grains in the 3rd section from the left.

Figure 4.34 Sample 2-1 EBSD grain map montage

Figure 4.35 shows 9 series of grain maps for sample 6-1, which is the largest core diameter fiber analyzed. Across the 5 sections only 1 major grain is seen along with the presence of a few minor grains intruding into the major grain.

Figure 4.35 Sample 6-1 EBSD grain map montage

Long grains are identifiable in samples 32-1, 32-3, 23, 2-1 and 6-1 shown in Figure 4.24, Figure 4.26, Figure 4.29, Figure 4.34, and Figure 4.35 respectively. Most of the grain maps were imaged at or near the middle of the core. The grains within the core at these regions typically span across the diameter of the core. Some of the fibers were polished on an angle so that a portion of the core that was imaged was near the core-cladding boundary. Since the grains at the center of the core spanned the diameter it was assumed that the grain would appear to span the diameter in all directions. The sections that show the grain intersecting the cladding were then interpreted as being a grain that was the full diameter of the core and therefore a major grain. Minor and edge grains are typically not that long in comparison to the major grains and would show up as small interior grains in those sections and would not be confused with a major grain.

In addition to the grain maps that were produced by the OIM software, inverse pole figures (IPF) were made. The IPF details the crystal plane in the direction perpendicular to the fiber axis. Other orientations can also be displayed, however one whose normal is parallel to the fiber axis is relevant for on end device fabrication and for that reason it is presented in the results. The inverse pole figures are presented in Figure 4.37 - Figure 4.48 and the color map to interpret the IPFs is shown in Figure 4.36. The IPF images

were used to help interpret the grain maps due to missing portions of the core. When the gap was large enough, the computer software interprets the resumption of the grain as the start of a new grain, while the IPF shows the same orientation on both sides of the gap. When that situation was presented during the analysis it was interpreted that the grain was the same across the gap in the core, and the grain maps were changed accordingly. The IPF presented in these figures does not show any pattern that suggests the formation of a preferential orientation during the solidification process. The IPF maps are color coded to indicate the crystal plane present in the section of fiber. In Figure 4.36 the low index planes are at vertices of the triangle and have the color red to represents the {001} plane, green the {101} plane, and blue the {111} plane. Higher index planes are represented by yellow for the planes near the {012} and {013} as the planes transition from the {001} plane to the {101} plane, light blue for the {112} and {122} planes as they transition from the {101} to the {111}, and purple represents the planes near the {112} to {117} as the planes transition from the {111} plane to the {001} plane.

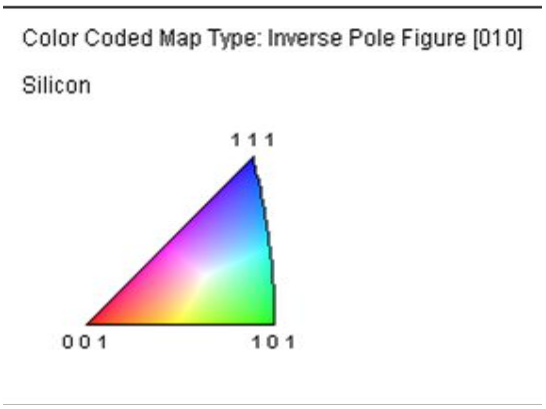

Figure 4.36 Color map for IPF crystal orientation

Figure 4.37 is the IPF maps of the sections scanned for sample 32-1. The major crystal orientation present is near the {111} plane. Some of the less prevalent orientations shown in the upper right corner are near the {001} plane with some {111} planes present in

between. The major {111} plane has a slow rotation of the plane from near {111} to near the {123}.

Figure 4.37 Sample 32-1 IPF montage

The Sample 30-1 IPF map is shown in Figure 4.38 with the presence of {211} and {111} present in about equal amounts. Areas show a slight deviation for the {211} and {111} planes in the section on the right as the grains change from one orientation to another.

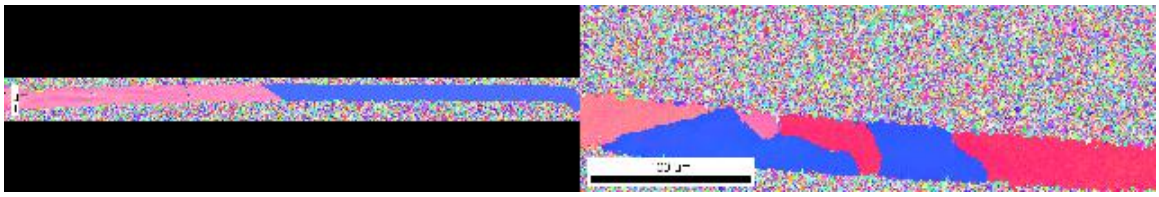

Figure 4.38 Sample 30-1 IPF montage

Figure 4.39 is the IPF map for the sample 32-3 sections. Crystal planes present are the {111} and near the {101} orientations. Not much rotation is seen in the {111} plane before it changes to the {101}. The {101} rotates towards the {212} plane until it encounters a region of {001} plane orientations.

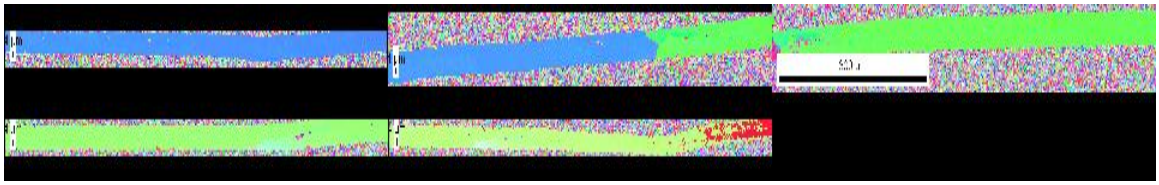

Figure 4.39 Sample 32-3 IPF montage

Figure 4.40 shows the plane orientations of sample 26 where multiple orientations are present in 3 of the 4 sections in the montage. Planes have orientations ranging from {001} to {111} and orientations in between those 2 planes. The major orientation is near the {111} with several regions showing {001} and near {001} orientations.

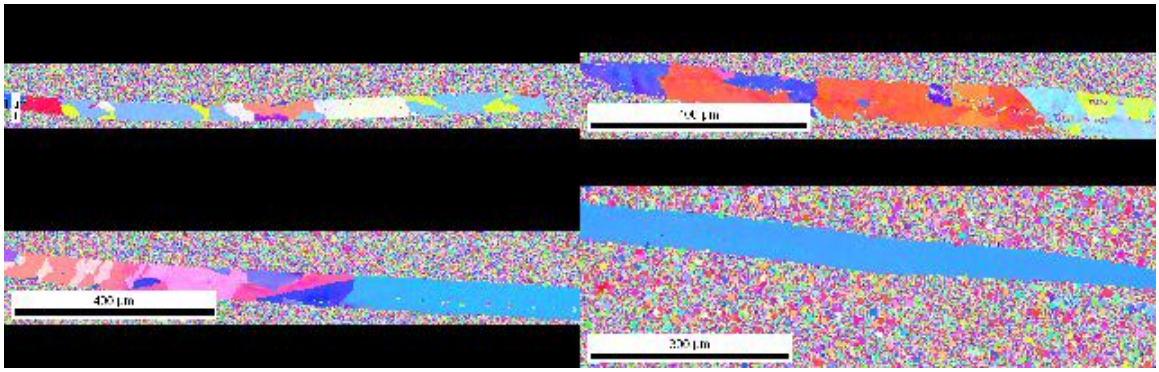

Figure 4.40 Sample 26 IPF montage

The IPF map for sample 22-1 is shown in Figure 4.41 which is similar to the IPF map for sample 26. Most of the grain plane orientations change from between near the {001} plane to {111} plane.

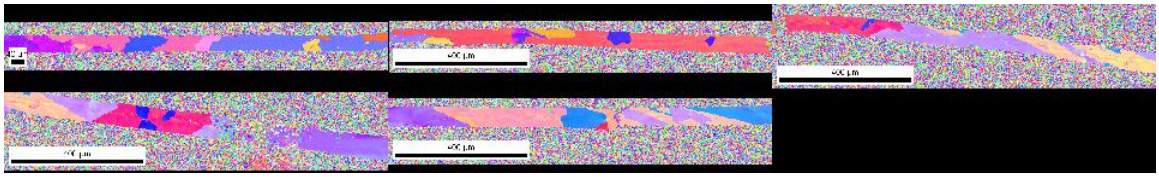

Figure 4.41 Sample 22-1 IPF montage

Figure 4.42 shows the IPF map for the sections of the sample 23. Plane orientations present are planes near the {111}, planes near {123}, and planes near {210}

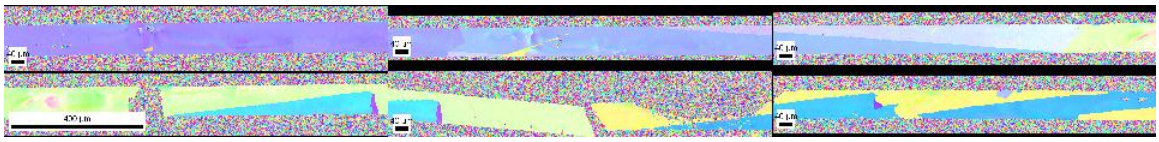

Figure 4.42 Sample 23 IPF montage

Sample 15-2 IPF maps are shown in Figure 4.43 where plane orientations of {210}, {111} and near {112} are visible in the IPF maps section going from left to right.

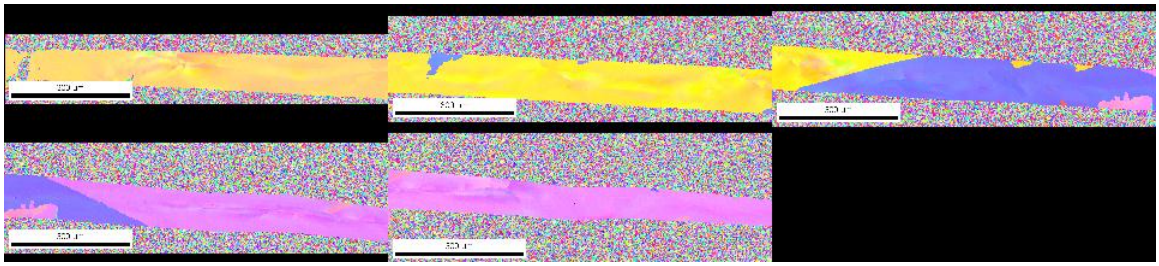

Figure 4.43 Sample 15-2 IPF montage

Figure 4.44 is the IPF maps section of sample 24-2 with plane orientations of {113} and near {101} and near {011} are shown in the sections from left to right.

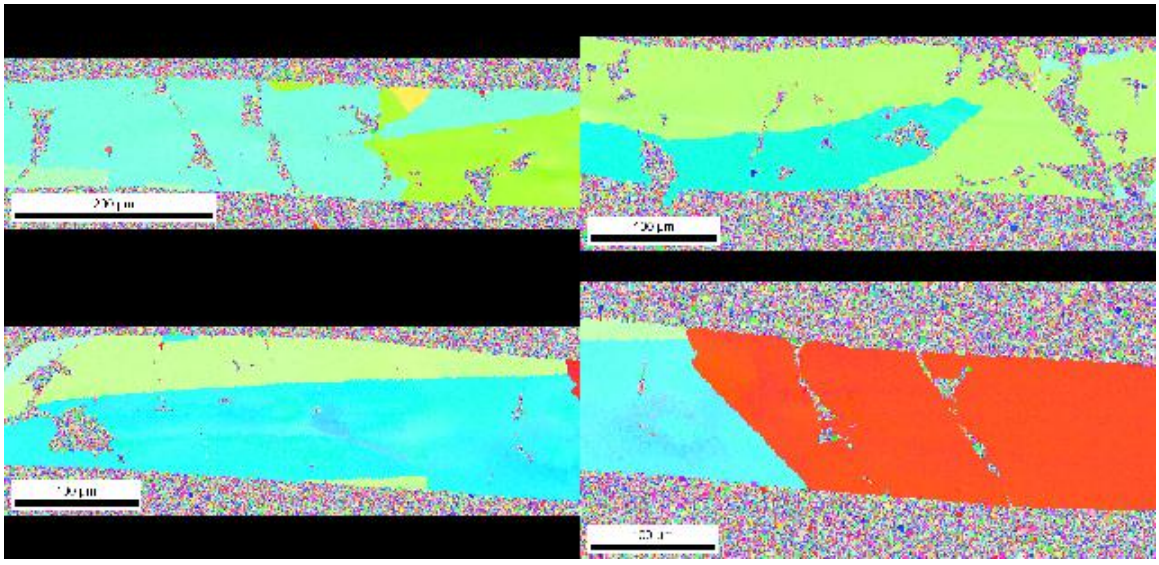

Figure 4.44 Sample 24-2 IPF montage

The IPF maps for sample 16 is shown in Figure 4.45 where the major grains visible have plane orientations of {111}, {210} and near {001} going from the left to the right.

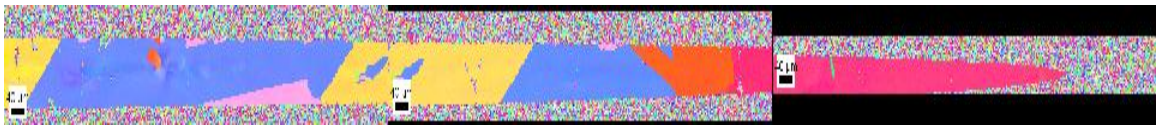

Figure 4.45 Sample 16 IPF montage

Sample 17 IPF maps of the scanned sections are shown in Figure 4.46. The plane orientations visible are mostly near {211} in orientation.

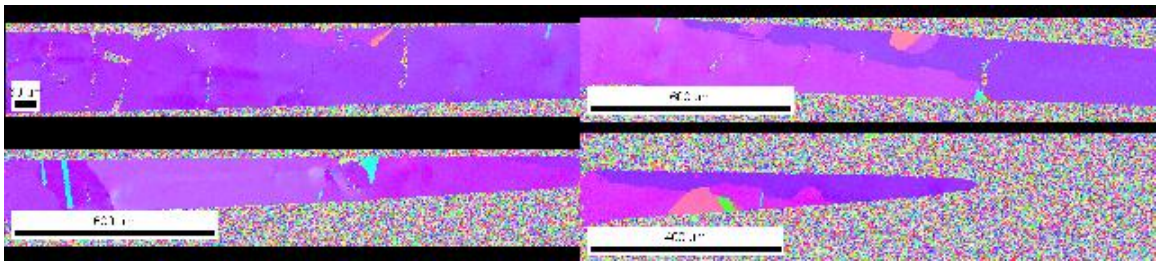

Figure 4.46 Sample 17 IPF montage

Figure 4.47 shows the IPF map for the scanned sections of sample 2-1. The sample has several large areas with one orientation. Starting from left to right the plane orientations are {001}, {111}, near {115} which shows up as the pink and salmon color sections

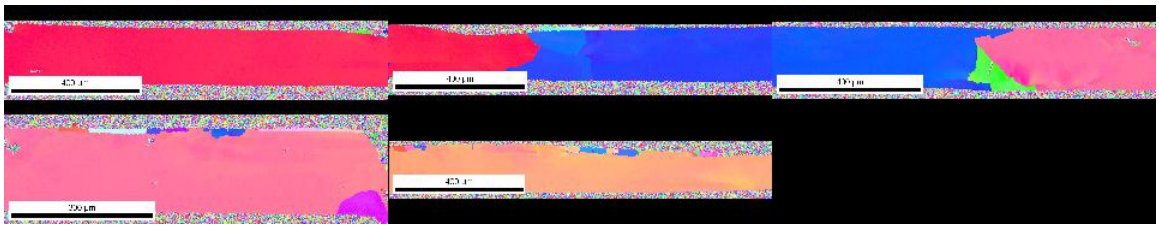

Figure 4.47 Sample 2-1 IPF montage

IPF maps of the scanned sections of sample 6-1 are shown in Figure 4.48. Only one major grain orientation is identified. The plane orientation is the {101} plane and it extends the whole length of the scanned area.

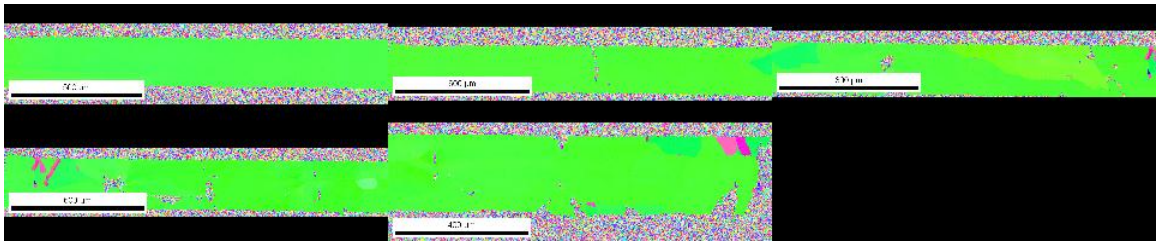

Figure 4.48 Sample 6-1 IPF montage

The IPF maps of the scanned fiber samples do not show a preferred plane orientation across the sample group. Many of the planes present have a low index orientation in line with the optical axis of the fiber. Low index planes are the lowest energy planes and the growth of the planes in typically fastest in the {001} direction followed by the {101} and then {111}.[25] The IPF maps indicate that the process of crystal growth , as far orientation is concerned, is random with growth of mostly low index planes in line with the fiber axis.

4.5.4 EBSD measurement data

The EBSD images were processed to collect grain length data for 4 different grain types, with the emphasis being on major and minor grains. This data was compiled along with the variation (σ) in the grain lengths within a sample. Average grain length was plotted as a function of core diameter with the overall data being separated into subgroups. The subgroups are samples based on the drawing speeds of the fiber samples which comprise 4 groups and samples from the overall pool that have a similar wall thickness which comprised a separate group. Drawing speeds of 3, 3.5, 4 and 4.5 m/min were used in the fabrication of the samples and the draw speed is used to denote the subgroups based on drawing speed. The data collected on the major grains is detailed in Table 4.2. Additional data on the other minor and interior grain types that was collected from the EBSD

analysis is included in Table 4.3. Data presented in Table 4.2 and Table 4.3 gives the inside diameter of the fiber (core diameter), the wall thickness of the cladding from the boundary of the core to the outside diameter, the difference between the preform OD to ID ratio and the fiber OD to ID ratio (Δ ratio), the grain variation, the maximum grain length in the sample, the number of grains identified in the sample and the number of grains per millimeter.

Table 4.2 Major grain data derived from EBSD analysis

Sample	ID (μm)	wall thickness (μm)	Δ ratio	% Area	Avg. Length (μm)	σ	Max length (μm)	grains	grain/mm
32-1	39	184	0.1045	94.5	7898	2761	8903	6	0.56
30-1	41	257	0.0597	97.2	269	331	773	6	4.20
32-3	47	201	0.0962	96.2	1856	457	2196	3	0.78
26	57	236	0.0925	84.5	689	600	1429	18	5.14
22-1	67	254	0.0833	87.1	403	76	787	22	3.87
23	97	226	0.0226	94.2	1412	1259	2695	5	0.67
15-2	112	260	0.0224	96.8	1407	584	1977	3	0.69
24-2	130	230	-0.0200	96.0	235	129	401	6	4.01
16	142	263	-0.0124	94.9	821	391	1325	4	1.12
17-1	178	220	-0.0887	90.0	1329	974	2444	4	0.70
2-1	210	515	0.0308	96.8	1430	292	1686	4	0.82
6-1	290	263	-0.0553	96.2	7530	275	7530	1	0.13

Numerical values of the quantities described are readily understandable except the Δ ratio. The Δ ratio is calculated by subtracting the ratio of the diameters of the fiber from the ratio of the diameters of the preform it was made from. When the value is positive, it means that the fiber ratio is smaller than the preform ratio and when it's negative it means it's larger. The process for the formation a positive Δ ratio is due to the pulling of a

capillary tube of the front of the preform and having the collapse due to the low viscosity of the silica cladding. A negative value is formed by pulling the cladding glass off the external portion of the preform prior to the pulling of the interior into a fiber. This is caused by higher temperatures at the cladding surface than in the interior of the cladding. The lower surface viscosity allows for the outer layer of the cladding to be pulled off prior to movement of the interior portion.

Table 4.3 Minor grain data derived from EBSD analysis

Minor grains				Interior grains					
Sample	ID (μm)	% Area	Avg. Length (μm)	grains	grains/ mm	% area	Avg. length	grains	grains/ mm
32-1	39	1.3	24.6	5	0.47	0.46	1.2	73	6.8
30-1	41	1.2	9.4	1	0.52	0.17	0.2	19	10.0
32-3	47	4.8	71.2	3	0.78	1.65	0.5	88	22.8
26	57	11.6	29.4	19	5.43	1.18	0.7	119	34.0
22-1	67	7.5	30.7	14	2.46	2.65	1.0	67	11.8
23	97	5.1	114.7	4	0.53	0.65	0.4	45	6.0
15-2	112	1.4	15.5	4	0.92	0.70	0.3	65	15.0
24-2	130	4.5	6.7	6	4.01	1.34	0.2	88	58.7
16	142	2.3	85.6	1	0.28	1.01	3.4	56	15.7
17-1	178	9.1	36.8	11	1.92	0.44	2.6	49	8.6
2-1	210	1.3	35.0	2	0.41	0.05	1.4	20	4.1
6-1	290	2.7	9.0	7	0.90	1.60	3.0	62	7.9

Figure 4.49 and Figure 4.50 plot the average major grain length versus the core diameter for pulling speeds of 3 and 3.5 m/min and the 4 and 4.5 m/min respectively. It should be noted that the samples plotted for the 3.5 m/min are also sample sections randomly taken from the same fiber. The points in Figure 4.49 show different trends. Fibers pulled at 3

m/min have an increase in grain length with core diameter, while the fibers pulled at 3.5 m/min show an increase in grain length with a decrease in core diameter.

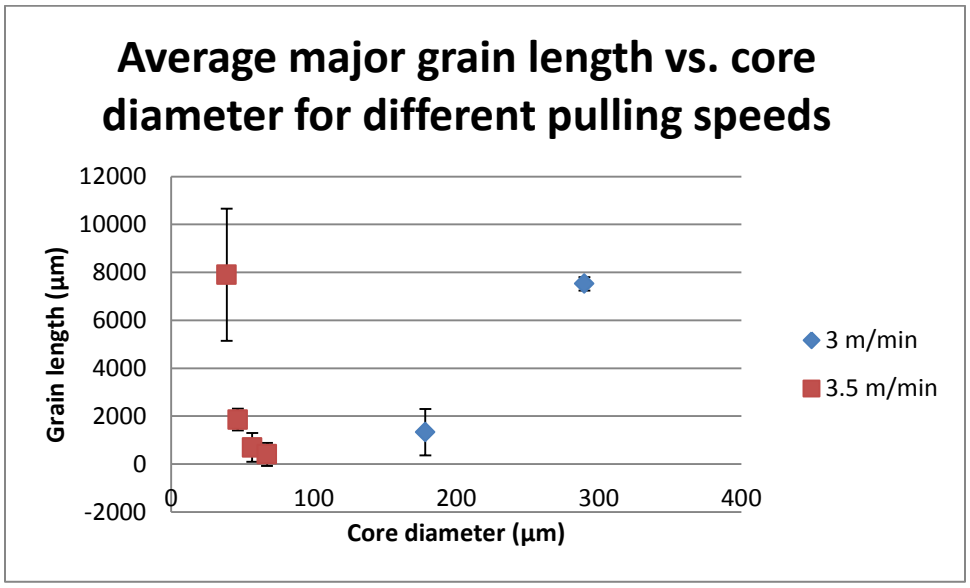

Figure 4.49 Average major grain length vs. core diameter for sample pulled at 3 and 3.5 m/min

The trend of the data for fibers from the 3 m/min pulling speed group is linear, but only 2 points were obtained for that group. The relationship is thought to be linear because the solidification velocity is a linear function based on the undercooling of the liquid and as the undercooling increases the velocity will also increase. In competition with the linear function of the solidification velocity is the rate of nucleation which for small undercooling will also be approximately linear. For the larger grain, the undercooling will be smaller and the growth rate will dominate. As the undercooling increases, the nucleation rate in front of the solid-liquid interface will start to dominate at large undercooling. Formation of grains when a higher undercooling is present means that the likelihood of nucleation of a grain in the liquid ahead of the solidification front is greater.

Since the length of the fiber extracted from the torch is dependent on the pulling speed, it can be surmised that the length of the undercooled liquid zone in the fiber is also dependent on the pulling speed. Most of the figures that detail the grains in the fiber don't show more than a couple of grains within one region but rather one grain propagating along the core and then another grain starts. If the nucleation rate was high in the liquid ahead of the solidification front there would be more regions with small grains packed closely together without taking up the entire cross section of the core. This trend indicates that the nucleation rate is relatively low and that it influences the overall grain length, but does not dominate over the solidification velocity due to a low undercooling of the liquid.

The data points for the 3.5 m/min are not linear as would be expected. This anomalous behavior is not understood. One possible explanation could be that the formation of a capillary tube in the silica cladding prior to filling in of the tube by wicking in silicon by capillary pressure is dominating. This was observed in several fibers during the fabrication process. Identification of these fibers is done by looking at the ratio of the outside diameter to the inside diameter of both the preform and the fiber. These two ratios are then compared and if they are not the same, then some alteration occurred during drawing that lead to the change. In the case of the fiber samples in the 3.5 m/min group the ratio is much smaller than the preform ratio. When this type of capillary tube would form, the silicon would wick into the tube several seconds after the tube started to be pulled from the end of the preform. Several seconds translates into a length of 175 to 200 mm for a drawing speed of 3.5m/min. With the silica tube leaving the hot zone before the silicon, it will cool substantially before the silicon is wicked into the tube. When the

silicon leaves the hot zone it does so very quickly and essentially at the same temperature. It is estimated that the time is less than 0.5 seconds. As the silicon leaves it starts to cool with the portion leaving first cooling the most. Upon arriving to this cold area, the silicon solidifies and the liquid silicon behind it has a small fraction of heat energy above the solid silicon in front of it. This proceeds until the solidification front encounters an area sufficiently far away to have been independently cooled and thus nucleates the beginnings of a grain. Figure 4.50 shows the next 2 groups based on the pulling speed of 4 and 4.5 m/min. The points in both groups show a linear relationship between the core diameter and the length of the major grains in the sample. Within each group, as the core diameter increase so does the average length of the major grains. Average major grain lengths of the individual samples of both groups have some variance in the length of the major grains with one sample having a large variation.

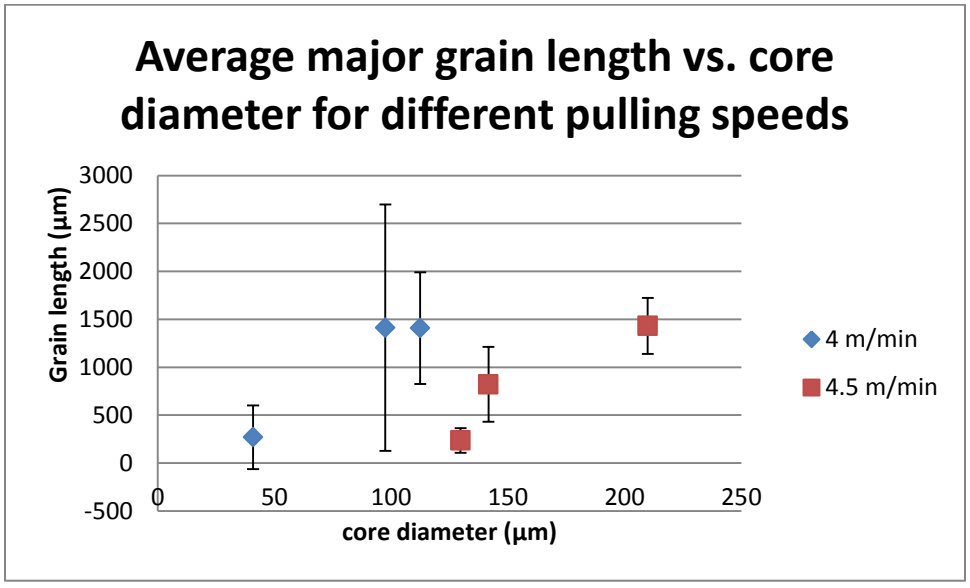

Figure 4.50 Average major grain length vs. core diameter for samples pulled at 4 and 4.5 m/min.

The trends established by the data points in Figure 4.50 appear to be linear as is expected and discussed in the previous section about the data in Figure 4.49. Data in the Figure 4.50 shows that for these pulling conditions the average major grain length increases with an increase in the core diameter. One of the notable items is the close proximity of the largest core diameter in the 4 m/min group and the smallest in the 4.5 m/min group. The core diameters are close with the fiber in the 4.5 m/min group being larger. The average grain length is lower for the larger of the 2 core diameters. If the grain length was only dependent on the core diameter then the grain length would be linear across all pulling conditions. Since the grain length decreases for similar core diameters with an increase in pulling speed, there is also a dependence on the pulling speed on the grain length. The dependence on pulling speed is a result of the difference in the thermal history or rate of cooling and the amount of undercooling that the core experiences between the different pulling speeds. As the pulling speed is increased, the fiber is drawn out of the hot zone at a faster rate. The rate of cooling will increase because the fiber spends less time in the hotter environment and this will increase the cooling rate. This will increase in the amount of undercooling present in the liquid silicon. This will increase the probability of nucleation of a crystal in the liquid that is ahead of the solidification front leading to a reduction in the average grain length.

Figure 4.51 shows data for samples with similar wall thickness and includes data points that have different pulling speeds. The points show that when the wall thickness is controlled, the average grain length of the major grains increases with an increase in the

core diameter. The scatter in the data may result from the influence of the different pulling speeds of the samples in the group.

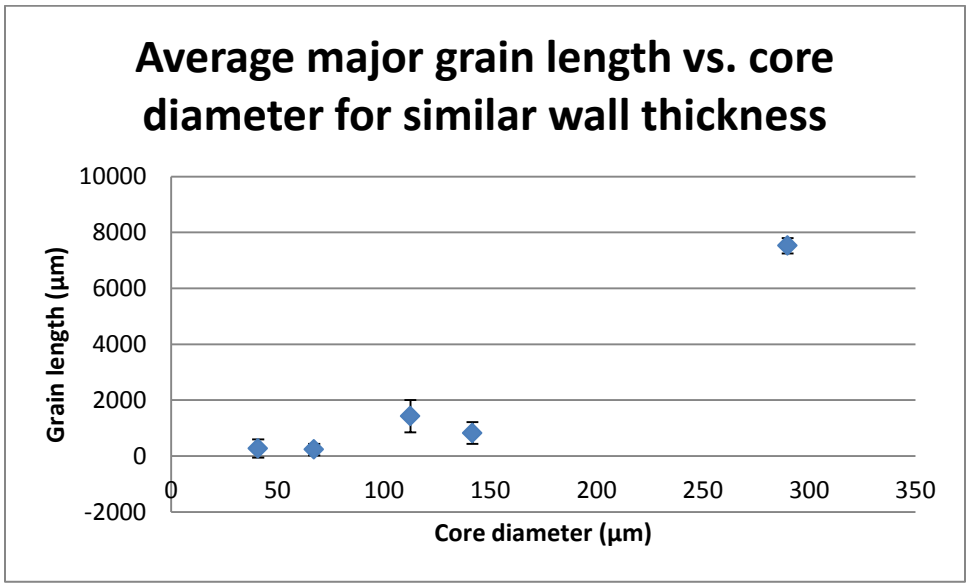

Figure 4.51 Average major grain length vs. core diameter for similar wall thickness samples

In controlling for the wall thickness, the effect of the cladding is somewhat neutralized. The impact of any absorption as the heat radiation travels through the cladding will be close to the same for all samples. Since the radii of the cores and outside diameters in the cladding are not similar, the heat energy contained is not the same. The heat content of the cladding and any radiation related to this heat content in the direction of the core will not be the same. The effect that this may have on the solidification is not eliminated in looking at this data in this manner. A linear trend is thought to exist for grain size as function core diameter. This relationship along with that established in Figure 4.51 and Figure 4.50 shows that the cladding thickness has some effect on the solidification of the

core, otherwise the data would establish a linear trend across all pulling speed groups. Understanding what the effect is would require more experimentation.

The previous results with the 3 different silicon core fibers and the GaSb fiber led to the experiment to determine the type of grain structure in these types of fibers. Many fiber drawing trials were conducted with the most successful preforms for the drawing of fibers being the 10 mm OD/2 mm ID (10/2) preforms. Success was measured as the ability of fibers to be pulled in consecutive trials from the same preform. The 10 mm OD/ 1 mm ID (10/1) and the 15 mm OD/1 mm ID preforms were difficult to fabricate resulting in short lengths of useable preform because only 1-2 cm of silicon would get sucked into the center tube. Such a short length doesn't leave enough room to be able to fuse a pulling rod onto the end and still have a useable section of silicon left. None of the10/1 or the 15/1 preforms produced any useable fibers due to the short length of the preform. The other preform that didn't produce any fibers was the 15 mm OD/ 3 mm ID (15/3) preforms. These preforms had sufficient length to pull fibers, however the fibers would explode upon freezing of the silicon core. If heat was removed from the preform after the silicon was molten the preform would also explode. Samples analyzed represent fibers drawn from the 10/2, 10/3, and 15/2 preforms. During the fiber drawing trials it was observed that some of the fibers are formed by the silicon being pulled into the core region after a tube is pulled from the end of the preform. This type of capillary action is represented in the different ratio (Δ ratio) of the core diameter to the cladding thickness. The grain structure does appear to have some dependence on this type of core formation in addition the fibers with the best core integrity were formed in this manner. Fibers that

were pulled in trials that exhibited capillary action produced the smallest cores and the longest lengths of continuous core fibers.

Preforms made with the vacuum forming method allowed for an easier time in pulling fiber from the preforms. The solid form of the silicon completely fills in the core of the preform. Upon melting of the section that was under flame, there is a significantly reduced free area for the molten silicon to escape. The heat zone thereby allows maintenance of the temperature of the silicon prior to pulling. In addition to a more consistent pulling condition, the solidification of the silicon during the fabrication of the preforms provided a tight seal between the silicon and the silica due to the volume expansion of the silicon. Due to this seal, none of the preforms were put under vacuum during pulling and none of the fibers pulled or the remaining parts of the preforms showed any evidence of crystalline silica formation due to the oxidation of the silicon. Crystalline silica would either form a white layer between the core and cladding or as a non-silicon crystalline phase in the EBSD scans. However, this behavior was observed in the powder –in-tube type preforms. This observation does not dismiss that oxidation of the silicon presenting itself as amorphous silica may occur as this was not tested for in any of the fiber samples made from these preforms.

The data collected from the EBSD scans show several types of grains configurations forming during the fiber pulling. Figure 4.51 shows that with a similar wall thickness the average grain length increases with increasing core diameter. The trend for the 3.5 m/min series in Figure 4.49 is opposite of the other 3 series. This is thought to have occurred due

to the formation of a capillary tube from the preform prior to filling with silicon. In general, the trend is that as the core diameter increases so does the average grain length for the major grains. The general trend shows that the grain size is influenced by the heat transfer out of the core. As predicted, the larger the core, the longer the grain due to the lower undercooling at the time of nucleation resulting in fewer nucleation of grains.

When taken together, the plots show that the grain length is dependent upon the wall thickness and core size within a specific pulling speed during the fabrication. Specific conditions at the time of fabrication are also relevant, such as the formation of a tube prior to the forming of the core. In all fiber drawing trials, the average grain length for the major grain in the core were all of sufficient lengths in order to be utilized as a basis for fabricating electronic structures in the core. Even the smallest average size is around 300 μm which is of sufficient depth for the fabrication process.

With the dependence of the grain length on pulling speed, core diameter and the factors that influence the ratio difference, the fiber can be fabricated so that the average grain length can be increased or decreased in different core diameters by changing the ratio difference and pulling speed to achieve the desired effect.

5. Thermal Model

In understanding the process of solidification of the silicon core it is useful to look at the rate of cooling of both the core and cladding regions and developing a model. The fiber is pulled from the hot zone with the core in the temperature range of 1950 °C to 2050 °C and Silicon freezes at 1412 °C. Heat transfer in this range is thought to be primarily

radiant, so convective and conductive methods are neglected in developing the model of the heat loss. The model that is developed is simple and is only intended to understand the approximate cooling rates of the core and the temperature gradients in the solidified portions. This will assist in understanding how the core diameter affects the final properties of the fiber such as cracks and grain size in the core. A simple approach was used to determine the rate of heat loss in the core. The equation used for heat transfer is given by the Stefan-Boltzmann law as shown in Equation 25.

$$-q_c = \varepsilon\sigma\left({T_c}^4 - {T_{rm}}^4\right) \tag{25}$$

Where ε is the emissivity of the solid or liquid silicon, σ is the Stefan-Boltzmann constant, T_c is the temperature of the core, and T_{rm} is the temperature of the room. The model assumes that the heat loss is primarily radiant in the radial direction and the heat distribution in the liquid and solid is uniform so as to neglect conduction in the calculation. This assumption can be justified by the small length scale since the diameters of the fiber cores are in the 40 to 300 micron range. The radiant heat loss is assumed to be from surface radiation. At room temperature and up to around 800 °C silicon has about 55% transmittance. Silicon is opaque above 800 °C to the wavelengths that make up the bulk of the heat transfer.[26-28] The percentage of heat emitted from the core was calculated out to a wavelength of 5 μm from 2000 °C to 1000 °C. Graphical representation is shown in Figure 5.1 with the percent of total emissive power shown on the right side of the graph legend.

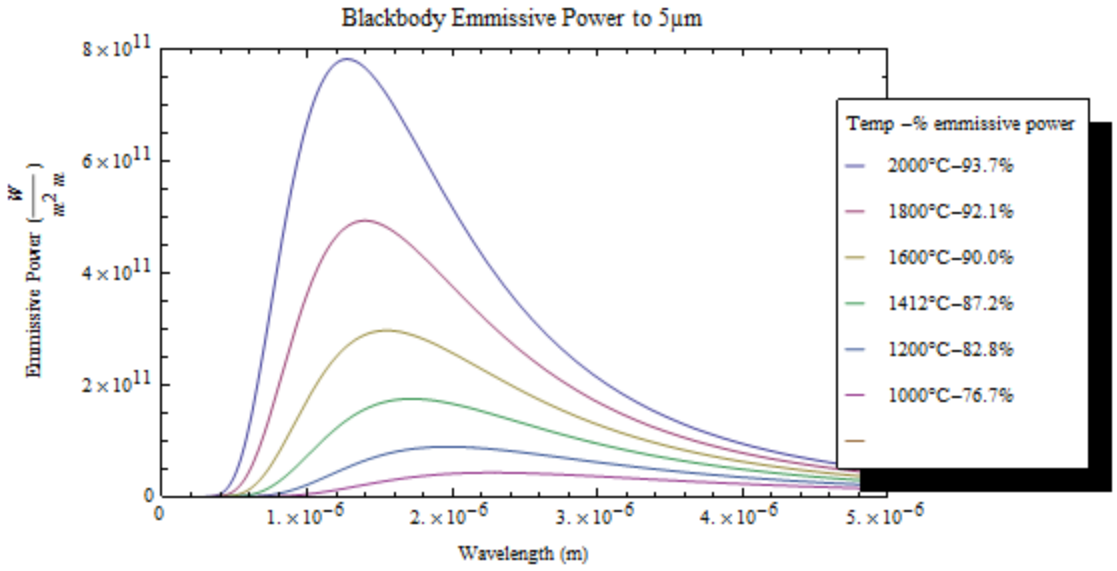

Figure 5.1 Emissive power to 5 μm from 2000 °C to 1000 °C with percent of total emissive power

Figure 5.1 shows that the amount of emissive power at the melting point of silicon is about 82%. Silicon is opaque in these wavelength regions so surface radiation holds, however the transmission window of the 214D silica used for the cladding extends out to about 3 μm with greater than 90% transmittance and a 5 μm transmittance limit. The model assumes that the bulk of the radiation from the core is transmitted thru the cladding. The radiation which is not transmitted is assumed to be absorbed and then reradiated by the cladding into the surrounding environment. Additionally, it is assumed that the cladding loses heat at greater rate than the core since it is transparent to the wavelengths of radiation that makes up the bulk of the radiant heat transfer. This transparency leads to a greater cooling rate since the interior volume elements of the cladding will all be radiating heat energy to the outside environment at the same time. The representative transmittance curve for the fused silica used is shown in Figure 5.2.

The product transmittance curves for the cladding glass used can be found at http://www.quartz.com/gedata.html#optics.[29]

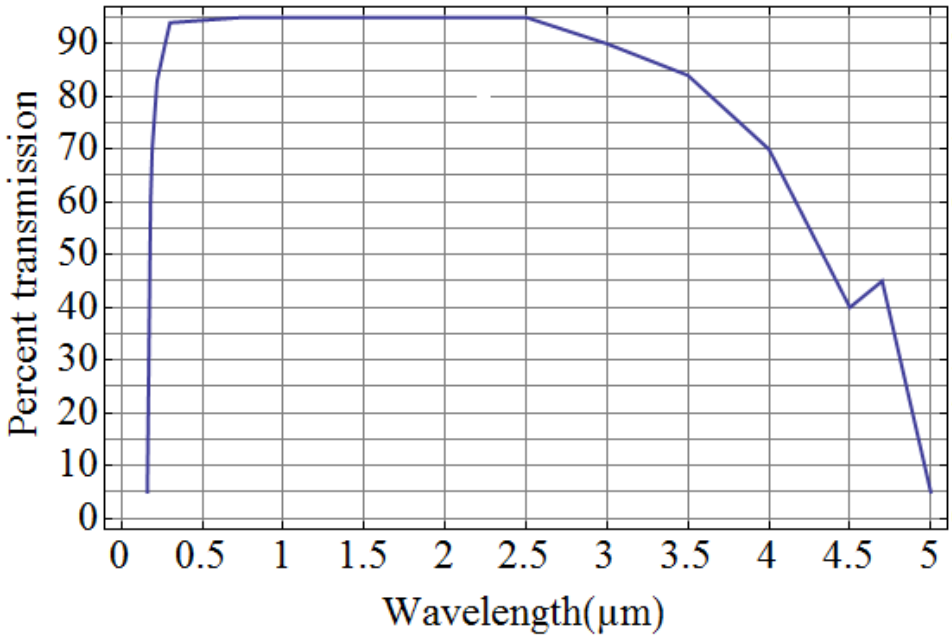

Figure 5.2 Transmittance curves for GE fused quartz

In addition to the heat loss being calculated, the amount of heat in the core is calculated for the different fiber samples. Both the heat loss and heat input calculations were done with a program written in Mathematica. Mathematica code used for computation is shown in Appendix B. The temperature range was from 2000 °C to 1000 °C with the removal of the heat of fusion at 1412 °C. Removal of the heat of fusion at 1412 °C was chosen because there was no way to predict the amount of undercooling that the core will experience prior to the beginning of solidification.

5.1.1 Fiber drawing schematic

The model for the heat transfer is based on using a fiber section that is a slice of the fiber whose normal is parallel to the fiber optical axis. If the fiber section is thin enough it can be used to calculate the radial heat transfer due to radiation while neglecting conduction along the fiber axis. A slice can be then used to determine the heat profile in the fiber as a function of time, and thus fiber length, since the length is dependent on the drawing speed during fabrication. The length of fiber that is extracted from the hot zone is given by Equation 26.

$$Fiber\ length(L) = draw\ speed(\frac{mm}{s})\ x\ time(s) \qquad (26)$$

The fiber length will be made up of a number of slices of unit length with each successive slice having a higher temperature than the preceding one. As the fiber exits the hot zone during fabrication it is assumed that it has the peak temperature of the torch which is 2000 °C. Once it leaves the hot zone the slice immediately starts to radiate heat to the ambient air at 20 °C. This is a simplified model due to the fact that a temperature gradient most likely exists within the hot zone, but the model will allow for an approximation of a cooling curve for the different diameters without the added complication of taking into account of the hot zone temperature gradient. In this simplified model, as a fiber slice is removed from the hot zone it begins to cool independent of the fiber slice that follows it out of the hot zone. Since the heat transfer is assumed to be radiant in the radial direction, any temperature gradients will be established in that direction ensuring a more even heat distribution in that direction. The temperature gradient over the length of the fiber along

the direction of the fiber axis will be large. Locally the temperature difference will be small compared to the radial direction so that the slices can be approximated with independent radial heat loss. The temperature difference of one fiber slice to another will be determined by the time it takes to draw that length of fiber. A schematic of the drawing and time dependence of the temperature is shown in Figure 5.3.

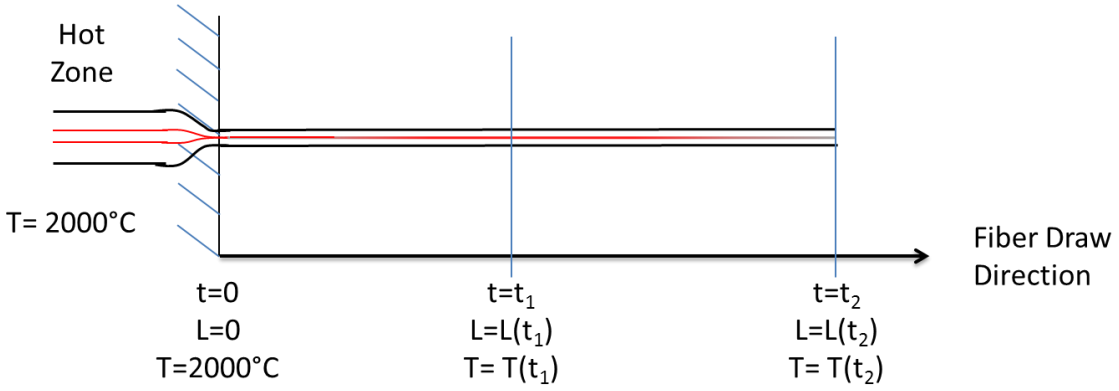

Figure 5.3 Time dependence on temperature profile in fibers during drawing

5.2 Heat Input

The amount of heat input into the core region was calculated initially by using data from a review paper[30] in which the heat capacity of the silicon was estimated from the presented graphs in a temperature range of 20 °C to 2150 °C. The points were then plotted in Excel and an equation fitted to the data. At the melting point of silicon there is a discontinuity in the density and in the heat capacity. Graphs of both series were made with fitted equations. The data and graph with the fitted equations is given in appendix

A. These equations were then used to determine the amount of heat in the core at a given temperature. The amount of heat in the core is given by Equation 27 for the solid phase and Equation 28 for the liquid phase.

$$q_{in-\,solid}\left(\frac{J}{gC}\right) = \int_{20}^{1412} -2x10^{-7}T^2 + 4x10^{-4}T + 0.724\,dT \qquad (27)$$

$$q_{in-\,liquid}\left(\frac{J}{gC}\right) = \{\int_{20}^{T} 3\times10^{-8}T^2 - 5\times10^{-5}T + 0.866\,dT\} + 1787.8(\frac{J}{gC}) \qquad (28)$$

Equation 27 was evaluated for temperatures from 20 °C to 1412 °C in 1 °C increments with the results having units of J/g and equation 28 was evaluated in 1 °C from 1412 °C up to 2000 °C. The amount of heat put into the core was dependent on the reflective nature of the core diameter. The transient nature of the heat input was accomplished by representing the heat as heat per unit length for a given core diameter or Q/L. The amount of heat content was calculated for core diameters of the fiber samples. The manner that the heat content of the core is calculated is shown in Equations 29.

$$\frac{Q}{L} = q_{in} * \rho(T) * A \qquad (29)$$

With ρ (T) being the temperature dependent density of silicon, V is the volume of silicon in the core and A is the cross sectional area of the core. The density of silicon was estimated in the same way as the heat capacity and the fitted equation and graph is included in appendix A. The rate of pull of the fiber is also the rate of extraction of the core from the heat source. In using the heat content in the form of Q/L, the heat is

described in a radial slice of the fiber. This allows for the transient nature of the temperature along the fiber due to pulling from the hot zone to be taken into account. A graph of the heat content in the large core fiber samples is shown in Figure 5.4 and of small core fiber samples is in Figure 5.5. All of the heat content calculations done in Mathematica and the graphs are included in appendix B.

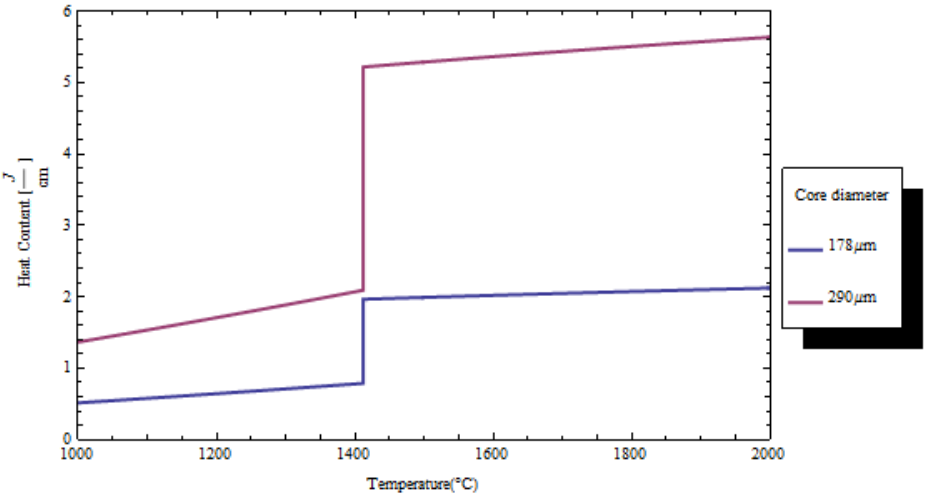

Figure 5.4 Calculated heat content of large core fiber samples

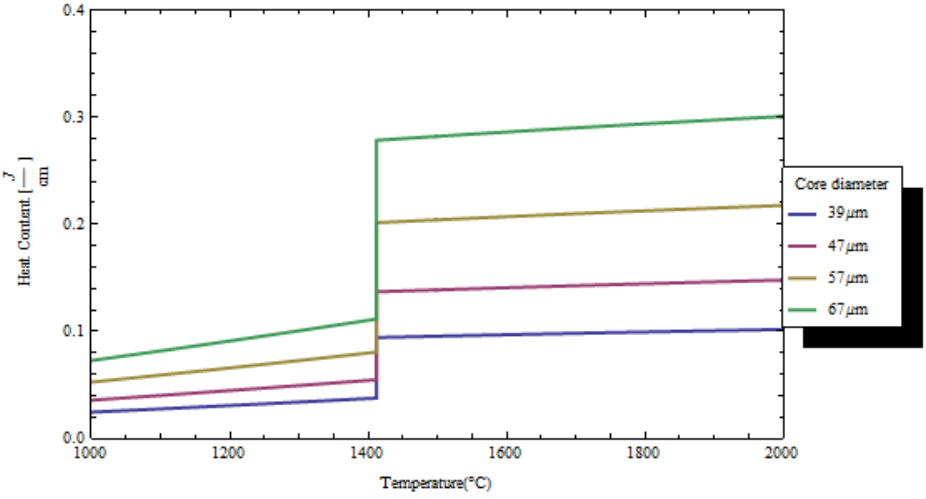

Figure 5.5 Calculated heat content of small core fiber samples

Figure 5.4 and Figure 5.5 shows that the cores of the fiber samples have a very low amount of heat energy per unit length, even at such a high temperature due to the small amount of material contained within the core. While the fibers are very hot, not much heat needs to be extracted to reduce the temperature of the core.

5.3 Heat Transfer

As stated in the beginning part of the section, this model of heat transfer assumes primarily radiant heat transfer in the radial direction with complete temperature uniformity in the liquid and solid portions of the core. This simplification allows for the Stefan-Boltzmann law to be used in the following manner for calculating the heat loss per unit length of the fiber. The emissive power of the core was calculated for the liquid phase from 2000 °C to 1412 °C prior to the solidification of the silicon and then of the solid phase from 1412 °C to 1000 °C after the solidification of the silicon was completed. At the onset of the removal of the heat of fusion, the emissivity in equation 25 was changed to the solid emissivity to account for an increase in emissive power by the formation of a solid skin on the surface of the core. As with the heat input into the core, the heat transfer out of the core was calculated per unit length. The equations used for the heat transfer out of the core are shown in Equations 30 and 31 which are for the solid and liquid phases of the core respectively.

$$\frac{P_{out\,solid}}{L_f} = C_f \varepsilon_s (T_{si}^4 - T_{rm}^4) \tag{30}$$

$$\frac{P_{out\ liquid}}{L_f} = C_f \varepsilon_l (T_{si}^4 - T_{rm}^4) \quad (31)$$

Where L_f is the unit length of the fiber, ε is the emissivity of the solid (ε_s) or liquid (ε_l), C_f is the circumference of the fiber, T_{si} is the temperature of the silicon and T_{rm} is the temperature of the room. The emissivity of the silicon in the solid state is 0.7 above 700 °C and 0.23 for the liquid silicon.[1, 31] Equations 30 and 31 were evaluated within the temperature ranges given and in 1 °C increments. Length of the fiber is dependent on the drawing speed during fabrication and in making the heat transfer emissive power a per unit length quantity it incorporates the time dependence into the heat transfer. This allows for the heat profile of the fiber to be generated from the cooling rate calculations.

5.4 Cooling Curves

The purpose of calculating the heat content of the core region and the heat loss was to generate a cooling curve for a specific core diameter. In order to generate these curves, the differential heat content of the core was calculated by subtracting the heat content at a temperature from the heat content 1 °C higher. This gives the amount of heat loss necessary to cause the slice to lose 1 °C. The differential heat content was calculated to go from 2000 °C to 1000 °C in 1 °C increments. Heat loss was also calculated in 1 °C increments from 2000 °C to 1000 °C so that at each change in temperature, the emissive power would change accordingly and the amount of heat loss at that temperature was used. Time was calculated by determined by using the amount of heat loss necessary to change 1 °C and the amount of power the core would radiate at that temperature. The

equation used to calculate the time is given in equation 32 which shows a variation of equation 29 divided by a variation of equation 31.

$$t = \frac{q_{in}(T_{hi})*\rho(T)*A - q_{in}(T_{low})*\rho(T)*A}{C_f \varepsilon_{s/l}(T_{hi}^4 - T_{rm}^4)} \quad (32)$$

Where T_{hi} is the higher temperature, T_{low} is the temperature 1 °C lower and $\varepsilon_{s/l}$ is the emissivity of phase that is being calculated. Equation 32 gives the time it takes in seconds to go from one temperature to another and was evaluated for the time it takes to go from 2000 °C to 1000 °C in 1 °C increments. The time was plotted against the temperature for all fiber samples. The plots were separated into groups based on drawing speed so that the results will be visible and distinguishable. Figure 5.6 to Figure 5.9 are the cooling curves for core diameters that are representative of the fiber samples in the 3 m/min, 3.5 m/min, 4 m/min and 4.5 m/min groups. Figure 5.6 shows the calculated cooling curves for 2 larger core fibers duplicating the 3 m/min group fiber dimensions. The time from exiting the hot zone to final solidification of the fiber slice is calculated to be 1.62 s for the 178 µm diameter fiber and 2.64 s for the 290 µm fiber. Figure 5.7 shows curves for the fibers in the 3.5 meter per minute group and the calculated time to solidification for the fiber slices from the smallest diameter to largest are 0.355 s, 0.429 s, 0.520 s, and 0.611 s respectively. The cooling curve for the 4 meter per minute draw speed group is shown in Figure 5.8. The solidification time for 3 diameter sizes in that group are 0.374 s, 0.884 s, and 1.021 s for the 41 µm, 98 µm and 112 µm diameter fiber slices respectively. Figure 5.9 is the cooling curve for the 4.5 meter per minute group and

shows solidification times of 1.185 s for the 129 µm diameter slice, 1.295 s for the 141µm diameter slice, and 1.915 for the 209 µm diameter slice.

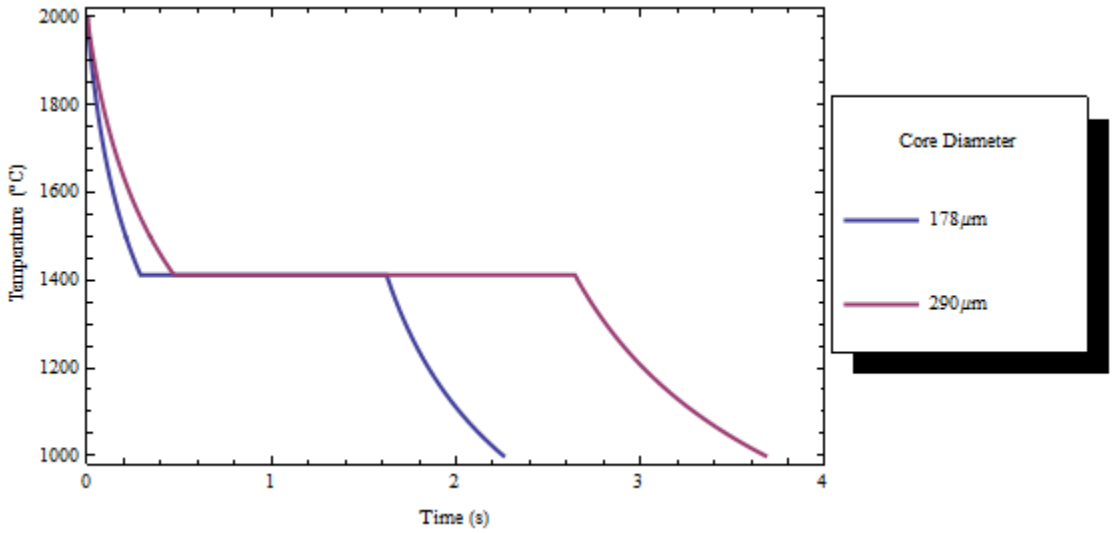

Figure 5.6 Calculated cooling curve for fiber samples from 3 m/min draw speed

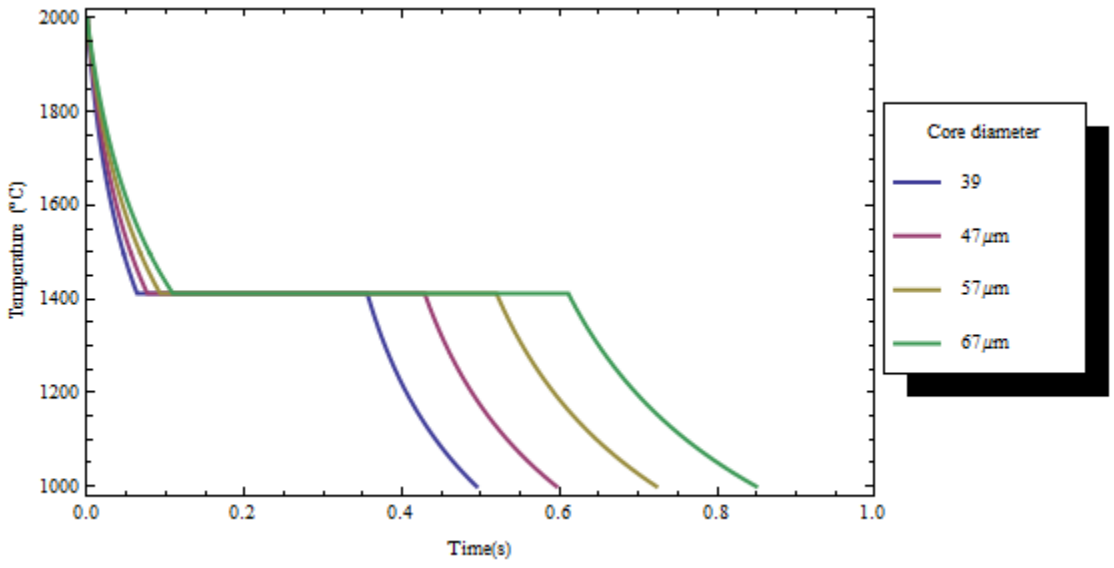

Figure 5.7 Calculated cooling curve for fiber samples from 3.5 m/min draw speed group

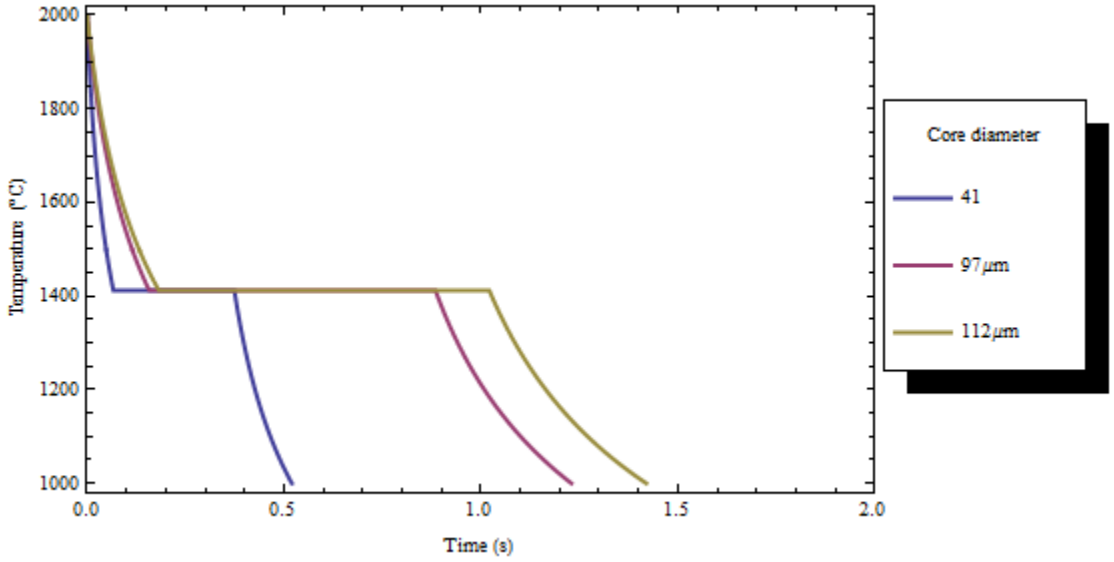

Figure 5.8 Calculated cooling curve for fiber samples from 4 m/min draw speed group

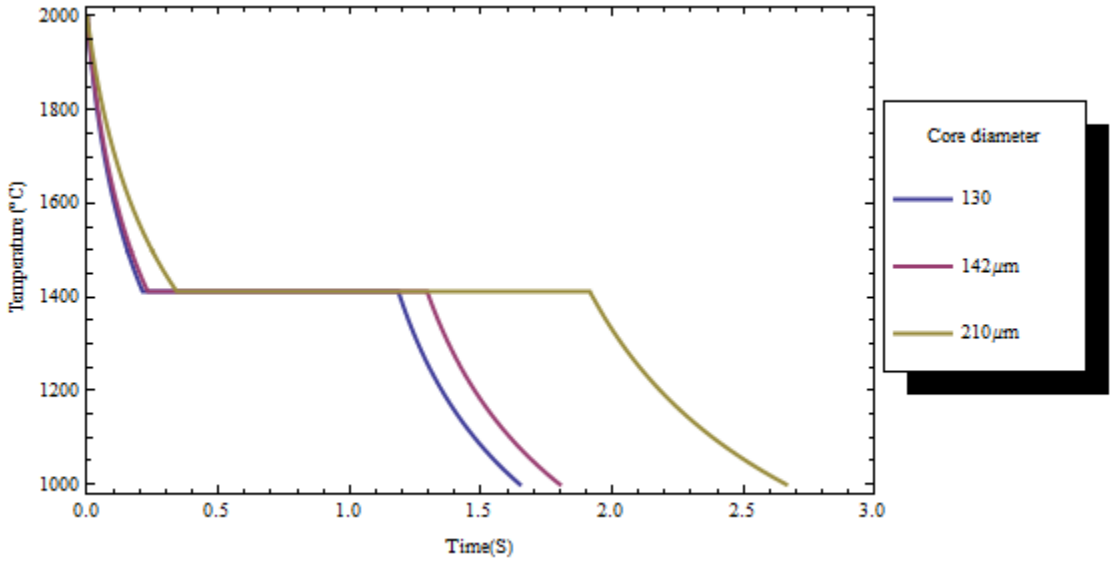

Figure 5.9 Calculated cooling curve for fiber samples from 4.5 m/min draw speed group

The graphs in Figure 5.6 to Figure 5.9 show that the cooling rate increases and the time to solidification decreases as the core diameter decreases. With an increase in the cooling rate, the amount of undercooling in the liquid silicon will be greater. Smaller cores will have a larger amount of undercooling at the area ahead of the solidification front. This will lead to a greater probability of nucleating a crystal. These graphs give an understanding of the how quickly the core can transfer the heat out. With the time to cool a fiber slice down to 1412 °C being less than a second and removal of all the latent heat in a few seconds, the extraction of heat is not the limiting factor in the solidification process. Solidification will mostly likely proceed at the speed of drawing of the fiber as the extraction of the fiber from the hot zone will determine how quickly the fiber can start to cool.

Cooling rates were calculated from the generated data. Rates were calculated by taking the time it took to cool from 1612 °C to 1412 °C prior to the onset of the removal of the heat of fusion divided by the temperature difference of 200 °C. The upper temperature was chosen because the graph from 1612 °C to 1412 °C is roughly linear and a good approximation of the cooling rates in vicinity of the solidification temperature. The cooling rates, time to solidification and time to cool to 1000 °C are shown in Table 5.1.

Table 5.1 Calculated cooling rates, solidification times, cooling time and time to draw a 10 mm length for all fiber diameters

Draw speed (m/min)	Core Diameter (μm)	Cooling Rate (°C/s)	Slice Solidification time (s)	Time to Cool to 1000 °C (s)	Time to pull 10 mm Section (s)
3.0	178	1299	1.62	2.27	0.20
	290	793	2.64	3.68	0.20
3.5	39	5900	0.36	0.49	0.17
	47	4938	0.43	0.60	0.17
	57	4000	0.52	0.72	0.17
	67	3425	0.61	0.84	0.17
4.0	41	5618	0.37	0.52	0.15
	98	2361	0.88	1.23	0.15
	112	2053	1.02	1.42	0.15
4.5	129	1773	1.19	1.65	0.13
	141	1613	1.30	1.80	0.13
	209	1099	1.92	2.66	0.13

The data generated can also be used to predict the temperature profile in the fiber as it is drawn from the hot zone. Temperature profiles of the fiber samples were determined for a 10 mm length of fiber. The length of time that the fiber has been drawn influences the temperature, so the parts of the fiber closer to the hot zone will be at a higher temperature. The time it takes to draw a 10 mm fiber varies by the drawing speed. The required drawing times for the fiber length for each group are included in Table 5.1. The temperature profiles were developed by taking the data used to produce the cooling curves. Temperatures were taken from the generated data at time intervals related to 1 mm increments along the fiber section. The time of the first point in the graphs is the point after which the fiber has been pulled to a length of 10 mm with one end just exiting

the hot zone at 2000 °C and the other at a temperature resulting from cooling for the duration of the drawing time. The second curve on the plots shows a later time for the same 10 mm section after the last portion of the fiber releases its heat of fusion. Temperature profiles for fiber lengths of 178 µm and 290 µm core diameter fibers are shown in Figure 5.10. These sizes represent fiber core diameters pulled in the 3 m/min drawing speed group. The temperature gradient visible in the figure for the 2 fibers are fairly large as there is approximately a 400 °C temperature difference over 10 mm in the 178 µm core fiber. Once the last part of the core in that length solidifies the temperature change is less than 200 °C for the 178 µm and even less for the large 290 µm core fiber.

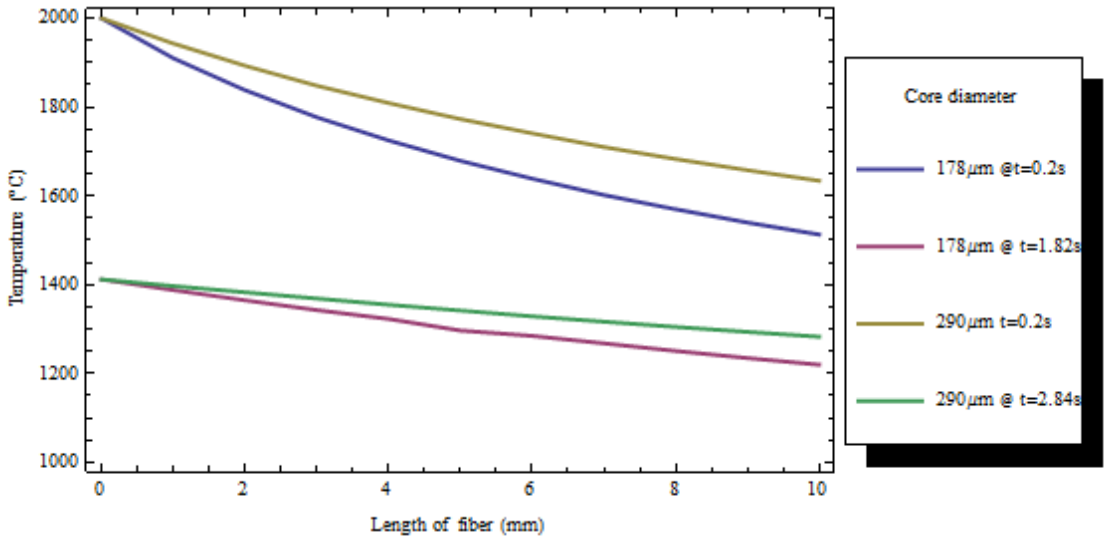

Figure 5.10 Calculated temperature profile for fiber lengths of fibers from the 3 m/min drawing speed group

Figure 5.11 shows the temperature profiles for fibers with core diameters similar to fibers in the 3.5 m/min drawing speed group. These small core diameters show steep temperature gradients in both the liquid phase and after solidification. In the liquid phase

the temperature drops almost 600 °C in 5 mm and around 400 °C in 10 mm in the solid phase. Figure 5.12 shows temperature profiles from core diameters similar to core diameters of fibers pulled in the 4 m/min drawing speed group. The temperature gradients are much larger for the 41 µm fiber than for the 2 larger fibers. The temperature profiles of the representative fiber cores from the 4.5 m/min drawing group are shown in Figure 5.13. Fibers in that group are all larger diameter core fibers and as can be seen in the graph, the temperature gradient along the 10 mm length is significantly less than the smaller core fibers seen in Figure 5.11.

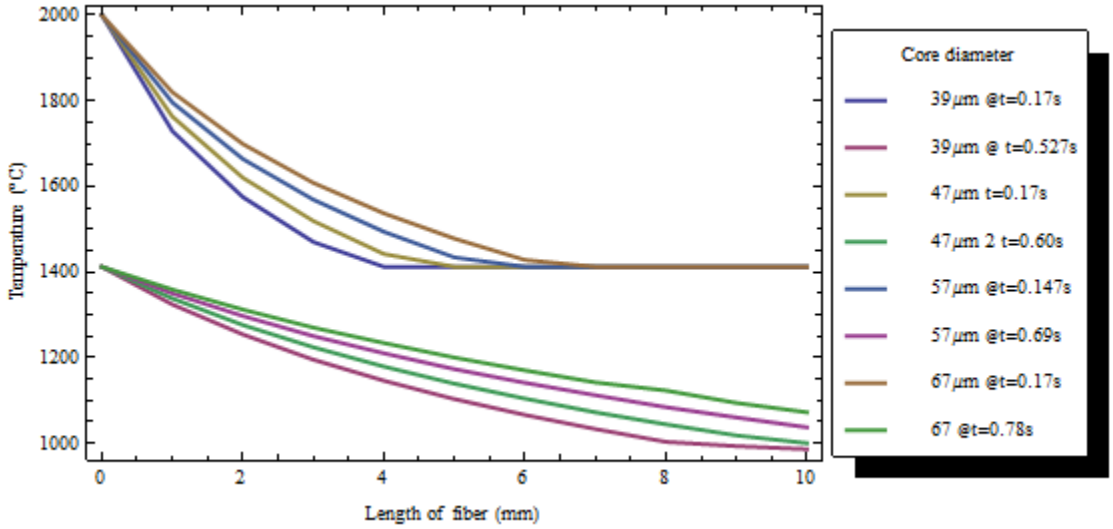

Figure 5.11 Calculated temperature profile for fiber lengths of fibers from the 3.5 m/min drawing speed group

Temperature profiles for fiber core diameters calculated in and shown in Figure 5.11 points out that the temperature gradient is higher in a smaller core fiber. When contrasted against the temperature profiles of the larger cores in Figure 5.10 and Figure 5.13 the temperature gradients are much larger. The explanation is simply that the amount of heat content in the fiber is much lower in the smaller core fibers in comparison to the amount

of area that is available to radiate heat energy. As the core diameter increases the surface area increases by the radius while the heat content of the core increases by square of the radius. This relates to a relationship where the cooling times increase by a factor of the difference in radius between 2 different diameter cores. This is illustrated in the cooling rates and cooling times shown in Table 5.1 where the calculated rates and times scale by the differences in the radii of the cores.

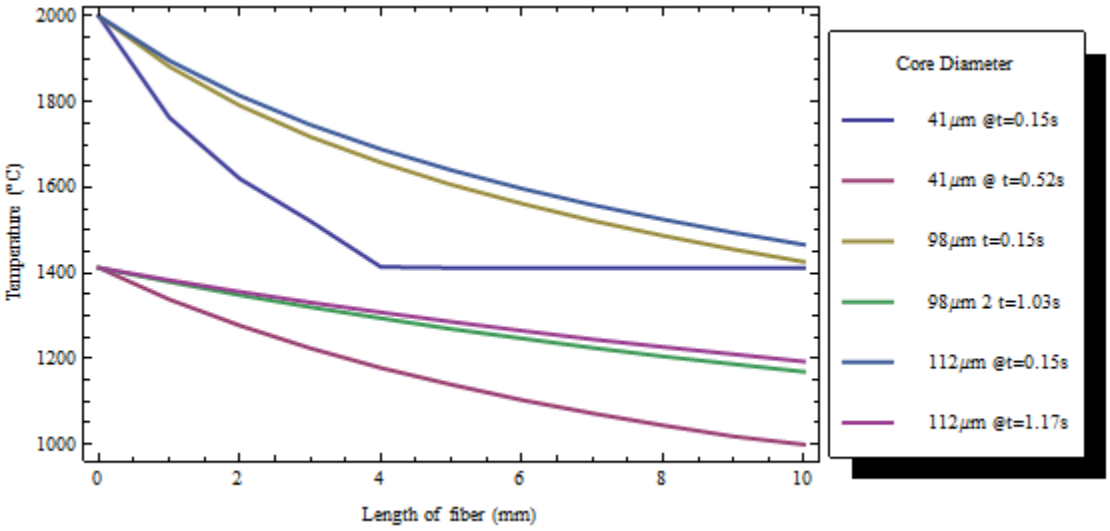

Figure 5.12 Calculated temperature profile for fiber lengths of fibers from the 4 m/min drawing speed group

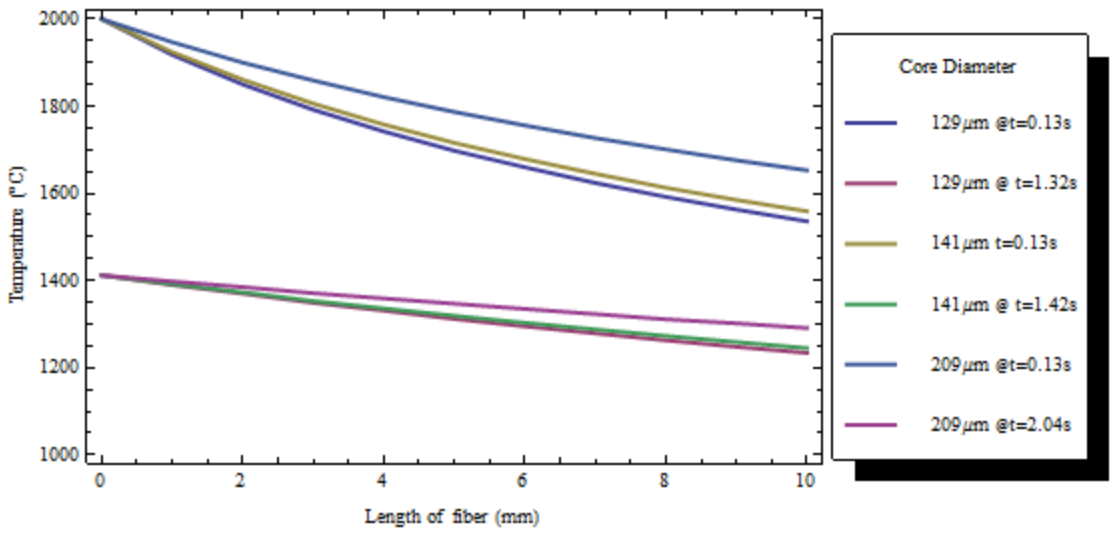

Figure 5.13 Calculated temperature profile for fiber lengths of fibers from the 4.5 m/min drawing speed group

The core diameters represented in Figure 5.10 are the largest of any of the fibers that were fabricated. These fibers show an average temperature gradient of around 40 °C/mm in the liquid phase and around 15 °C/mm in the solid phase. The lower temperature gradient in the liquid phase goes along with the lower cooling rates derived from the cooling curves in Figure 5.6. Calculated average temperature gradients in the liquid and solid phase are shown in Table 5.2.

Lower cooling rates and a lower temperature gradient within the liquid points to a small undercooling prior to the nucleation of grains. A small undercooling during grain nucleation in the area ahead of the solidification front will lead to the formation of fewer grains as the fiber core solidifies. This is shown in the average grain size of the fibers in the 3 m/min draw speed group detailed in Figure 4.49 with an average grain length of 1.33 mm for 178 µm diameter core fiber and 7.5 mm for the 290 µm diameter core fiber.

The temperature gradient in the solid phase is less beneficial for the core structure for these large diameter cores. During solidification, the silicon expands roughly 10 % by volume and this expansion will induce a significant amount of stress if the expansion is constrained. After solidification, the silicon will begin to contract as its density goes back up. With a low temperature gradient, the contraction of the core will be very small along the length of the fiber. This will cause a high stress state in all 3 dimensions leading to the formation of cracks in the core as a stress relief mechanism. The spacing of cracks can be seen in the optical micrograph of the 290 μm diameter core fiber in Figure 4.21 showing cracks every 0.5-1.0 mm.

Table 5.2 Calculated liquid and solid silicon temperature gradients

Draw Speed (m/min)	Core Diameter (μm)	Liquid Temperature Gradient (°C/mm)	Solid Temperature Gradient (°C/mm)
3 m/min	178	49	19
	290	37	13
3.5 m/min	39	176	51
	47	139	41
	57	113	37
	67	95	34
4 m/min	41	147	44
	98	57	24
	112	53	22
4.5 m/min	129	46	18
	141	44	17
	209	34	12

In the modeling of the heat transfer, the temperature gradient of the heat source was not taken into account. The relationships established in Figure 4.49 and Figure 4.50 shows that the pulling speed affects the average grain length. This can be seen to be the case when you look at the cooling curves in Figure 5.6 to Figure 5.9 and in the temperature profiles in Figure 5.10 to Figure 5.13. A fiber with the same dimensions should have the same cooling rates and approximately the same grain structure. When pulled from the hot zone at a slower rate, the fiber will experience a longer time in hotter conditions. With the rate of heat transfer a function of the temperature differential, the amount of heat loss will be less than for a fiber that moves quickly through the heat zone. This decreased heat loss will reduce the cooling rate and the amount of undercooling present as the liquid approaches the melting temperature.

6. Conclusion

The production and fabrication of semi-conductor core optical fibers is shown to be feasible and controllable. Useable fibers with cores of silicon, boron and phosphorous doped silicon, and gallium antimonide were demonstrated. Dimensions on the order of 10 μm for core diameters are readily achievable with a preform heat and draw method that is standard in the drawing of optical fibers. Utilization of either a powder-in-tube preform or a solid core preform produces fibers with a variety of fiber dimensions depending on the fabrication parameters. Powder-in-tube semi-conductor preforms have a compositional flexibility, but fabrication of the fibers is more difficult due to volume contraction during melting of the material and the tendency of the molten material to escape the hot zone. Solid core performs fabricated by vacuum forming are easier to use

in the pulling of fibers with less overall fluid movement during fiber pulling. Overall, there is greater ease and dimensional control with the use of the solid core preform.

Feasibility of fabrication of semi-conductor core optical fibers has been shown. Not only for high temperature semi-conductors like silicon clad in silica, but also for a low temperature material like gallium antimonide clad in a relatively low softening point borosilicate glass. It is possible to adapt the glass composition to accommodate the semi-conductor material chosen. Fiber size is scalable to a traditional drawing system and any length of fiber should be able to be made. The fibers have continuous cores with the ability for optical transmission showing potential use for optical transmission in conjunction with opto-electronic structures. Cores in these fibers are poly crystalline with varying grain lengths that have a dependency on the specific pulling conditions and the resultant fiber dimensions.

The grain lengths of the major grains in the core generally increase in length with an increase in core diameter. Average grain lengths are dependent on the core diameter, furnace profile and the pulling speed of the draw process. Grain lengths are suitable in all fibers for use in fabrication of electronic structures in the core region with even the smallest average grain length of around 300 μm. This grain structure satisfies the grain boundary requirements for fabrication of boundary free p-n junctions and other more complicated electronic structures. Best fiber quality was achieved with a high ratio difference small core fiber. This configuration produced fibers which had a long grain and few physical defects over the 1 mm length scanned.

7. Unique accomplishments

Several contributions to the literature have come about in the course of the fabrication of the semi-conductor core fibers and the experiments on understanding how the fabrication parameters affect the grain structure. Those contributions are:

- Fabrication of the first optical fiber sized silicon core fiber
- Fabrication of the first n-type doped silicon core fiber
- Fabrication of the first p-type doped silicon core fiber
- Fabrication of the first n-type GaSb core fiber
- Design and fabrication of a vacuum forming method for semi-conductor core preforms
- The first experimental results on the fabrication dependence of the grain structure in n-type silicon fibers
- Determination that the grain size is dependent on the core diameter, furnace profile and pulling speed during fabrication.

8. Future work

The area of semi-conductor optical fibers is a relatively new area in the research arena and as such there is significant work still to be done. Work still to be done can be broken into 2 areas; the first is in fabrication of the fibers and controlling the cores and second is the functionalization of the fiber. In the area of fabrication, additional work needs to be done to understand the fabrication parameters that cause the ratio difference between the

preform and the fiber. In the follow up work on understanding the ratio difference, the role of capillary formation, the wicking of silicon into the capillary and its effect on the solidification of the silicon also needs to be investigated. Duplication of this work in part on a draw tower is also warranted due to the more consistent and reproducible conditions inherent in that type of setup while also eliminating the effect of gravity during the fiber fabrication. In addition to duplication, expansion of the pulling speed portion of the trials is desirable to drive the core diameters to as small as possible as well as to develop either extremely long grains or amorphous core structures.

Work on functionalizing the fiber includes the understanding of the fiber optical properties, fabrication of electronic structures, in-fiber circuit design and inter-action between the optical properties and the in-fiber structures. The optical properties of the fibers weren't characterized in this work and the relationship between the fabrication of the fibers and how the optical properties change is necessary for full utilization of the fibers. One of the interesting areas that the development of these fibers opens up is the possibility of fabrication of electronic structures in the core. None of this work has been done to date, so all of the fabrication work in developing these structures still needs to be accomplished. In addition to fabrication of the structure, understanding and designing circuits that will work in the fibers needs to be completed. Finally, work needs to be done to understand the interaction of the optical side of the fiber performance with the use of in-fiber electronic structures and devices in order to design and fabricate useful structures.

References

[1] G. Z. Mashanovich, G.T.Reed, B. C. Timotijevic, and S. P. Chan, "Silicon Photonic Waveguides," in *Silicon Photonics: State of the Art*, G. T. Reed, Ed., ed Hoboken: John Wiley and sons, Ltd, 2008.

[2] G. T. Reed and A. P. Knights, *Silicon Photonics*: Hoboken, 2004.

[3] R. Jones, H. Rong, H.-F. Liu, and M. Paniccia, "Silicon Photonic Applications," in *Silicon Photonics: State of the Art*, G. T. Reed, Ed., ed Hoboken: John Wiley and Sons, Ltd, 2008.

[4] B. Scott, K. Wang, and G. Pickrell, "Fabrication of N-type Silicon Optical Fibers," *Photonics Technology Letters*, vol. 21, pp. 1798-1800, 2009.

[5] P. J. A. Sazio, A. Amezcua-Correa, C. E. Finlayson, J. R. Hayes, T. J. Scheidemantel, N. F. Baril, B. R. Jackson, D. J. Won, F. Zhang, E. R. Margine, V. Gopalan, V. H. Crespi, and J. V. Badding, "Microstructured optical fibers as high-pressure microfluidic reactors,," *Science 311, 1583-1586*, vol. **311**
pp. 1583-1586
2006.

[6] J. Ballato, T. Hawkins, P. Foy, R. Stolen, B. Kokuoz, M. Ellison, C. McMillen, J. Reppert, A. M. Rao, M. Daw, S. R. Sharma, R. Shori, O. Stafsudd, R. R. Rice, and D. R. Powers, "Silicon optical Fiber," *Opt. Express*, vol. 16, pp. 18675-18683, 2008.

[7] P. Klocek, Ed., *Handbook of infrared Optical Materials*. New York: Marcel Dekker, Inc, 1991, p.^pp. Pages.

[8] J. Ballato, T. Hawkins, P. Foy, B. Yazgan-Kokuoz, R. Stolen, C. McMillen, N. K. Hon, B. Jalali, and R.Rice, "Glass-Clad single-crystal germanium optical fiber," *Optics Express*, vol. 17, pp. 8029-8035, 2009.

[9] B. Scott, K. Wang, and G. Pickrell, "Fabrication of N-type Silicon Optical Fibers," *Photonics Technology Letters*, vol. 21, pp. 1798-1800, 2009.

[10] J. Ballato, T. Hawkins, P. Foy, C. McMillen, L. Burka, J. Reppert, R. Podila, A. M. Rao, and R. R. Rice, "Binary III-V semiconductor core optical fiber," *Opt. Express*, vol. 18, pp. 4972-4979, 2010.

[11] S. Adachi, "Gallium Antimonide," in *Handbook on Physical Properties of semiconductors*
vol. 2- III-V compound semiconductors, ed Boston: Kluwer Academic Publishers, 2004, p. 446.

[12] A. G. Milnes and A. Y. Polyakov, "Gallium antimonide device related properties," *Solid-State Electronics*, vol. 36, pp. 803-818, 1993.

[13] A. Aardvark, G. G. Allogho, G. Bougnot, J. P. R. David, A. Giani, S. K. Haywood, G. Hill, P. C. Klipstein, F. Mansoor, N. J. Mason, R. J. Nicholas, F. Pascal-Delannoy, M. Pate, L. Ponnampalam, and P. J. Walker, "Devices and desires in the 2-4 micron rgion based on antimony-containing III-V heterostructurs grown by MOVPE," *Semiconductor Science and Tehcnology*, vol. 8, pp. S380-S385, 1993.

[14] H. K. Choi and G. W. Turner, "GaSb-based mid-infrared quantum well diode lasers," in *Laser Diodes and Applications*, San Jose, CA, USA, 1995, pp. 236-243.

[15] E. A. Grebenshchikova, A. N. Imenkov, B. E. Zhurtanov, T. N. Danilova, A. V. Chernyaev, N. V. Viasenko, and Y. P. Yakovlev, "Properties of GaSb-Based Light-

Emitting Diodes with Chemically Cut Substrates," in *Semiconductors* vol. 37, ed: Springer Science & Business Media B.V., 2003, pp. 1414-1420.
[16] C. R. M. Grovenor, "Grain Boundaries in Semiconductors," *Journal of physics C: Solid State Physics,* vol. 18, pp. 4079-4119, 1985.
[17] J. Orton, *The story of Semiconductors*. New York: Oxford University Press, 2004.
[18] L. LIAO, D. R. LIM, A. M. AGARWA, X. DUAN, K. K. LEE, and L. C. KIMERLING, "Optical Transmission Losses in Polycrystalline Silicon Strip Waveguides: Effects of Waveguide Dimensions, Thermal Treatment, Hydrogen Passivation, and Wavelength," *Journal of Electronic Materials,* vol. 29, 2000.
[19] J. F. Hamet, R. Abdelaoui, G. Nouet, and G. Allais, "Precipitation at Grain Boundaries in Silicon," *Materials Science and Engineering,* vol. B4, 1989.
[20] E. Schroer, S. Hopfe, P. Werner, U. Gosele, G. Dushcer, M. Ruhle, and T. Y. Tan, "Oxide precipitation at silicon grain boundaries," *Applied Physics letters,* vol. 70, pp. 327-329, 1997.
[21] A. K. Sinha, *Physical Metallurgy Handbook*. New York McGraw-Hill, 2003.
[22] A. K. Varshneya, *Fundamentals of Inorganic Glasses*. Boston Academic Press, Inc, 1994.
[23] J. Winkler, M. Neubert, J. Rudolph, N. Duanmu, and M. Gevelber, "Czochralski Process Dynamics and Control Design," in *Crystal Growth Processes Based on Capillarity*, T. Duffar, Ed., ed West Sussex: John Wiley & Sons, LTD, 2010, pp. 115-202.
[24] A. Ludge, H. Riemann, M. Wunscher, G. Behr, W. Loser, A. Muiznieks, and A. Croll, "Floating Zone Crystal Growth," in *Crystal Growth Processes Based on Capillarity*, T. Duffar, Ed., ed West Sussex: John Wiley & Sons, LTD, 2010, pp. 203-276.
[25] A. G. Cullis, N. G. Chew, H. C. Webber, and D. J. Smith, "Orientation dependence of high speed silicon crystal growth from the melt," *Journal of Crystal Growth,* vol. 68, pp. 624-638, 1984.
[26] K. D. Li and P. M. Fauchet, "Drude parameters of liquid silicon at the melting temperature," *Applied Physics Letters,* vol. 51, pp. 1747-1749, 1987.
[27] H. Rogne, P. J. Timans, and H. Ahmed, "Infrared absorption in silicon at elevated temperatures," *Applied Physics Letters,* vol. 69, pp. 2190-2192, 1996.
[28] N. M. Ravindra, S. Abedrabbo, C. Wei, F. M. Tong, A. K. Nanda, and A. C. Speranza, "Temperature-dependent emissivity of silicon-related materials and structures," *Semiconductor Manufacturing, IEEE Transactions on,* vol. 11, pp. 30-39, 1998.
[29] www.quartz.com/gedata.html#optics. (2007). *Optical properties of fused quartz*.
[30] C. L. Yaws, L. L. Dickens, R. Lutwack, and G. Hsu, "Semiconductor Industry Silicon: Physical and Thermodynamic Properties," *Solid State Technology,* pp. 87-92, 1981.
[31] W.-K. Rhim and K. Ohsaka, "Thermophysical properties measurement of molten silicon by high-temperature electrostatic levitator: density, volume expansion, specific heat capacity, emissivity, surface tension and viscosity," *Journal of Crystal Growth,* vol. 208, pp. 313-321, 2000.

Appendix A. Data fitting for heat calculations

The equations that were used for the heat calculation in the thermal model section were taken from a review article.[30] Data within the article was in the form of graphs and no explicit equations were given for the either the heat capacity or the density of silicon as a function of temperature. Points on the graphs were estimated and then plotted in Excel. A curve was then fitted to the points. This equation was used for the calculations in determining the heat content of a particular core diameter as a function of temperature. Figure A.1 is the fitted curve for the solid heat capacity of silicon. . The equation that fits the points is displayed in the graph along with the R^2 of 1 showing the fit of the equation to the data.

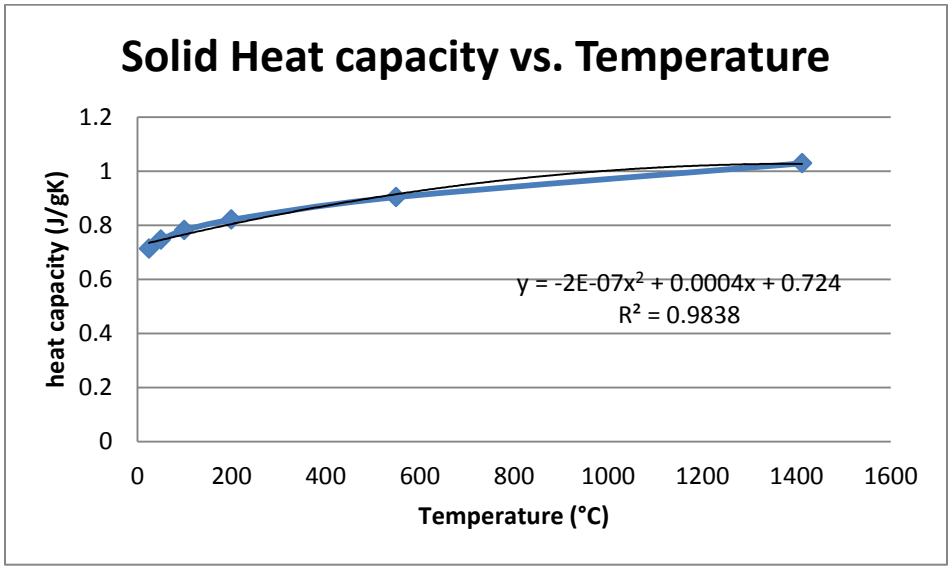

Figure A.1 Heat capacity of solid silicon versus temperature

Figure A.2 is the heat capacity of liquid silicon from the melting point to the 2300 °C. The equation for the fit is displayed in the graph, with an R^2 of 1, showing the fit of the equation to data.

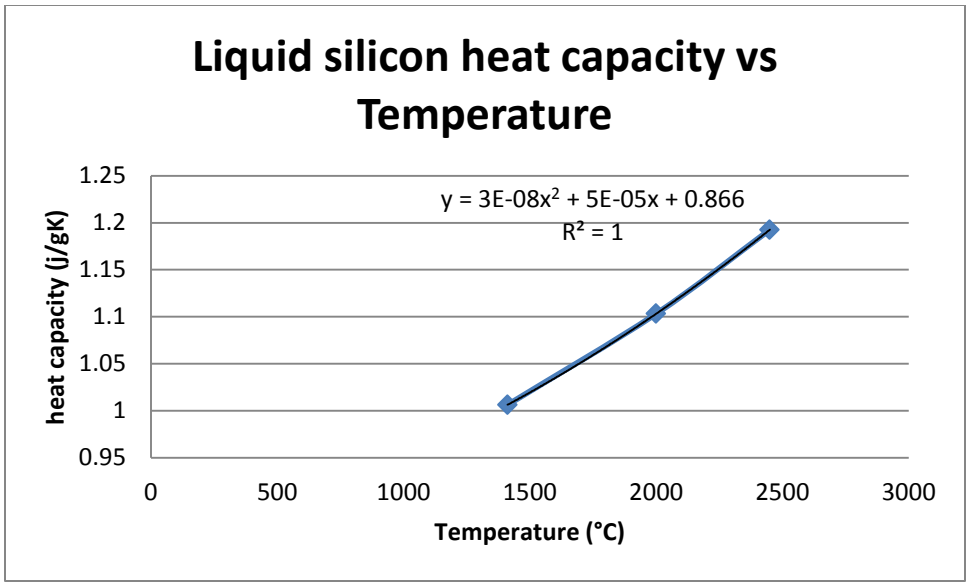

Figure A.2. Heat capacity of liquid silicon versus temperature

Figure A.3 is the graph of the data for the density of silicon as a function of temperature. The temperature range is from 20 °C to 1412 °C prior to melting. The equation for the fit is displayed in the graph, with an R^2 of 1, showing the fit of the equation to data.

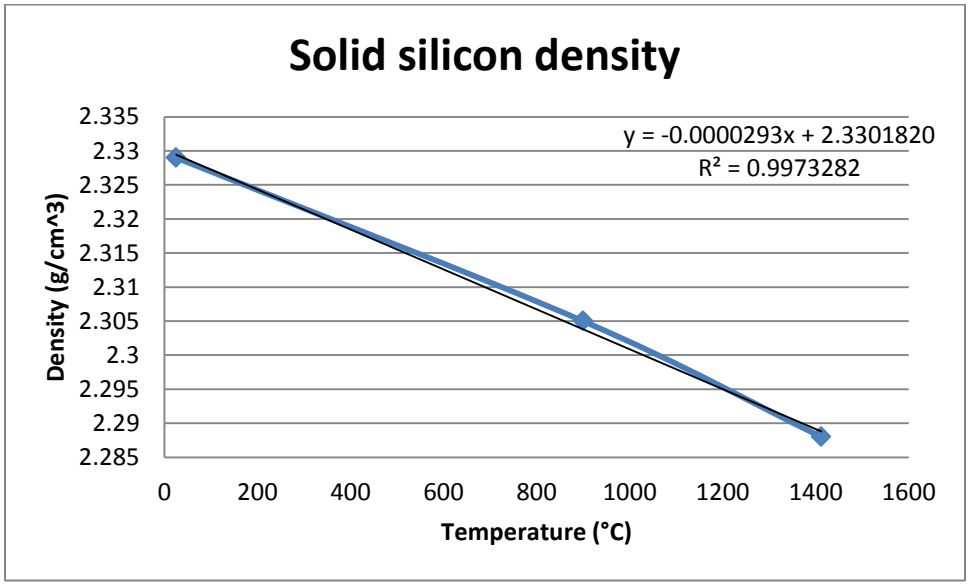

Figure A.3. Solid silicon density versus temperature

Figure A.4 is the graph of the data for the density of liquid silicon as a function of temperature. The temperature range is from the melting point at 1412 °C to 2300 °C. The equation for the fit is displayed in the graph, with an R^2 of 1, showing the fit of the equation to data

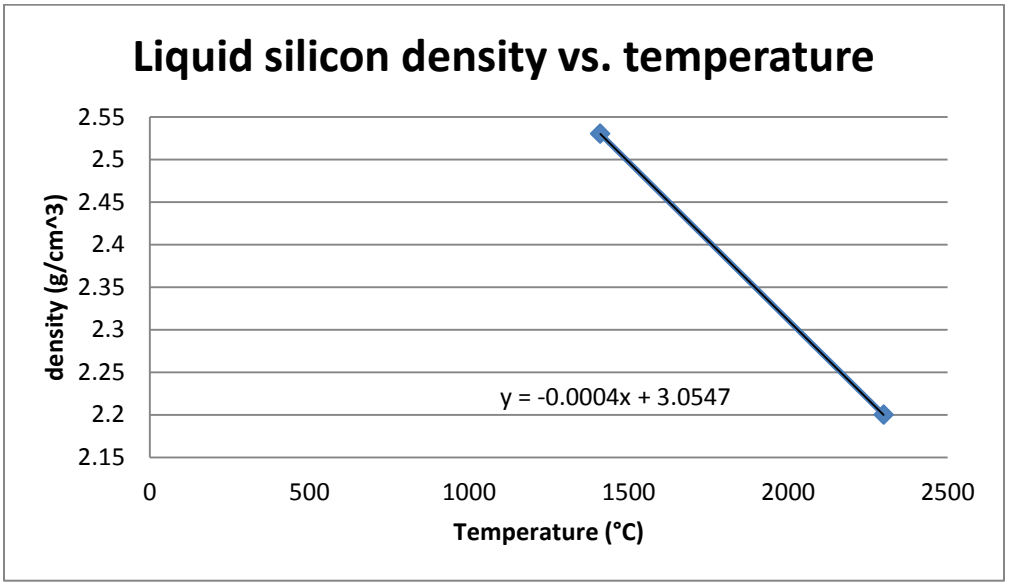

Figure A.4 Density of liquid silicon versus temperature

Appendix B. Mathematica program for calculating cooling curves

The calculations that were performed for the heat content, heat transfer and the cooling curves in section 5 was accomplished with a program written in Mathematica. A separate section was written for each of the cooling curve graphs displayed, but the only difference between them was the diameter of the core.

```
Needs["PlotLegends`"]
temp2 = Append[temp1, 2000]
heat178 = Transpose[{temp2, core178}]
heat290 = Transpose[{temp2, core290}]
heat39 =  Transpose[{temp2, core39}]
heat47 = Transpose[{temp2, core47}]
heat57 = Transpose[{temp2, core57}]
heat67 = Transpose[{temp2, core67}]
heat41 = Transpose[{temp2, core41}]
heat97 = Transpose[{temp2, core97}]
heat112 = Transpose[{temp2, core112}]
heat130 = Transpose[{temp2, core130}]
heat142 = Transpose[{temp2, core142}]
heat210 = Transpose[{temp2, core210}]
```

```
g2 = ListLinePlot[{heat39, heat47, heat57, heat67},
  Frame → True, FrameLabel → {"Temperature(°C)", "Heat Content [J/cm]"},
  PlotLegend → {"39μm", "47μm", "57μm", "67μm"}, LegendPosition → {0.95, -0.2},
  AxesOrigin → {0, 1000}, PlotRange → {{1000, 2000}, {0, .4}},
  ImageSize → Large, LegendSize → {.3, .4}, PlotStyle → {Thick},
  LegendLabel → "Core diameter", LegendSize → {0.4, .5}]
```

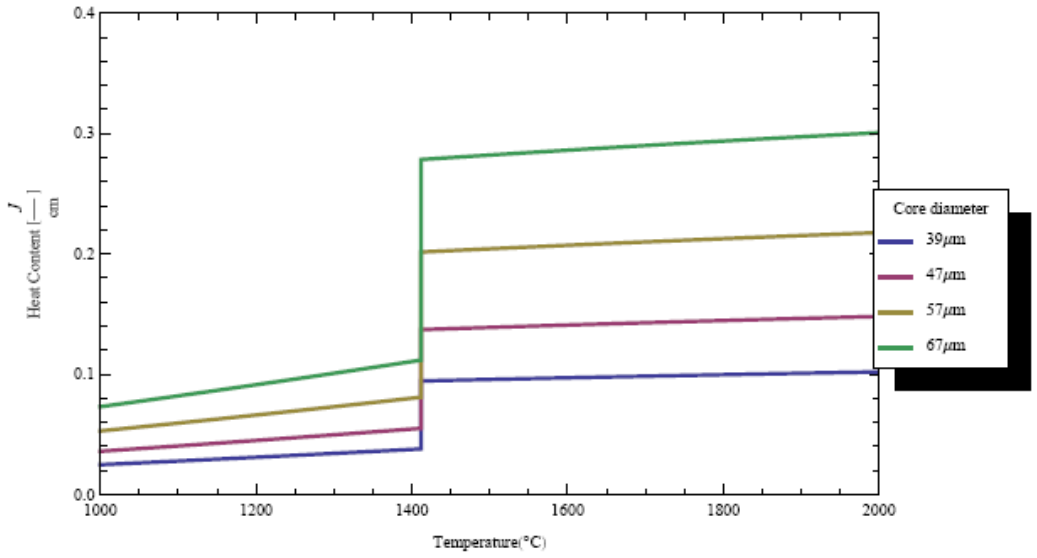

```
g1 = ListLinePlot[{heat178, heat290}, Frame → True,
  FrameLabel → {"Temperature(°C)", "Heat Content [J/cm]"},
  PlotLegend → {"178μm", "290μm"}, LegendPosition → {0.95, -0.2}, AxesOrigin → {0, 1000},
  PlotRange → {{1000, 2000}, {0, 6}}, ImageSize → Large, LegendSize → {.3, .4},
  PlotStyle → {Thick}, LegendLabel → "Core diameter", LegendSize → {0.4, .5}]
```

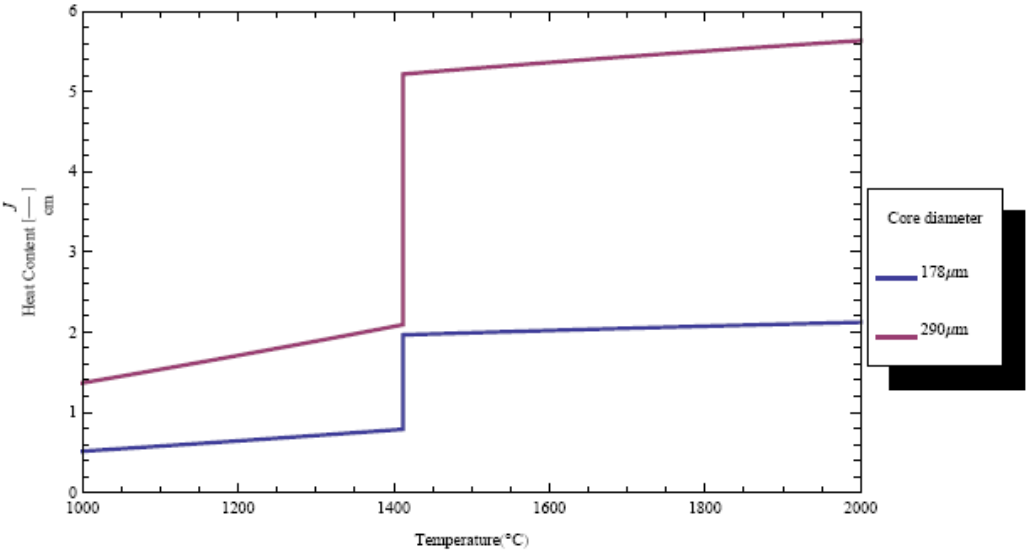


```
g3 = ListLinePlot[{heat41, heat97, heat112},
  Frame → True, FrameLabel → {"Temperature(°C)", "Heat Content [J/cm]"},
  PlotLabel → "Calculated Temperature vs. Heat Content of 4 m/min Fiber Sample Cores ",
  PlotLegend → {"41μm", "97μm", "112μm"}, LegendPosition → {0.77, -0.2},
  AxesOrigin → {0, 1000}, PlotRange → {{1000, 2000}, {0, 1}}, ImageSize → Large,
  LegendSize → {.4, .5}, PlotStyle → {Thick}, LegendLabel → "Fiber Diameter"]
```

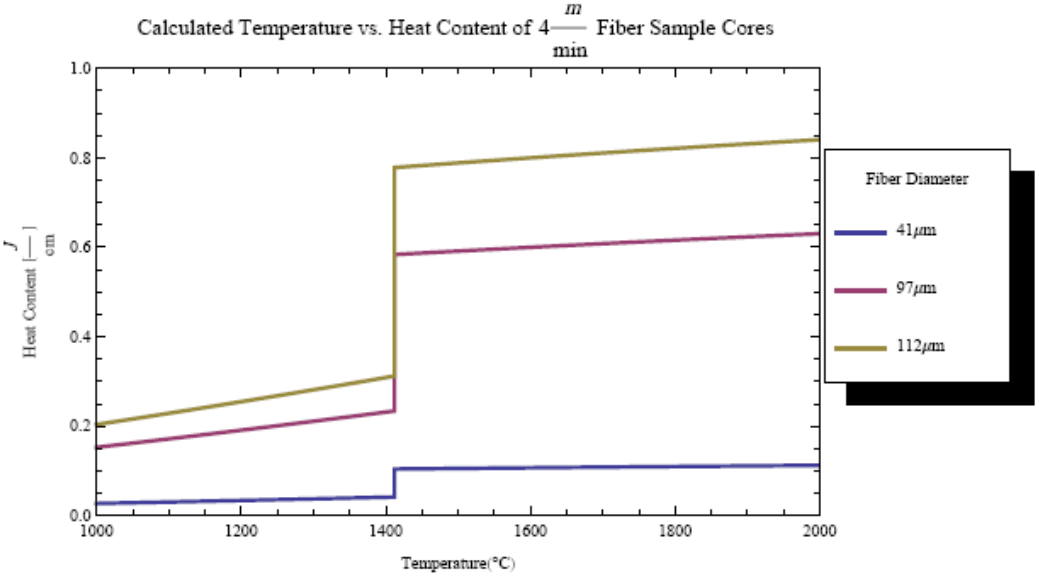

```
g4 = ListLinePlot[{heat130, heat142, heat210},
  Frame → True, FrameLabel → {"Temperature(°C)", "Heat Content [J/cm]"},
  PlotLabel → "Calculated Temperature vs. Heat Content of 4.5 m/min Fiber Sample Cores ",
  PlotLegend → {"130μm", "142μm", "210μm"}, LegendPosition → {0.77, -0.2},
  AxesOrigin → {0, 1000}, PlotRange → {{1000, 2000}, {0, 3}}, ImageSize → Large,
  LegendSize → {.4, .5}, PlotStyle → {Thick}, LegendLabel → "Fiber Diameter"]
```

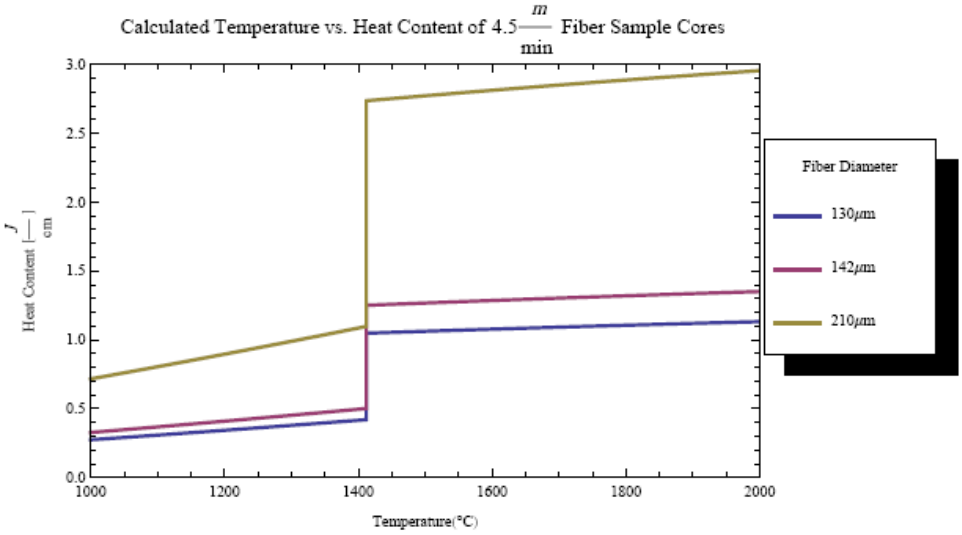


```
Needs["PlotLegends`"]
```

```
"Heat capacity of solid silicon"
```

```
solidcp = Integrate[-2 * 10^-8 x^2 + 0.0004 x + 0.724, {x, 25, T}]
```

$$-18.2249 + 0.724\,T + 0.0002\,T^2 - 6.66667 \times 10^{-9}\,T^3$$

```
"Heat capacity of liquid silicon"
```

```
liquidcp = Integrate[3 * 10^-8 x^2 + 5 * 10^-5 x + 0.866, {x, 1412, T}] + 1787.8
```

$$487.013 + 0.866\,T + 0.000025\,T^2 + 1. \times 10^{-8}\,T^3$$

```
"Area of fiber cross section in cm^2"
a178 = Pi * 0.0089^2
a290 = Pi * 0.0145^2
```

```
0.000248846
```

```
0.00066052
```

```
"Circumference of fiber cross section in cm"
c178 = 2 * Pi * 0.0089
c290 = 2 * Pi * 0.0145
```

```
0.0559203
```

```
0.0911062
```

```
"Stefan-Boltzman constant"
```

```
sig = 5.670400 * 10^-12
```

```
5.6704 × 10^-12

"Evaluation of heat capacity from 1000 to 1412°C and from 1412 to 2000°C"

heatbelow = Table[solidcp, {T, 1000, 1412}]

heatabove = Table[liquidcp, {T, 1412, 2000}]

heatabove1 = 1384.04 + heatabove

heat = Join[heatbelow, heatabove1]


"Evaluation of solid and liquid density"

soliddensity = Table[-0.0000293 T + 2.3301820, {T, 1000, 1412}]
liquiddensity = Table[-0.0004 T + 3.0547, {T, 1412, 2000}]

density = Join[soliddensity, liquiddensity]

"heat capacity * density"


heatcont = Table[Part[heat, i] * Part[density, i], {i, 1, 1002}]

"heat content of the core per unit length"
core178 = a178 * heatcont
core290 = a290 * heatcont

"heat loss per unit length from 1000-2000°C"

heatout178 = Table[Part[core178, i] - Part[core178, i - 1], {i, 1002, 2, -1}]

heatout290 = Table[Part[core290, i] - Part[core290, i - 1], {i, 1002, 2, -1}]

heatloss1781 = Table[0.7 * sig * (T^4 - 20^4) * c178, {T, 1000, 1412}]

0.7 * sig * (1412^4 - 20^4) * c178

0.882308

heatloss17811 = Append[heatloss1781, 0.882308331600002`]

heatloss1782 = Table[0.23 * sig * (T^4 - 20^4) * c178, {T, 1413, 2000}]


heatloss178j = Join[heatloss17811, heatloss1782]

heatloss2901 = Table[0.7 * sig * (T^4 - 20^4) * c290, {T, 1000, 1412}]

0.7 * sig * (1412^4 - 20^4) * c290

1.43747

heatloss29011 = Append[heatloss2901, 1.4374686301348347`]

heatloss2902 = Table[0.23 * sig * (T^4 - 20^4) * c290, {T, 1413, 2000}]

heatloss290j = Join[heatloss29011, heatloss2902]

"Reverse table order to match heatout order"

heatloss178r = Reverse[heatloss178j]

heatloss290r = Reverse[heatloss290j]

"Time to lose heat for core change of 1°C"

time178 = Table[(Part[heatout178, i] / Part[heatloss178r, i]), {i, 1, 1001}]

time290 = Table[(Part[heatout290, i] / Part[heatloss290r, i]), {i, 1, 1001}]
```

```
"Time to cool from 2150-1000°C"

Total[time178]

2.25672

Total[time290]

3.67668

"Adding terms in table for accumulated time during cooling"

timeacum178 = Accumulate[time178]

timeacum290 = Accumulate[time290]

"Reverse table order to match temperature table"

timeacumr178 = Reverse[timeacum178]

timeacumr290 = Reverse[timeacum290]

"Create a temperature table for plotting"

temp = Range[1000, 1412]

tempa = Range[1412, 1999]

temp1 = Join[temp, tempa]

"Merge time and temperature tables for plotting"

timetemp178 = Transpose[{timeacumr178, temp1}]

timetemp290 = Transpose[{timeacumr290, temp1}]

"Add term to start cooling at 2150°C"

timetemp178ap = Append[timetemp178, {0, 2000}]

timetemp290ap = Append[timetemp290, {0, 2000}]

ListLinePlot[{timetemp178ap, timetemp290ap},
 Frame → True, FrameLabel → {"Time (s)", "Temperature (°C)"},
 PlotLegend → {"178μm", "290μm"}, LegendPosition → {0.94, -0.2},
 AxesOrigin → {0, 1000}, PlotRange → {{0, 4}}, ImageSize → Large,
 LegendSize → {0.6, 0.6}, PlotStyle → Thick, LegendLabel → "Core Diameter"]
```